STUDY OF COHERENT STRUCTURES IN TURBULENT FLOWS USING PROPER ORTHOGONAL DECOMPOSITION

A Thesis Submitted to the College of

Graduate Studies and Research

In Partial Fulfillment of the Requirements

For the Degree of Doctor of Philosophy

In the Department of Mechanical Engineering

University of Saskatchewan

Saskatoon, Saskatchewan

By

MAZIAR SAMANI

Permission to Use

In presenting this thesis in partial fulfilment of the requirements for a Postgraduate degree from the University of Saskatchewan, I agree that the Libraries of this University may make it freely available for inspection. I further agree that permission for copying of this thesis in any manner, in whole or in part, for scholarly purposes may be granted by Dr. Donald J. Bergstrom who supervised my thesis work or, in his absence, by the Head of the Department or the Dean of the College in which my thesis work was done. It is understood that any copying or publication or use of this thesis or parts thereof for financial gain shall not be allowed without my written permission. It is also understood that due recognition shall be given to me and to the University of Saskatchewan in any scholarly use which may be made of any material in my thesis.

Requests for permission to copy or to make other use of material in this thesis in whole or part should be addressed to:

Head of the Department of Mechanical Engineering
University of Saskatchewan
57 Campus Drive, Saskatoon, Saskatchewan, Canada
S7N 5A9

Acknowledgments

First and foremost, I would like to acknowledge and warmly thank my PhD supervisor, Professor Donald J. Bergstrom, for his support, patience, encouragement and advice throughout the completion of this thesis. Also, I wish to thank his wife, Mrs. Naomi Bergstrom, for her kind invitations to their house, and great hospitality.

I sincerely thank members of my advisory committee, Dr. David Sumner, Dr. Fang-Xiang Wu and Dr. Richard Evitts, for their valuable comments which helped me to improve the quality of my research work. I appreciate the help and support I received from the faculty, staff and colleagues in the Department of Mechanical Engineering. I would like to extend a special thank you to Mr. David Deutscher for his valuable assistance during the lab demonstration experience, and also in helping with the CFD lab facilities. I gratefully acknowledge the funding support of the Natural Sciences and Engineering Research Council (NSERC) of Canada.

I also would like to take this opportunity to thank my parents, for believing in me in every single step. Lastly, my wife, Pegah, whose love and encouragement provided my inspiration to complete this work. She was always there, cheering me up and stood by me through the good times and bad.

Abstract

For many decades, turbulence has been the subject of extensive numerical research and experimental work. A bottleneck problem in turbulence research has been to detect and characterize the energetic, space and time-dependent structures and give a mathematical definition to each topology. This research presents a fundamental study of coherent structures, embedded in turbulent flows, by use of Proper Orthogonal Decomposition (POD). The target is to detect dominant features which contain the largest fraction of the total kinetic energy and hence contribute more to a turbulent flow. POD is proven to be a robust methodology in multivariate analysis of non-linear problems. This method also helps to obtain a low-dimensional approximation of a high-dimensional process, like a turbulent flow.

This manuscript-based dissertation consists of five chapters. The first chapter starts with a brief introduction to turbulence, available simulation techniques, limitations and practical applications. Next, POD is introduced and the step-by-step approach is explained in detail.

Three submitted manuscripts are presented in the subsequent chapters. Each chapter starts with introducing the study case and explaining the contribution of the study to the whole topic and also has its topic-relevant literature review. Each article consists of two parts: flow simulation and verification of the results at the onset, followed by POD analysis and reconstruction of the turbulent flow fields. For flow simulation, Large Eddy Simulation (LES) was performed to obtain databases for POD analysis. The simulations were validated by making comparison with available experimental and numerical studies. For each case, coherent topologies are characterized and the contribution of kinetic energy for each structure is determined and compared with previous literature.

The first manuscript focused on investigating the large-scale dynamics in the wake of an infinite square cylinder. This case is the first step towards the targeting study case of this research, *i.e.* flow over rib roughened walls. The main purpose the first step is to establish a benchmark for comparison to the

more complicated cases of a square cylinder with a nearby wall and flow over a rib-roughened surface. For POD analysis, the three-dimensional velocity field is obtained from LES of the flow around an infinite square cylinder at a Reynolds number of $Re = 500$. The POD algorithm is examined and the total energy of the flow is found to be well captured by only a small number of eigenmodes. From the energy spectrum, it is learned that each eigenmode represents a particular flow characteristic embedded in the turbulent wake, and eigenmodes with analogous characteristics can be bundled as pairs. Qualitative analysis of the dominant modes provided insight as to the spatial distribution of dominant structures in the turbulent wake. Another outcome of this chapter is to develop physical interpretations of the energetic structures by examining the temporal coefficients and tracking their life-cycle. It was observed that the paired temporal coefficients are approximately sinusoidal with similar order of magnitude and frequency and a phase shift. Lastly, it was observed that the turbulent flow field can be approximated by a linear combination of the mean flow and a finite number of spatial modes.

The second manuscript analyses the influence of a solid wall on the wake dynamics of an infinite square cylinder. Different cases have been studied by changing the distance between the cylinder and the bottom wall. From the simulation results, it is learned that the value of drag and lift coefficients can be significantly affected by a nearby solid wall. From the energy decay spectrum it is observed that the energy decay rate varies for different gap ratios and accordingly a physical explanation is developed. Visualization of coherent structures for each case shows that for larger gaps, although the structures are distorted and inclined away from the wall, the travelling wave characteristic persists. Lastly, it is observed that as the gap ratio gets smaller, energetic structures originated by the wall begin to appear in the lower index modes.

The last manuscript presents a numerical study of the structures in turbulent Couette flow with roughness on one wall, which as mentioned earlier, is the targeting study case of this research. Flow over both roughened and smooth surfaces was examined in a single study. Comparison was made with experiments and other numerical studies to verify the LES results. The mean velocity distribution across

the channel shows that the rib roughness on the bottom wall has a strong effect on the velocity profile on the opposite wall. The energetic coherent dynamics of turbulent flow were investigated by the use of POD. The energy decay spectrum was analysed and the influence of a roughened wall and each roughness element on formation of those structures was investigated. Coherent POD modes on a spanwise sampling plane are detected. A secondary swirling motion is visualized, for the first two modes and counter-rotating cells are observed in the lower region of the channel above the rough wall for the higher modes. At the end, a quantitative analysis of the POD temporal coefficients was performed, which characterize the life-cycle of each coherent dynamic. A motivating outcome of this analysis is to decompose the time trace curves into quasi-periodic and fluctuations curves and to detect a linkage between these life cycles and physical meaning and location of each energetic pattern.

At the end, in a closuring chapter, concluding remarks of this research work are presented in more detail and some potential extensions have been proposed for future researchers.

To the wonderful one

Without whom I would have been graduated by now
But life would be joyless…

Table of Contents

Permission to Use i
Acknowledgements ii
Abstract iii
Dedication vi
Table of Contents vii
List of Figures x
List of Tables xiii

Chapter 1: Introduction 1
1.1 Motivation 1
1.2 Objectives and Scope 3
1.3 The Expected Contributions 5
1.4 Numerical Methodology 6
1.4.1 Governing equations 6
1.4.2 Discretization scheme 7
1.4.3 Turbulence modeling 9
1.4.4 Proper Orthogonal Decomposition 11
1.5 Literature Review 13
1.6 Thesis Outline 18
References 20

Chapter 2: Capturing the Large-Scale Dynamics in the Wake of an Infinite Square Cylinder using Proper Orthogonal Decomposition 26
Preamble 27
Abstract 28
2.1 Introduction 28
2.2 Numerical Methodology 31
2.2.1 Flow configuration and LES 31
2.2.2 Proper Orthogonal Decomposition 33
2.3 Selected Results and Discussion 35

2.3.1 Vortex shedding frequency 35
2.3.2 Mean and fluctuating velocity components in the wake 37
2.3.3 Phase-averaged structures 41
2.4 POD Analysis 45
2.4.1 Energy spectrum 45
2.4.2 Energetic velocity modes 47
2.4.3 Reconstruction of turbulent flow 51
2.4.4 Streamwise sampling plane 52
2.5 Conclusions and Outlook 57
References 59

Chapter 3: Effect of a Wall on the Wake Dynamics of an Infinite Square Cylinder 63
Preamble 64
Abstract 65
3.1 Introduction 65
3.2 Computational Details 68
3.3 Selected Results and Discussion 71
3.3.1 Flow simulation results 71
3.3.2 POD analysis 77
3.4 Conclusions and Recommendations 82
References 83

Chapter 4: Turbulent Couette Flow with Rib-Roughness: A Study of Coherent Structures using Proper Orthogonal Decomposition 87
Preamble 88
Abstract 89
4.1 Introduction 90
4.2 Computational Methodology 92
4.2.1 Flow physics, transport equations and numerical approach 92
4.2.2 Implementation of Proper Orthogonal Decomposition 97
4.3 Selected Results and Discussion 98
4.3.1 Validation of Couette flow results 98
4.3.2 Proper Orthogonal Decomposition 107
4.3.2.1 Spanwise sampling plane 107

4.3.2.2 Streamwise sampling plane 112
4.3.2.3 Analysis of the lifecycle of the eigenvectors 116
4.4 Conclusions 120
References 122

Chapter 5: Concluding Remarks 126
5.1 Thesis Summary 126
5.2 Conclusions and Contributions 127
5.2 Recommendations for Future Extension 131

Appendix: Side Works 133
References 137

List of Figures

2.1 Cartesian computational grid configuration around the infinite cylinder 32

2.2 Time trace of spanwise velocity and spanwise vorticity 35

2.3 Power spectrum based on spanwise velocity component 36

2.4 Streamlines in center plane (mean and instantaneous) 37

2.5 Time-averaged stream traces near rear corner of prism 38

2.6 Time-averaged streamwise velocity distribution along the centerline and transverse section in the wake 39

2.7 Distribution of fluctuating energy along the centerline for streamwise and transverse velocity components 40

2.8 Profiles of the mean streamwise velocity and fluctuations along transverse section located at the midpoint of the top wall of cylinder 42

2.9 Phase-average iso-vorticity contours and vector plot at 1/4 , 1/2 , 3/4 and 1 shedding period (T) 43

2.10 Phase-averaged transverse velocity component along the centerline for two phases 44

2.11 Vorticity contours and vector plot of time-averaged flow, comparison with streamwise and transverse velocity distribution for two selected phases 45

2.12 Convergence of POD eigenvalues 46

2.13 Spatial structures of the first 3 eigenmodes (streamline pattern, streamwise and transverse velocity component) 48

2.14 Temporal behavior of the first five eigenmodes over one shedding period, cross plot of normalized $[a_1\text{-}a_2]$, $[a_1\text{-}a_4]$ and time evolution of $[a_1\text{-}a_2]$ over 13 shedding periods 49

2.15 Streamlines for instantaneous and reconstructed flow field for M_o=2, M_o=24 and M_o=60 51

2.16 Energy spectrum for streamwise sampling plane 53

2.17 Lateral component (ϕ_{u3}) of the first six eigenmodes 54

2.18 Spanwise component (ϕ_{u2}) of the first six eigenmodes 55

2.19 Velocity vector field of the first six eigenmodes 56

3.1 Flow configuration and layout of computational grid 69

3.2 Power spectra of lift forces for different gap heights 72

3.3 The variation of mean drag and lift coefficients with gap ratio....73
3.4 Effect of gap width on flow structures (g/D = 0, 0.5, 1 and ∞) 75
3.5 Averaged velocity profiles in the gap region (g/D = 0, 0.5, 1 and ∞) 76
3.6 Decay of energy for different gap ratios....78
3.7 First three modes for streamwise velocity component Φ_{u1} (g/D = 0, 0.5, 1 and ∞) 80
3.8 First three modes for wall-normal velocity component Φ_{u3} (g/D = 0, 0.5, 1 and ∞) 81
3.9 First three modes for spanwise vorticity component $\Phi_{\omega 2}$ (g/D = 0, 0.5, 1 and ∞)....82
4.1 Geometrical sketch of the channel showing sampling planes 95
4.2 Projected computational grid....96
4.3 Mean velocity distribution across the channel....99
4.4 Mean velocity distribution expressed in wall coordinates....100
4.5 Profile of resolved-scale streamwise velocity fluctuation in wall coordinates....102
4.6 Shear stress profile across the channel 103
4.7 Mean and instantaneous flow patterns (stream traces and spanwise vorticity) 104
4.8 Time-averaged streamlines in spanwise plane....105
4.9 Instantaneous velocity vector field in different x_1-x_2 planes 106
4.10 POD eigenmodes energy spectrum....107
4.11 First four modes for the Φ_{u1} component....108
4.12 First four modes for the Φ_{u3} component....109
4.13 First four modes for the $\Phi_{\omega 2}$ component 110
4.14 POD modes of a single rib on ground plane (Φ_{u1} and Φ_{u3}) 111
4.15 Ensemble averaged motions in a streamwise plane....112
4.16 Energy spectrum from POD in two planes 113
4.17 Velocity vector plots of the first four eigenmodes in the y-z plane 114
4.18 Φ_{u3} component for the first four modes....116
4.19 Φ_{u2} component for the first four modes....117
4.20 $\Phi_{\omega 1}$ component for the first four modes 118
4.21 Time variation of temporal coefficients for the first four modes 119

4.22 Time histories of the first four modes over 100 non-dimensional time units 120

4.23 Decomposition of $a_n(t)$ plots (trend curves and oscillations) 121

A.1 Formation of cavity flow between elements 133

A.2 Steady solution at Re = 1000 (streamlines and velocity profiles along horizontal and vertical centerlines) 134

A.3 Velocity vectors for the first 4 eigenmodes 135

A.4 Streamline patterns of Re : 3000 and Re : 8000 136

A.5 Velocity vectors for the first 2 eigenmodes (Re : 8000) 136

List of Tables

3.1 The mean drag and lift coefficients for four different value of gap ratio; comparison to data in literature 74

4.1 Comparison of roughness shifts in different studies.....101

Chapter 1

Introduction

"A biologist, a chemist, and a CFD Professor are taking a walk through the countryside when they come upon a "Bigfoot". For some reasons, none of them knew what it was. The biologist thinks for a second and then declares, "I know what that is. That's a bipedal anthropoid mammal." The chemist looks for a second and then says, "It's just a carbon-based life form, approximately 75% water, and the remaining 25% trace elements." The CFD Professor stares blankly for a second and then says, "Well.... I guess we could approximate it as a finite cylinder in a free-stream."

1.1 Motivation

According to the book "A Voyage Through Turbulence" [1], the history of turbulence start with Leonardo da Vinci, when he used the word "*turbolenza*" and sketched a variety of turbulent flows. Turbulence refers to a fluid motion with random and chaotic three-dimensional vorticity. Most of the industrial and environmental flows are turbulent, e.g. aerodynamic flows, combustion, rivers and even the exhaust jets from noses when people breathe. *The advantage of studying turbulence is that you truly can see it almost everywhere as it mixes and diffuses, disrupts and dissipates the world around us* as quoted in [2]. That, in fact, is the motivation and importance of studying turbulence.

However, there are difficulties in studying turbulent flow, primarily because it is difficult to fundamentally understand the physics and impossible to solve it analytically (even though the governing equations are known). The dynamical system is strongly non-linear and the available theory, both in the context of turbulence and transition-to-turbulence, is very limited. The existing exact solutions are very limited and they are often obtained by taking a number of assumptions which in some cases involve physically unrealistic suppositions. An alternate approach to analytical solution would be to numerically simulate the flow. A high fidelity simulation provides observation on how a turbulent flow behaves and what it looks like. Consequently, a simulated flow can provide insight as to its mechanisms. There are a number of techniques to numerically resolve the turbulent motions. The most common technique in engineering applications is the so-called Reynolds Averaged Navier Stokes (RANS) method. This approach is based on averaging the equations of motion. The opposite approach is Direct Numerical Simulation (DNS), in which the Navier-Stokes equations are directly solved without any turbulence model. Although DNS is (potentially) the most accurate way of computing turbulent flow, the computational cost in a DNS grows quickly with Reynolds number. Therefore, DNS is unsuitable for most practical computations. Some key references that describe RANS and DNS are [1], [2] and [3].

In between, there is Large Eddy Simulation (LES) which solves the larger motions directly (LES is DNS of large scales), and models (approximates) the smaller scale eddies. LES is a suitable method for practical flows and complex domains, but requires much more computational effort than RANS. Moreover, LES is able to predict the instantaneous flow characteristics and resolve turbulent flow structures, with much lower cost compared to DNS. That is why LES is chosen to simulate the turbulent flows in this research.

It should be noted here that, a third approach to study turbulent flows, which is equally as challenging (for many of the same reasons), is to perform experiments. Many of key parameters of turbulent flows can be obtained from experimental measurements, especially when it comes to time-averaged parameters. Those outputs can be used to validate numerical simulations of turbulent flows. However, when it comes

to instantaneous flow fields, conventional experimental studies do not give as much information as one can obtain from numerical simulations. In other words, numerical simulations give more spatio-temporal information. In addition, the accuracy of results in experimental research is limited to the measuring instrument. Therefore numerical simulation is chosen for this research work.

Having simulated a turbulent flow, a challenge would be to identify the coherent structures which dominate this multi-scale process. A thorough understanding of turbulent structures, their energy content and interactions, can be very beneficial for flow control purposes, flow reconstruction and even airfoil profile design, and therefore it is chosen as the main objective of this research. Some key review articles on coherent structures in turbulent flows are [4], [5] and [6].

The most common technique used by former researchers is the so called turbulence statistics, which yields the mean properties and turbulence intensities. However, it does not give much information about the lifecycle of each structure, i.e. birth, growth, decay and death of each structure as well as its contribution to the whole flow. It is difficult to give a mathematical definition to a spatio-temporal structure, and this is where Proper Orthogonal Decomposition (POD) comes into play. POD is proven to be a powerful method of data analysis that facilitates a low-dimensional approximation of a high-dimensional process. In addition, POD modes are the optimal decomposition for a turbulent flow field that much of the flow topology can be captured by using only a few modes. Some key references that used POD to investigate large scale energetic structures in turbulent flows are [7], [8] and [9].

1.2 Objectives and Scope

The ultimate scope of this research is to study the turbulent flow over rough walls and the objective is to investigate the turbulent structures caused by rough walls. In order to reach there, the flow simulation was done in three steps.

First, it starts with study of the external incompressible flow around an infinite cylinder of square cross section. The reason to choose this "simple" geometry for the first step is to verify the LES and POD algorithm on a configuration where a number of earlier experimental and numerical studies are available for comparison. Another intention is to establish a benchmark for comparison to more complicated cases in the following studies. The main objective of the first study was to investigate large-scale velocity structures and their corresponding energy content in the turbulent wake region.

In the second study, a ground plane was added and the cylinder (in the first study) was moved towards the bottom wall (and ultimately on the wall). The main objective for the second study is to investigate the interaction between the structures generated by the wall and turbulent wake.

In the third and final study, to simulate Couette channel flow, the pressure gradient was removed and a moving top surface was added, such that the flow would solely be driven by the motion of the top surface. A number of rib elements were periodically distributed in the streamwise direction (to resemble a roughened surface). The scope of this particular set-up was to compare flow over rough and smooth walls within a single study for the same flow conditions: the top wall resembles flow over a smooth wall, while transitional roughness is obtained on the bottom wall. The objective of this study is to analyse the topologies of the coherent structures generated by the rough wall, make a comparison with those in proximity of the smooth wall and finally investigate the interactions of the coherent structures in the core region.

In the context above, the main objectives of this thesis can be summarized as follows:

- To investigate large-scale velocity and vorticity structures and their corresponding energy content in turbulent flows;
- Examine the ability of POD in reconstructing turbulent flow;
- Explore the structures generated by a solid wall and their interactions with the turbulent wake structures;

- Examine topologies of coherent turbulent structures generated by rough and smooth surfaces and investigate the interactions with coherent structures in the core region.

1.3 The Expected Contributions

In the first study case, an infinite square cylinder in a free stream, the Reynolds number based on the approach-flow velocity (U_∞), cylinder edge-length (D) and dynamic viscosity of the flow (ν) was set to $Re = 500$ ($U_\infty D/\nu$), where a number of high resolution numerical results are available for comparison. The first expected contribution for this study case was to resolve the turbulent wake flow field by using a relatively courser mesh and accordingly, lesser computational time and cost compared with the existing numerical simulations. Another expected contribution of this study case was to perform a qualitative analysis of the coherent structures in different sampling planes, spanwise and lateral, and examine the three-dimensionality of the turbulent wake generated by a prismatic bluff body.

For the second study case, an infinite square cylinder in proximity of a solid wall, a similar Reynolds number was adopted to make a connection with the first study. The expected contribution was to examine how a nearby wall can affect the energy contained in the energetic eigenmodes. Investigating the distribution of energetic topologies and the effect of the wall on generating or distorting coherent topologies was also expected to be another contribution of this study.

The last study case, turbulent Couette flow in a channel with rib-roughness on one wall, is unique both in terms of simulation and POD analysis. The main expected contribution from the simulation perspective was to examine the effect of roughness on the velocity distribution across the channel and consequently measure the characteristic roughness shift. From POD analysis, detecting and classifying the coherent structures in two sampling planes was expected to be another contribution of this study.

In the context above, to recap the main expected contributions of the three studies:

- To provide a new insight as to the spatial distribution of dominant structures in the turbulent wake and flow inside a roughened channel;
- Showing how one can get a sense of the physical nature of each dominant structure and structures with the same or similar energy content, by analyzing eigenmodes energy spectrum;
- To present a method to develop physical interpretations of the energetic structures by examining the temporal coefficients and tracking their life-cycle and a technique to detect a linkage between these life cycles and physical meaning and location of each energetic pattern.

1.4 Numerical Methodology

In this section the numerical approach is outlined. First, the governing equations are determined and the discretisation scheme used in the simulation is explained. Then, details of LES and the POD methodology are outlined in the next subsections.

1.4.1 Governing equations:

Turbulence is a flow regime, not a property of a fluid, so the governing equations are the same as for laminar flow. Therefore, the Navier-Stokes (NS) and continuity equations are used as the governing equations to describe turbulent flow:

$$\frac{\partial \boldsymbol{u_i}}{\partial t} + \boldsymbol{u_j}\frac{\partial \boldsymbol{u_i}}{\partial \boldsymbol{x_j}} + \frac{1}{\rho}\frac{\partial p}{\partial \boldsymbol{x_i}} - \nu\frac{\partial^2 \boldsymbol{u_i}}{\partial \boldsymbol{x_j}\partial \boldsymbol{x_j}} = \boldsymbol{f}_i \tag{1.1}$$

and

$$\frac{\partial \boldsymbol{u_i}}{\partial \boldsymbol{x_i}} = 0. \tag{1.2}$$

Here $\boldsymbol{u_i}$ is the i component of velocity field, p is the pressure, t is the time, $\boldsymbol{x_i}$ is the corresponding Cartesian coordinate and $\boldsymbol{f_i}$ is an external force term. The specific terms in equation (1.1) are the unsteady term, the convection term, $\boldsymbol{u_j \frac{\partial u_i}{\partial x_j}}$, which is nonlinear, the diffusion term, the pressure term, and the body force. Note that the above equations are for incompressible flow, constant properties and Newtonian fluids.

By the use of numerical simulation, one can approximate the above equations by a system of algebraic equations. With increasing computer power, this field has become more popular and is known as Computational Fluid Dynamics (CFD). The typical procedure in numerical approaches is as follows. The first step is to choose an appropriate mathematical model, i.e. a set of partial differential equations and proper boundary and initial conditions. The next step is to find a method for approximating the equations by a system of algebraic equations which is the discretization method. Based on the flow conditions and geometry, the discretization can be performed on a Cartesian, cylindrical, spherical or any curvilinear coordinate system.

1.4.2 Discretization scheme:

In this work, the finite volume method (FVM) is chosen as the discretization technique. In this approach the solution domain is covered by a finite number of control volumes. Notwithstanding that the FVM is regarded as the simplest approach to program, the FVM is also an efficient method for complex geometries, since it can accommodate many types of grids and geometries. This is the reason why the FVM is the most popular discretization method in CFD applications. However, this scheme also has some disadvantages compared with the finite difference method. When it comes to higher-order methods, it is more difficult to implement higher order schemes in the FVM especially in three dimensions [15].

The basic concept of the FVM is to balance the unsteady term and the net flux across the bounding surfaces. Therefore the finite volume approximation deals with approximations of surface integrals,

$$\int_{S_i} f dS\,, \tag{1.3}$$

where *f* is the net flux and *S* denotes the surface. In order to approximate (1.3), one needs to approximate the integrand (f) first. Based on the required accuracy and computational costs, one may choose an approximation method among several available approaches. More details on common approaches can be found in [3].

In this work, a second order fractional step algorithm is employed to solve the governing equations. In the fractional step method, first the momentum equation is solved in a predictor step to obtain an intermediate value of the velocity field based on previous pressure field. Then a Poisson equation for the pressure field is formed by taking the divergence of the momentum equation. Finally, the convector step uses the new pressure field to obtain an improved solution for the velocity field.

In order to describe the methodology, the starting point is to rearrange the NS equations in the form of

$$\frac{\delta u^n}{\delta t} = (\sum a_{nb}\, u_{nb}^n - a_p u_p^n + b)/\rho V\,. \tag{1.4}$$

Here *n* denotes the time step, δt is the time space between the two time steps and the $a_i u_i$ terms represent the flux through the face i. Now, the mathematical algorithm would be:

Step 1) advection-diffusion equation step:

$$\text{node velocity:}\quad \vec{u}_p^* = u_p^n + \rho\delta t\left(\frac{3}{2}\frac{\delta u^n}{\delta t} - \frac{1}{2}\frac{\delta u^{n-1}}{\delta t}\right) \tag{1.5.a}$$

and

$$\text{face velocity:}\quad \vec{u}_e^* = \frac{1}{2}\left(u_p^* + u_E^*\right) - \frac{A_e}{\rho\nu/\delta t}\left({P_E}^n - {P_p}^n\right), \tag{1.5.b}$$

where $\vec{u}^*$ is the intermediate velocity obtained from the momentum equation and A represents the control volume face.

Step 2) mass-conservation

$$a_p P'_P = \sum a_{nb} P'_{nb} + b \tag{1.6}$$

where b is the mass residual based on the $\vec{u}^*$ field, i.e.

$$b = -\rho\left[A_x(\vec{u}^*_e - \vec{u}^*_w) + A_y(\vec{u}^*_n - \vec{u}^*_s) + A_z\left(\vec{u}^*_f - \vec{u}^*_b\right)\right] \tag{1.7}$$

Here A_x, A_y and A_z are the face areas in *x, y* and *z* direction respectively. At the end of this step the pressure correction term will be obtained.

Step 3) pressure correction step

$$P_P{}^{n+1} = P_P{}^n + P'_P \tag{1.8}$$

Step 4) updating the velocities

$$\text{node velocity:} \quad u_p^{n+1} = u_p^* - \frac{\delta t}{\rho(2\delta x)}(P_E{}^{n+1} - P_W{}^{n+1}) \tag{1.9.a}$$

and

$$\text{face velocity:} \quad \vec{u}_e^{n+1} = \vec{u}_e^n - \frac{A_e}{\rho\nu/\delta t}(P'_E - P'_P). \tag{1.9.b}$$

More details about the fractional step methodology can be found in [3] and [10].

1.4.3 Turbulence modeling:

As mentioned previously, in this study LES is employed for modelling the flow. In LES one solves the large-scale motions and approximates the small-scale motions. This approach is based on Kolmogorov's theory of self-similarity, which states that the large eddies of the flow are dependent on the flow geometry, while the smaller eddies are more universal [11]. The large scale motions can be computed directly while the effect of the small-scale motions represented by a subgrid-scale model (SGS model). First the flow is decomposed as

$$u_i = \bar{u}_i + u_i' \,, \tag{1.10}$$

where $\bar{u}_i$ is the large scale component of the velocity field and u_i' is the SGS part. The large scale velocity $\bar{u}_i$ can be obtained by a filtering technique, i.e.

$$\bar{u}_i(\vec{x}) = \int G(\vec{x}, \vec{\alpha}) u(\vec{\alpha}) d\vec{\alpha} \tag{1.11}$$

where the function $G(\vec{x}, \vec{\alpha})$ is called the filter kernel, which eliminates the small-scale eddies, and $\vec{x}$ and $\vec{\alpha}$ are the coordinates. There are several possible filtering techniques, e.g. Gaussian, box filter and cut-off, that can be applied. Every filter has a characteristic width, Δ, and the condition $\Delta > h$ (where h is the grid size) should be satisfied. After implicitly filtering the incompressible Navier-Stokes equations with a spatial filter of characteristic width, Δ, the governing equations become

$$\frac{\partial \bar{u}_i}{\partial t} + \frac{\partial (\bar{u}_i \bar{u}_j)}{\partial x_j} = -\frac{1}{\rho}\frac{\partial p}{\partial x_i} + \nu \frac{\partial^2 \bar{u}_i}{\partial x_j \partial x_j} - \frac{\partial \tau_{ij}}{\partial x_j} \tag{1.12}$$

and

$$\frac{\partial \bar{u}_i}{\partial x_i} = 0 \,, \tag{1.13}$$

where $\bar{u}_i$ is the filtered velocity component and the variable τ_{ij} is the so-called subgrid-scale stress (SGS) term which is given by

$$\tau_{ij} = \overline{u_i u_j} - \bar{u}_i \bar{u}_j \,. \tag{1.14}$$

For closure, a model relation is required for the SGS term. Perhaps the simplest and most common model used for the subgrid stresses is the Smagorinsky model which uses an eddy viscosity formulation for the SGS term, i.e.

$$\tau_{ij} - \frac{1}{3}\delta_{ij}\tau_{kk} = -2\nu_t \bar{S}_{ij} \,, \tag{1.15}$$

in which the SGS viscosity (ν_t) needs to be specified. From dimensional analysis

$$\nu_t = C_S^2 \Delta^2 |\bar{S}| \,, \tag{1.16}$$

where C_S is the model parameter, $\bar{S}_{ij} = \frac{1}{2}\left(\partial \bar{u}_i/\partial x_j + \partial \bar{u}_j/\partial x_i\right)$ and $|\bar{S}| = \left(\bar{S}_{ij}\bar{S}_{ij}\right)^{\frac{1}{2}}$. In isotropic turbulence $C_S \approx 0.2$ can be used, but in general, C_S is not a constant; it may be a function of Reynolds number, can be affected by a wall and may take different values in different flows. The Smagorinsky model is poor at representing details of the SGS stresses, especially at higher Reynolds numbers. In the current study, the so called Dynamic Smagorinsky (DS) model of Germano *et al.* [12] is employed to improve the modelling. In this model, C_S is determined as a variable of space and time, utilizing two filters with different characteristic scales: a grid filter and a test filter. Additional details of the mathematical formulation of this methodology can be found in [13].

1.4.4 Proper Orthogonal Decomposition:

As mentioned previously POD is a powerful method of data analysis that can be used to obtain a low-dimensional approximation of a high-dimensional process. POD is also known as the *Karhunen–Loéve* Expansion. There are applications of POD in different fields: turbulent flow modelling, structural vibrations, image processing, signal analysis, etc. POD was first introduced to the study of turbulence by Lumley [11]. In order to identify coherent structures, Lumley used functions of spatial variables that have the maximum energy content. So based on his definition, coherent structures are linear combinations of $\boldsymbol{f}(\boldsymbol{x})$'s which maximize the following expression,

$$\frac{\langle (\boldsymbol{f}(\boldsymbol{x}), \boldsymbol{u}(\boldsymbol{x}, t))^2 \rangle}{\left(\boldsymbol{f}(\boldsymbol{x}), \boldsymbol{f}(\boldsymbol{x})\right)} \,, \tag{1.17}$$

where $(A,B) = \int_\Omega A\bar{B}\, d\Omega$. Assume there is a function, call it $\boldsymbol{f}_1(\boldsymbol{x})$, that maximizes the equation above; then if the flow field $\boldsymbol{u}(\boldsymbol{x}, t)$, is projected along $\boldsymbol{f}_1(\boldsymbol{x})$, the average energy content is larger than if the flow field is projected along any other direction. If one then repeats the maximization process in the space

orthogonal to $\boldsymbol{f_1(x)}$, a set of orthogonal functions $\boldsymbol{f_i(x)}$ can be determined. The $\boldsymbol{f}_i(\boldsymbol{x})$'s are called the orthogonal basis functions [17].

The POD methodology attempts to decompose the flow field ($\boldsymbol{\phi(x_i}, t)$) into an orthonormal system of spatial modes ($\boldsymbol{\phi_m(x_i)}$) and corresponding temporal coefficients ($a_m(t)$), where

$$\boldsymbol{\phi}(\boldsymbol{x_i}, t) = \boldsymbol{\phi_0}(\boldsymbol{x_i}) + \sum_{m=1}^{M} a_m(t)\boldsymbol{\phi_m}(\boldsymbol{x_i}) \tag{1.18}$$

The representation of equation (1.18) is not unique; there are several choices of functions $\boldsymbol{\phi_m(x_i)}$, based on different types of series such as Fourier series, Legendre or Chebyshev polynomials, etc. Likewise, the time coefficients, $a_m(t)$, are different. The POD is concerned with one possible choice of function: the POD eigenfunctions are optimal with respect to energy content, which means that any other set of modes contains less energy on average than the corresponding POD eigenfunctions. One can use this property to determine the most energetic structures of the flow.

To compute the POD coefficients, the method of snapshots by Sirovich [5] is employed in this study. The coefficients are obtained from the solution of an eigenvalue problem associated with the correlation matrix. For example, if a velocity field is used as the input data for POD analysis, the correlation matrix would be

$$C_{mn} = \frac{1}{M}\int_{\Omega} [\boldsymbol{u}'(\boldsymbol{x_i}, t_m)\boldsymbol{u}'(\boldsymbol{x_i}, t_n)]\, d\boldsymbol{x_i}\,, \tag{1.19}$$

where $\boldsymbol{u}'(\boldsymbol{x_i}, t)$ represents the fluctuating part of the flow field, i.e.,

$$\boldsymbol{u}'(\boldsymbol{x_i}, t) = \boldsymbol{u}(\boldsymbol{x_i}, t) - \boldsymbol{U_0}(\boldsymbol{x_i})\,. \tag{1.20}$$

After solving the eigenvalue problem associated with the correlation matrix, a series of eigenvalues and corresponding eigenvectors are obtained; the eigenvectors are the temporal coefficients ($a_m(t)$) in (1.18). The eigenvalues are used to compute the total energy and evaluate the energy captured by each

mode. Moreover, there is a mathematical relation between the temporal coefficients and the eigenvalues λ^i given by

$$\overline{a_i a_j} = \frac{1}{M}\sum_{m=1}^{M} a_i(t_m)a_j(t_m) \; = \lambda^i \delta_{ij} \; . \tag{1.21}$$

Finally, the POD modes are computed as

$$\boldsymbol{u_m}(\boldsymbol{x_i}) = \frac{1}{M\lambda^m}\sum_{m=1}^{M} a_m(t_n)\boldsymbol{u'}(\boldsymbol{x_i}, t_n) \; . \tag{1.22}$$

A MATLAB code was developed to implement the POD algorithm based on the above formulation.

1.5 Literature Review

As mentioned before, there are a number of techniques to numerically resolve the turbulent motions, and among these LES is chosen to simulate the turbulent flows in this thesis. The first attempt to numerically solve a turbulent flow goes back to 1922, when Richardson [14], a meteorologist, developed a numerical scheme to solve the equations applied to the atmosphere. Four decades after, another meteorologist named Smagorinsky proposed the famous Smagorinsky eddy viscosity model [15], which marked the beginning of Large Eddy Simulation of turbulence. The Smagorinsky model was improved by Lilly [16], who calculated the value of the Smagorinsky's constant based on three-dimensional isotropic turbulence. Chollet and Lesieur [17] used the spectral eddy viscosity to develop LES in spectral space, which allows for conquering the scale-separation phenomenon. This technique was modified by Ducros *et al.* [18] for application to shear flows. Later, Germano and co-workers ([12] and [19]) developed a physical-space eddy-viscosity concept, in which the Smagorinsky constant was dynamically evaluated through a double filtering, which is used in the present study.

Among the present techniques for studying turbulent structures, POD is selected in this research. POD, which is also known as the *Karhunen–Loéve* Expansion, was developed by several researchers (e.g.

[4], [5], [20] and [21]) and in different fields: turbulent flow analysis, meteorology, structural vibrations, image processing and signal analysis. POD was first proposed for the study of turbulence by Lumley [4]. Sirovich [5] developed the snapshot POD method based on the *Karhunen–Loéve* Expansion. This method has much less computational cost than the direct computation of POD, and therefore is being used in this study. Aubry *et al.* [6] proposed the idea of constructing low-dimensional models that exhibit most of the coherent properties of the flow. Berkooz *et al.* [22] performed a comprehensive assessment of POD and its abilities for turbulence structural analysis. POD has since been extensively used for many turbulence flow studies. Some of the alternatives to POD method are coherent structure tracking (CST) which was developed by Scouten [23], linear-stochastic estimation (LSE) by Adrian [24] and wavelet transformation by Brown *et al.* [25]. Among all the existing techniques, POD was proven to be more powerful in terms of the level of details it reveals when it comes to the study of coherent structures. Due to the memory limitations of computers in the past, the majority of POD analysis was performed on two-dimensional sampling planes. But the growth of computer technologies could remove this computational limitation and can make three-dimensional POD analysis possible in the near future.

There have been a number of high resolution numerical and experimental studies of viscous incompressible flow past a square cylinder. Rodi [14] performed a comprehensive LES study of flow past different types of bluff-bodies including a long square cylinder. Norberg [26] conducted an experimental investigation of flow around rectangular cylinders at a range of Reynolds numbers from 400 to 30,000. Later, Sohankar *et al.* [27] presented a high fidelity Direct Numerical Simulation (DNS) of two- and three-dimensional unsteady flow around a square cylinder at Re = 150 - 500. The same group also performed LES of flow past a square cylinder at a higher Reynolds number (Re = 22,000) [28].

The study of the energetic topologies by the use of POD has attracted specific attention in recent years. The energetic flow structures in the wake region of an infinite circular cylinder have been extracted by POD [30]. Van Oudheusden *et al.* [31] characterized the coherent wake flow and extracted the shedding phase of the velocity field for a flow past a square cylinder at relatively high Reynolds number

(*Re* = 10,000). Results for three-dimensional flow past a square cylinder confined between two parallel walls is documented in [32]. Perrin *et al.* [8] extracted the first three dominant structures in the wake region of an infinite circular cylinder. Giordano *et al.* [33] used the data obtained from particle image velocimetry (PIV) measurements of both infinite and finite circular cylinder flows to perform POD analysis. Their main focus was on the study of vortex shedding and velocity structures in the wake region. Frederich *et al.* [9] conducted LES for a finite wall-mounted circular cylinder to investigate the large-scale dynamics of the flow in the wake region.

Notwithstanding the comprehensive studies on an infinite square cylinder in a free stream and the existence of high resolution numerical and experimental results, the study of the energetic coherent structures and analysis of the wake is not yet complete. The existing literature, e.g. [31], does not go that deep into the analysis of the temporal coefficients and is limited in terms of the number of modes used to reconstruct the flow. A significant aspect of this study compared to previous studies is to perform POD analysis for a low Reynolds number, yet turbulent wake flow where experimental data are available for validation (e.g. [26] and [34]). Also, the lower Reynolds number enables larger time gaps between the time steps and therefore the input database for POD analysis covers more time history of the flow (due to memory limitations, the number of snapshots cannot be too large). In addition, the present study emphasizes the temporal coefficients and tracks the variation of the energetic modes and attempts to determine the physical meaning of each mode.

For an infinite cylinder in proximity to a solid wall, there are a number of previous experimental and numerical studies, both in terms of circular and square geometries. A comprehensive experimental study for a high Reynolds number (*Re* = 45,000) flow around a circular cylinder in proximity to a wall, and for gap-to-diameter ratios in the range of 0.2 to 0.4 was performed by Bearman *et al.* [35]. Later, Bailey *et al.* [36] performed a similar experimental study of a square cylinder for different gap-to-diameter ratios at a Reynolds number of *Re* = 19,000. They classified the wake flow into three distinct regimes based on the gap width and defined a critical gap for which vortex shedding is suppressed due to presence of wall. This

critical gap-to-diameter ratio was also investigated by Bosch *et al.* [37], Durao *et al.* [38] and Martinuzzi *et al.* [39] using different approaches. Later, Price *et al.* [40] extended that study by classifying the flow into four regimes based on the gap width and boundary layer thickness.

Despite the previous studies on cylinders in proximity to a solid wall, investigation of the wake flow characteristics and topologies caused by solid wall and bluff body is far from complete. Wang *et al.* [41] studied the flow characteristics in the near-wake of a circular cylinder by the use of a vortex identification method. Later, Lin *et al.* [42] examined these flow characteristics in more detail for a wide range of gap-to-diameter ratios (0.0 to 4.0). They also investigated the mechanism of vortex shedding suppression (for circular cylinder cases). In a recent study by Shi *et al.* [43], the wake flow characteristics of a square cylinder in proximity to a solid wall was investigated by the use of POD. The database for the POD analysis was obtained for gap-to-diameter ratios in the range of 0.1 to 0.8 by time-resolved particle image velocimetry (TR-PIV) measurements at high temporal resolution.

Previous studies of rib-roughened channel flow are more focused on pressure-driven flows, rather than wall driven Couette flows. Miyake *et al.* [44] conducted a DNS study of pressure-driven channel flow with transverse rib roughness on both walls. Later, Ikeda and Durbin [45] performed DNS of a configuration with uneven rib heights. Cui *et al.* [46] conducted an LES study to investigate mean and instantaneous flow structures of pressure driven flow in a rib roughened channel for different element spacing. A series of studies by Leonardi and co workers (e.g. [47-48]) used DNS to study turbulent channel flow with a rib-roughened wall for a wide range of w/k values, where w is the separation distance between the rib elements and k is the rib height. Krogstad *et al.* [49] studied a fully turbulent pressure-driven symmetric channel flow for cases with smooth walls and rod-roughness on both walls using both hot-wire anemometry and DNS. They also assessed the turbulence structure in terms of the Reynolds stress ratios and anisotropy tensor. Similar symmetric configurations have been studied by other authors, e.g., Bakken *et al.* [50] and Ashrafian *et al.* [51]. Orlandi *et al.* [52] conducted a DNS study to investigate the effect of element shape and orientation on the turbulence structure. Later, Burattini *et al*. [53]

performed simultaneous experimental and numerical analyses of asymmetric channel flow with roughness on one wall for a range of Reynolds numbers. They extensively studied the statistical moments of the velocity fluctuations, turbulent length scales and energy spectra, and their variation with Reynolds number.

Notwithstanding previous numerical and experimental results on pressure driven channel flows, the study of turbulent Couette flow on roughened surfaces is far from complete. In two experimental studies by Aydin and Leutheusser [54-55] plane Couette flows with two smooth walls and with two rough walls were analysed in detail. They compared the mean velocity distribution and turbulent intensities between the smooth and rough wall cases; the flow was symmetric for both cases. Papavassiliou *et al.* [56] conducted a DNS study of a plane Couette flow to investigate large scale secondary flow structures, which are not be observed in pressure-driven flows. Wang and Bergstrom [57] applied and validated LES for a simulation of turbulent Couette flow for a similar Reynolds number.

The existing literature on analyzing the large-scale dominant structures in turbulent Couette channel flow and interaction of flow topologies associated with the wall and bulk flow is limited. Moehlis *et al.* [58] investigated coherent structures in a plane Couette flow using POD. Their work was later extended by Smith *et al.* [59] to obtain a low-dimensional model in a minimal flow unit. Tsukahara *et al.* [60] extracted three-dimensional spatial POD modes from a DNS analysis of a plane Couette flow.

To the author's knowledge no one has yet studied plane Couette flow with rib roughness on one wall, which is the main difference of the present work with previous studies. Another contribution of this study is to analyze the large-scale velocity structures in turbulent Couette channel flow and the flow topology associated with the roughness elements using POD, which has not been done in the past. Lastly, a new insight into the temporal coefficients' life cycles has been introduced which may encourage new development ideas in POD analysis of turbulent channel flows.

1.6 Thesis Outline

This manuscript-based dissertation consists of five chapters; each chapter has its own individual reference list.

Chapter 2 presents the study case of flow around an infinite cylinder of square cross section. It starts with a literature review, followed by the numerical methodology and flow set-up details. Choosing a common geometry made it possible to validate the LES simulations before performing POD analysis. Large-scale velocity structures and their corresponding energy content in the wake region were investigated on sampling planes in two directions and ultimately, the ability of POD in reconstructing a turbulent wake flow was examined. The results was documented and submitted to the *International Journal of Fluid Mechanics Research.*

In chapter 3 the effect of a solid wall on the wake dynamics of an infinite square cylinder was investigated. Unlike chapter 2, this study case emphasizes less on LES verifications and focuses more on POD analysis. The flow structures associated with the proximity of wall were analyzed, compared to the benchmark study and the results were documented and submitted to the *10th International ERCOFTAC Symposium on Engineering Turbulence Modeling and Measurements*.

Chapter 4 presents the last study case, study of coherent structures in a turbulent Couette flow with rib-shaped roughness elements on one wall. It starts with literature reviews on pressure-driven flows with rib-roughened walls and Couette flows with rough and smooth walls. Then, the literature on POD analysis of plane Couette flows and rib-roughened Poiseuille flows is reviewed. Numerical methodology and flow set-up details are presented next. Flow simulation results are presented in detail and comparison of flow over rough and smooth walls are discussed. At the end, topologies of the coherent structures generated by the rough and smooth walls are investigated on sampling planes in two directions. A comparison is made to the first two study cases and the results were documented and submitted to the *International Journal of Heat and Fluid Flow.*

Conclusions and recommendations for future extension are presented in Chapter 5. At the end, results of a separate side work, the study of a turbulent lid-driven cavity flow, are briefly presented in Appendix. The relevance of this subject to the case study 3, which is the motivation of this side study, was explained first. The results were primarily prepared for the *7th International Symposium on Turbulence, Heat and Mass Transfer* in Sicily, Italy (September 2012), and later an extended work was submitted to the *Journal of Turbulence*.

References:

[1] P. A. Davidson, Y. Kaneda, K. Moffat, K. R. Sreenivasan, *A Voyage Through Turbulence.* Cambridge University Press, 2011.

[2] W. K. George, *Lectures in Turbulence for the 21st Century*, Chalmers University of Technology, Gothenburg, Sweden, 2008.

[3] J.H. Ferziger and M. Perić, *Computational Methods for Fluid Dynamics*, Springer-Verlag, New York, 2002.

[4] J. L. Lumley, "The structure of inhomogeneous turbulence." *Atmospheric Turbulence and Radio Wave Propagation*: edited by A. M. Yaglom and V. I. Tararsky, Nauka, Moscow, 166–178, 1967.

[5] L. Sirovich, "Turbulence and the dynamics of coherent structures." Parts I, II and III. *Quarterly of Applied Mathematics*, 45: 561-571 and 573-590, 1987.

[6] N. Aubry, P. Holmes, J. L. Lumley and E. Stone, "The dynamics of coherent structures in the wall region of a turbulent boundary layer." *Journal of Fluid Mechanics* 192:115-173 1988.

[7] W. Cazemier, *Proper orthogonal decomposition and low dimensional models for turbulent flows*, Rijksuniversiteit Groningen, 1997.

[8] R. Perrin, M. Braza, E. Cid, S. Cazin, P. Chassaing, C. Mockett, T. Reimann and F. Thiele, "Coherent and turbulent process analysis in the flow past a circular cylinder at high Reynolds number." *Journal of Fluids and Structures*, 24: 1313-1325, 2008.

[9] O. Frederich, J. Scouten, D.M. Luchtenburg and F. Thiele, *Large-scale dynamics in the flow around a finite cylinder with ground plate.* The Sixth International Symposium on Turbulence and Shear Flow Phenomena. Seoul, Korea, June 22-24, 2009.

[10] M. Einian, *Large Eddy Simulation of Flow around a Finite Square Cylinder*, PhD thesis, University of Saskatchewan, 2012.

[11] M. Lesieur, O. Metais and P. Comte, *Large-Eddy Simulations of Turbulence*, Cambridge University Press, 2005.

[12] M. Germano, U. Piomelli, P. Moin and W. Cabot, "A dynamic subgridscale eddy-viscosity model." *Physics of Fluids* A 3(7): 1760–1765, 1991.

[13] B. –C. Wang and D. J. Bergstrom., "A general optimal formulation for the dynamic Smagorinsky subgrid-scale stress model." *International Journal for Numerical Methods in Fluids*, 49(12): 1359-1389, 2005.

[14] L. F. Richardson, *Weather Prediction by Numerical Process*, Cambridge University Press, 1922.

[15] J. Smagorinsky, "General circulation experiments with the primitive equations." *Monthly Weather Review*, 91(3): 99–164, 1963.

[16] D. K. Lilly, *The representation of small-scale turbulence in numerical simulation experiments*, Proceedings of the IBM Scientific Computing Symposium on Environmental Sciences: 195–210, Yorktown Heights, NY, 14-16 November 1966.

[17] L. P. Chollet and M. Lesieur, "Parameterization of small scales of three-dimensional isotropic turbulence utilizing spectral closures." *Journal of Atmospheric Science*, 38: 2747–2757, 1981.

[18] F. Ducros, P. Comte and M. Lesieur, "Large-eddy simulation of transition to turbulence in a boundary layer developing spatially over a flat plate." *Journal of Fluid Mechanics* 326: 1–36, 1996.

[19] M. Germano, "Turbulence, the filtering approach." *Journal of Fluid Mechanics* 238: 325–336, 1992.

[20] M. M. Loève, *Probability Theory*, Princeton, N.J., VanNostrand, 1955.

[21] K. Ball, K. Sirovich and L. Keefe, "Dynamical eigenfunction decomposition of turbulent channel flow", *International Journal for Numerical Methods in Fluids,* 12: 585-604, 1991.

[22] G. Berkooz, P. Holmes and J. L. Lumley, "The proper orthogonal decomposition in the analysis of turbulent flows." *Annual Review of Fluid Mechanics* 25: 539–575, 1993.

[23] J. Scouten, *Coherent structure tracking with application to the wake flow behind a wall-mounted finite circular cylinder*, TU Berlin, 2009.

[24] R. Adrian, "Conditional eddies in isotropic turbulence", *Physics of Fluids*, 22(11): 2065-2070, 1979.

[25] G. Brown and A. Roshko, "On density effects and large structure in turbulent mixing layer", *Journal of Fluid Mechanics*, 64: 775-816, 1974.

[26] C. Norberg, "Flow around rectangular cylinders: Pressure forces and wake frequencies", *Journal of Wind Engineering and Industrial Aerodynamics*, 49: 187-196, 1993.

[27] A. Sohankar, C. Norberg and L. Davidson, "Simulation of three-dimensional flow around a square cylinder at moderate Reynolds numbers." *Physics of Fluids*, 2: 288-306, 1999.

[28] A. Sohankar, L. Davidson and C. Norberg, "Large Eddy Simulation of Flow Past a Square Cylinder: Comparison of Different Subgrid Scale Models." *ASME Journal of Fluids Engineering*, 122: 39-47, 2000.

[29] W. Rodi, "Large-eddy simulations of the flow past bluff bodies; state of the art." *JSME International Journal*, Series B, 41(2): 361-374, 1998.

[30] X. Ma and G.E. Karniadakis, "A low-dimensional model for simulating three-dimensional cylinder flow." *Journal of Fluid Mechanics*, 458: 181-190, 2002.

[31] B. W. Van Oudheusden, F. Scarano, N. P. Van Hinsberg and D. W. Watt, "Phase-resolved characterization of vortex shedding in the near wake of a square-section cylinder at incidence." *Experiments in Fluids,* 39: 86-98, 2005.

[32] M. Buffoni, S. Camarri, A. Iollo and M.V. Salvetti, "Low-dimensional modelling of a confined three-dimensional wake flow." *Journal of Fluid Mechanics*, 569: 141-150, 2006.

[33] R. Giordano, T. Astarita and G. M. Carlomagno, *Vortex shedding in the near wake of a finite cylinder*. The 14th International Symposium on Applications of Laser Techniques to Fluid Mechanics, Lisbon, Portugal, July 7-10, 2008.

[34] S. Dutta, P. K. Panigrahi and K. Muralidhar, "Experimental Investigation of Flow Past a Square Cylinder at an Angle of Incidence" *ASCE Journal of Engineering Mechanics*, 134: 788-803, 2008.

[35] P. W. Bearman and M. M. Zdravkovich, "Flow around a circular cylinder near a plane boundary." *Journal of Fluid Mechanics*, 89: 33-47, 1978.

[36] S. C. C. Bailey, G. A. Kopp and R. J. Martinuzzi, "Vortex shedding from a square cylinder near a wall." *Journal of Turbulence* 3: 1-18, 2002.

[37] G. Bosch, M. Kappler and W. Rodi, "Experiments on the flow past a square cylinder placed near a wall." *Experimental Thermal and Fluid Science* 13: 292–305, 1996.

[38] D. F. Durao, P. S. T. Gouveia and J. C. F. Pereira, "Velocity characteristic of the flow around a square cross section cylinder placed near a channel wall." *Experiments in Fluids* 11: 341–350, 1991.

[39] R. J. Martinuzzi, S. C. C. Bailey, G. A. Kopp, "Influence of wall proximity on vortex shedding from a square cylinder." *Experiments in Fluids* 34: 585–596, 2003.

[40] S. J. Price, D. Sumner, J. G. Smith, K. Leong and M. P. Païdoussis, "Flow visualization around a circular cylinder near to a plane wall." *Journal of Fluids and Structures*, 16 (2): 175–191, 2002.

[41] X. K. Wang and S. K. Tan, "Near-wake flow characteristics of a circular cylinder close to a wall." *Journal of Fluids and Structures*, 24: 605-627, 2008.

[42] W.-J. Lin, C. Lin, S.-C. Hsieh and S. Dey, "Flow characteristics around a circular cylinder placed horizontally above a plane boundary." *Journal of Engineering Mechanics*, 135: 697-715, 2009.

[43] L. L. Shi, Y. Z. Liu and J. J. Wan, "Influence of wall proximity on characteristics of wake behind a square cylinder: PIV measurements and POD analysis." *Experimental Thermal and Fluid Science* 34: 28–36, 2010.

[44] Y. Miyake, K. Tsujimoto and Y. Agata, "A DNS of a turbulent flow in a rough-wall channel using roughness elements model." *JSME International Journal*, Series B 43 (8): 233–242, 2000.

[45] T. Ikeda and P. A. Durbin, *Direct simulations of a rough-wall channel flow*. Report TF-81, Department of Mechanical Engineering, Stanford University, 2002.

[46] J. Cui, C. P. Virendra and L. Ching-Long, "Large-eddy simulation of turbulent flow in a channel with rib roughness." *International Journal of Heat and Fluid Flow*, 24: 372–388, 2003.

[47] S. Leonardi, P. Orlandi, R. J. Smalley, L. Djenidi, and R. A. Antonia, "Direct numerical simulation of turbulent channel flow with transverse square bars on one wall", *Journal of Fluid Mechanics*, 491:229–238, 2003.

[48] S. Leonardi, P. Orlandi, L. Djenidi and R. A. Antonia, "Structure of turbulent channel flow with square bars on one wall." *International Journal of Heat and Fluid Flow*, 25: 384–392, 2004.

[49] P.-Å. Krogstad, H. I. Andersson, O. M. Bakken and A. Ashrafian, "An experimental and numerical study of channel flow with rough walls", *Journal of Fluid Mechanics*, 530: 327–352, 2005.

[50] O. M. Bakken, P.-Å. Krogstad, A. Ashrafian and H. I. Andersson, "Reynolds number effects in the outer layer of the turbulent flow in a channel with rough walls" *Physics of Fluids*, 17, 065101, 2005.

[51] A. Ashrafian and H. I. Andersson, "The structure of turbulence in a rod-roughened channel" *International Journal of Heat and Fluid Flow*, 27: 65–79, 2006.

[52] P. Orlandi, S. Leonardi and R. A. Antonia, "Turbulent channel flow with either transverse or longitudinal roughness elements on one wall" *Journal of Fluid Mechanics*, 561: 279–305, 2006.

[53] P. Burattini, S. Leonardi, P. Orlandi and A. Antonia, "Comparison between experiments and direct numerical simulations in a channel flow with roughness on one wall" *Journal of Fluid Mechanics*, 600: 403–426, 2008.

[54] E. M. Aydin and H. J. Leutheusser, *Experimental investigation of turbulent plane Couette flow*, ASME Forum on Turbulent Flows FED, Cincinnati, OH, June 14-17, 1987.

[55] E. M. Aydin and H. J. Leutheusser, "Plane-Couette flow between smooth and rough walls" *Experiments in Fluids*, 11: 302-312, 1991.

[56] D. V. Papavassiliou and T. J. Hanratty, "Interpretation of large-scale structures observed in a turbulent plane Couette flow" *International Journal of Heat and Fluid Flow*, 18: 55-69, 1997.

[57] B-C. Wang and D. J. Bergstrom, "A dynamic nonlinear subgrid-scale stress model" *Physics of Fluids*, 17, 035109, 2005.

[58] J. Moehlis, T. R. Smith, P. Holmes and H. Faisst, "Models for turbulent plane Couette flow using the Proper Orthogonal Decomposition", *Physics of Fluids*, 14: 2493-2507, 2002.

[59] T. R. Smith, J. Moehlis and P. Holmes, "Low-dimensional models for turbulent plane Couette flow in a minimal flow unit", *Journal of Fluid Mechanics*, 538: 71–110, 2005.

[60] T. Tsukahara, K. Iwamoto and H. Kawamura, *POD analysis of large-scale structures through DNS of turbulent plane Couette flow*, Advances in Turbulence XI, Proceeding 11th EUROMECH Turbulence Conference: 245-247, Porto, Portugal, June 25-28, 2007.

Chapter 2

Capturing the Large-scale Dynamics in the Wake of an Infinite Square Cylinder using Proper Orthogonal Decomposition

A similar version of this chapter has been submitted as:

- M. Samani, M. Einian and D.J. Bergstrom, "Capturing the large-scale dynamics in the wake of an infinite square cylinder using Proper Orthogonal Decomposition", *International Journal of Fluid Mechanics Research* (Under Review).

  The flow simulation results and POD analysis were performed by the main author. Partial development of the LES code was contributed by the co-authors.

In addition, a part of this chapter was presented at the following conference:

- M. Samani, M. Einian, D.J. Bergstrom, *Use of Proper Orthogonal Decomposition to Investigate the Large-Scale Dynamics in the Wake Region of an Infinite Square Cylinder*, 18th Annual Conference of the CFD Society of Canada, London, ON, Canada, May 17-19, 2010.

  The flow simulation results and POD analysis were performed by the main author. Partial development of the LES code was contributed by the first co-author and partial development of the POD routine formulation as well as initiating the LES code were performed by the second co-author.

Preamble:

The first step to simulate turbulent flow over rib-roughened surfaces is to validate the LES approach and most importantly verify the POD algorithm. To this end, a proper starting point is to examine the wake flow behind a square cylinder, and then add a nearby wall and next place the cylinder on the wall (which resembles a single rib), which is studied in an independent study in step 2. Finally, to make a sequence of those obstacles to resemble a rough surface, this is the ultimate target of this thesis.

Another benefit of choosing this common geometry for the first step is that because a number of experimental and high fidelity numerical studies are available for comparison, the used LES technique and POD algorithm can be verified and validated for next steps.

Another contribution of this chapter to the overall study is to establish a benchmark for comparison to more complicated cases in the next steps. As a result, this chapter equally concentrates on an upfront validation of LES and POD and smoothes the way for the next step.

Abstract

In this work, Proper Orthogonal Decomposition (POD) is applied to determine the large-scale three-dimensional space and time dependent flow structures in the near-wake region of an infinite square cylinder. One purpose of this study is to establish a benchmark for comparison to the more complicated case of flow over a rib-roughened surface. The three-dimensional velocity field obtained from a low resolution Large Eddy Simulation (LES) of the flow around an infinite square cylinder at a Reynolds number of $Re = 500$ is used as the input data for the POD analysis. The finite-volume method was used to discretize the filtered Navier-Stokes equations on a non-uniform collocated grid. A two-step fractional step method was used to solve the discrete equations, and a pressure correction method was used to ensure mass conservation. For the POD analysis, streamwise and wall-normal velocity components along with spanwise vorticity are used as the computational variables. The energy of the flow was found to be well captured by only a small number of eigenmodes, and the flow cycle can be accurately reconstructed using less than 60 eigenmodes. Qualitative analysis of the dominant modes provides insight as to the large-scale structures in the wake and their interaction with the developed turbulence in the outer flow.

2.1 Introduction

The external incompressible flow around an infinite cylinder of square cross section is a standard topic in the study of bluff body flows. The term “infinite” refers to the case when cylinder’s end effects are negligible. Although it is possible to find many numerical works related to the analysis of the infinite cylinder, studies on characterizing the coherent structures of this flow are more limited. In spite of the simple two-dimensional geometry, the turbulent wake is highly unsteady and three-dimensional. From an engineering perspective, the study of square cylinder flows is of interest as a proto-typical bluff-body

flow with applications such as the flow over long slender beams. For flows around bluff bodies with sharp corners, e.g. a square cylinder, cube or diamond, the geometry predetermines the separation point and therefore the "*numerical solution becomes less sensitive to modeling in the near-wall region*" [1]. At very low Reynolds numbers, a steady two-dimensional, symmetric, fully-attached flow pattern is observed. As the Reynolds number is increased to about $Re = 50$, the flow separation occurs at the rear corners of the cylinder, but the flow stays laminar, steady and two-dimensional. Further increasing the Reynolds number causes disappearing of the upstream-downstream symmetry and a pair of symmetric vortices forms behind the cylinder. These vortices or eddies grow longer with increasing Reynolds number. As the Reynolds number increases beyond the critical value ($Re = 125$), the flow separation starts moving towards the leading corners until the Reynolds number reaches $Re = 175$ [2]. Further increasing the Reynolds number causes antisymmetric and time-dependent motions to develop in the flow. For the infinite cylinder case, the wake flow is dominated by the time-periodic phenomenon of Kármán vortex shedding from the sides of the cylinder. The study of vortex shedding is an important application for research on flow control since it leads to sharp changes in the instantaneous drag, lift and vibration forces.

Due to the geometrical simplicity and phenomenon of flow separation, the viscous flow past an infinite square cylinder has been extensively studied over the past two decades. A Direct Numerical Simulation (DNS) of two- and three-dimensional unsteady flow around a square cylinder was performed in [2]. In general, their results were in a good agreement with existing experiments. The LES results for the flow past different types of bluff-bodies including a long square cylinder were documented in [3]. LES of flow past a square cylinder at a higher Reynolds number ($Re = 22{,}000$) was reported in [4]. A comparison between three different subgrid-scale (SGS) models, i.e. the Smagorinsky, dynamic Smagorinksy and dynamic one-equation model, was presented in their work.

In the context of the study of wake flows, the identification of the most-energetic flow topologies has attracted specific attention in recent years, and proper orthogonal decomposition (POD) has been extensively used to analyze the constituent topologies. A high-resolution direct numerical simulation (DNS) database was employed by by Ma and Karniadakis [5] to extract the most-energetic flow structures in the wake region of an infinite circular cylinder. POD was used to build a low-order model for two-dimensional flow past a square cylinder at incidence in [6]. They characterized the coherent wake flow unsteadiness and extracted the shedding phase of the velocity fields, by using mean and first two dominant modes. Buffoni *et al*. [7] studied a more complex three-dimensional flow past a square cylinder placed between two parallel walls. Advanced time resolved particle image velocimetry (TRPIV) measurements of flow past an infinite circular cylinder were performed by Perrin *et al.* [8] and they used the data to identify the first three dominant structures in the wake region based on POD. The dependence of the POD results on the domain size is also discussed in their work. PIV measurements of both infinite and finite circular cylinder flows were performed by Giordano *et al.* [9] to obtain input data for POD analysis. Their main focus was on the study of vortex shedding and velocity structures of the wake region. Frederich *et al.* [10] conducted LES for a finite circular wall-mounted cylinder to investigate the large-scale dynamics of the flow in the wake region. They characterized the flow features using two approaches: POD and Coherent Structure Tracking (CST).

The present study focuses on investigating the large-scale velocity structures and their corresponding energy content in the wake region of an infinite square cylinder. The Reynolds number based on the approach-flow velocity and cylinder edge-length ($U_\infty D/\nu$) was set to Re = 500. Here U_∞ is the approach-flow velocity, D is the cylinder edge-length and ν is the dynamic viscosity of the fluid. The flow results from LES are decomposed into orthogonal eigenmodes using the snapshot POD method of Sirovich [12]. The POD analysis specifically considers the two-dimensional velocity components and vorticity for plane sections in the wake region which are aligned perpendicular and parallel to the free stream flow.

2.2 Numerical Methodology

2.2.1 Flow configuration and LES:

For the purpose of generating a full-order database for the POD analysis, LES is utilized in this study. LES calculates the large-scale motions directly, and approximates the small-scale motions using a SGS model. For LES, the incompressible Navier-Stokes (NS) and continuity equations (for a Newtonian flow with constant properties) are implicitly filtered with a spatial filter of characteristic width (Δ), so that the governing equations become

$$\frac{\partial \overline{\boldsymbol{u}}_{\boldsymbol{i}}}{\partial t} + \frac{\partial (\overline{\boldsymbol{u}}_{\boldsymbol{i}} \overline{\boldsymbol{u}}_{\boldsymbol{j}})}{\partial \boldsymbol{x}_{\boldsymbol{j}}} = -\frac{1}{\rho}\frac{\partial p}{\partial \boldsymbol{x}_{\boldsymbol{i}}} + \nu \frac{\partial^2 \overline{\boldsymbol{u}}_{\boldsymbol{i}}}{\partial \boldsymbol{x}_{\boldsymbol{j}} \partial \boldsymbol{x}_{\boldsymbol{j}}} - \frac{\partial \tau_{ij}}{\partial \boldsymbol{x}_{\boldsymbol{j}}} \tag{2.1}$$

and

$$\frac{\partial \overline{\boldsymbol{u}}_{\boldsymbol{i}}}{\partial \boldsymbol{x}_{\boldsymbol{i}}} = 0, \tag{2.2}$$

where $\overline{\boldsymbol{u}}_{\boldsymbol{i}}$ is the filtered velocity component, t is the time, p is the local pressure, ρ is the fluid density, $\boldsymbol{x}_{\boldsymbol{i}}$ is the corresponding Cartesian coordinate and τ_{ij} is the so-called subgrid-scale stress (SGS) term, which is given by

$$\tau_{ij} = \overline{\boldsymbol{u}_{\boldsymbol{i}} \boldsymbol{u}_{\boldsymbol{j}}} - \overline{\boldsymbol{u}}_{\boldsymbol{i}} \overline{\boldsymbol{u}}_{\boldsymbol{j}}. \tag{2.3}$$

A cell-centered finite-volume method was used to discretise the filtered Navier-Stokes equations on a non-uniform collocated grid. A semi-implicit Crank-Nicolson scheme was employed for the viscous terms. A two-step fractional step method was used to solve the discrete transport equations, and a pressure correction method was implemented to ensure mass conservation at each time step. The pressure correction equation was solved using a multi-grid method which accelerates the iterative solution by considering coarser grids.

Using an eddy viscosity formulation, the SGS term is expressed as

$$\tau_{ij} - \frac{1}{3}\delta_{ij}\tau_{kk} = -2\nu_{SGS}\bar{S}_{ij} \tag{2.4}$$

where δ_{ij} is the Kronecker delta, $\bar{S}_{ij}$ is the deformations tensor and ν_{SGS} is the SGS viscosity, which needs to be modeled. The present results are based on the so called Dynamic Smagorinsky (DS) model of Germano *et al.* [11]. The dynamic Smagorinsky model for the SGS eddy viscosity, ν_{SGS}, takes the form

$$\nu_{SGS} = C_s\Delta^2|\bar{S}| \tag{2.5}$$

where $\bar{S}_{ij} = \frac{1}{2}\left(\partial\overline{\boldsymbol{u}}_{\boldsymbol{i}}/\partial\boldsymbol{x}_{\boldsymbol{j}} + \partial\overline{\boldsymbol{u}}_{\boldsymbol{j}}/\partial\boldsymbol{x}_{\boldsymbol{i}}\right)$ and $|\bar{S}| = \left(2\bar{S}_{ij}\bar{S}_{ij}\right)^{\frac{1}{2}}$. In this model, C_s is determined as a variable of space and time, utilizing two filters with different characteristic scales: a grid filter and a test filter. Additional details of the mathematical formulation of this methodology can be found in [11] and [13]. In the present code, the dynamic coefficient is locally smoothed so that plane averaging of the model coefficient is not required for numerical stability.

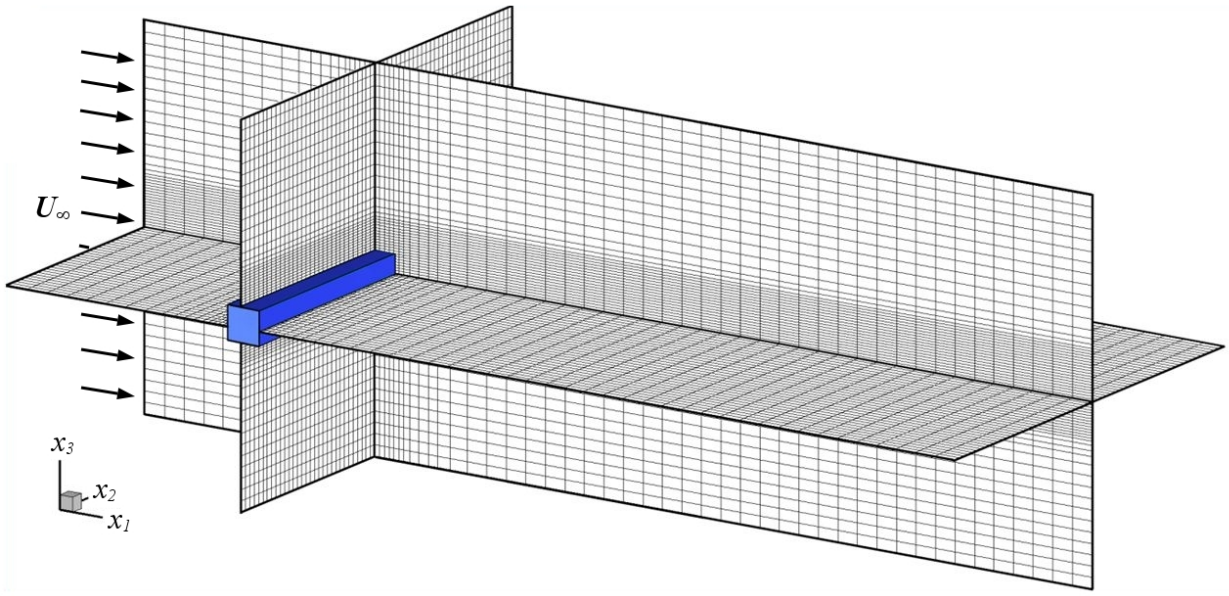

Figure 2.1: Cartesian computational grid configuration around the infinite cylinder

The physical solution domain was discretized using a rectangular 64×64×64 non-uniform grid. Figure 2.1 shows the grid configuration for the infinite cylinder. The solution domain extended 6 cylinder

widths upstream and 19 cylinder widths downstream. The spanwise (x_2) and normal (x_3) extent of the domain is 8 and 10 cylinder widths, respectively. This domain size was found to be adequate in previous LES studies, e.g., [32] and [33].

The surfaces of the cylinder were modeled as non-slip surfaces, while the upper and lower surfaces of the solution domain were modeled as slip surfaces. A uniform laminar velocity profile was used for the approach flow, while a convective boundary condition was applied at the outlet. A periodic boundary condition was implemented on the lateral surfaces of the solution domain which models a cylinder of infinite extent. Although the grid was relatively small, comparisons with other studies demonstrates that the LES accurately resolved the large-scale velocity field, which was then used for the POD analysis. Given the need for extensive time integration to obtain the database for the POD, it was efficient to follow the approach of other studies (e.g. [5]) and use a relatively small grid for the simulation.

2.2.2 Proper Orthogonal Decomposition:

Proper Orthogonal Decomposition is the methodology being used in this study to first identify the energy containing structures in the evolving dynamics, and then to reproduce the main turbulent wake structures using a finite number of modes. The basic concept of the POD methodology is straightforward: the attempt is to decompose the time-dependent fluctuating part of the flow field ($\boldsymbol{u}'(\boldsymbol{x},t)$) into a system of spatial modes ($\boldsymbol{\phi_k}(\boldsymbol{x})$) and associated temporal coefficients ($a_k(t)$), i.e.

$$\boldsymbol{u}'(\boldsymbol{x},t) = \sum_{k=1}^{K} \boldsymbol{\phi_k}(\boldsymbol{x}) a_k(t), \tag{2.6}$$

where $a_k(t)$ represents the amplitude of the spatial mode $\boldsymbol{\phi_k}(\boldsymbol{x})$ and K is the series cut-off with maximum being the total number of snapshots. For a given instantaneous field the fluctuation field can be obtained by subtracting the ensemble average $\boldsymbol{u_o}(\boldsymbol{x})$ from the instantaneous field ($\boldsymbol{u}(\boldsymbol{x},t)$), i.e.

$$\boldsymbol{u}'(\boldsymbol{x},t) = \boldsymbol{u}(\boldsymbol{x},t) - \boldsymbol{u_o}(\boldsymbol{x}). \tag{2.7}$$

The representation of equation (2.6) is not unique, i.e. there are several choices of functions $\boldsymbol{\phi_k(x)}$ such as Fourier series, Legendre or Chebyshev polynomials. The main advantage of POD over the other methods is that POD requires fewer modes to represent a system. The POD eigenfunctions are optimal with respect to energy content which means that any other set of modes contains less energy on average than the corresponding set of POD eigenfunctions. For practical applications, this property is used to determine the most energetic structures of a flow. Following the snapshot method of Sirovich [12], one can obtain the coefficients by solving an eigenvalue problem which is based on the covariance matrix of the velocity field correlating all points in the domain,

$$C_{pq} = \frac{1}{K}\int_{\Omega} \left[\boldsymbol{u}'(\boldsymbol{x}, t_p).\boldsymbol{u}'(\boldsymbol{x}, t_q)\right] d\boldsymbol{x}. \tag{2.8}$$

Here t_p and t_q are two sampling times and Ω is the POD domain. After solving the eigenvalue problem, a series of eigenvalues and corresponding eigenvectors are obtained. The eigenvalues are used to compute the energy captured by each mode. Finally, the POD vector modes can be obtained as

$$\boldsymbol{\phi(x)_k} = \int a_k(t)\, \boldsymbol{u}'(\boldsymbol{x}, t)\, dt. \tag{2.9}$$

Snapshot POD based on the above formulation is applied to two-dimensional slices of the flow field perpendicular to the cylinder axis and to the flow direction. In each plane, two-dimensional velocity and vorticity components are used as the computational data for the POD analysis. The domain chosen to perform POD analysis affects the result: in this case the POD domain extended 9*D* downstream in the wake region and 6*D* in the spanwise direction. The ensemble of 1200 snapshots extended over a time duration of 26 convective units (D/U_∞). The time step for the simulation was set to $0.001D/U_\infty$, and snapshots were taken every 20th time step. A MATLAB code was written to implement the POD algorithm based on the above formulation.

2.3 Selected Results and Discussion

2.3.1 Vortex Shedding Frequency:

To check the validity of the LES results, some global flow parameters were selected to make a comparison with the results of previous experimental and numerical studies. Time traces of the velocity and vorticity components can be used to assess the periodicity of the wake. In order to follow the evolution of the flow field, velocities, vorticity and pressure were collected from a number of numerical probes located in the wake region. Figure 2.2 illustrates a time series of the lateral velocity (u_3) and

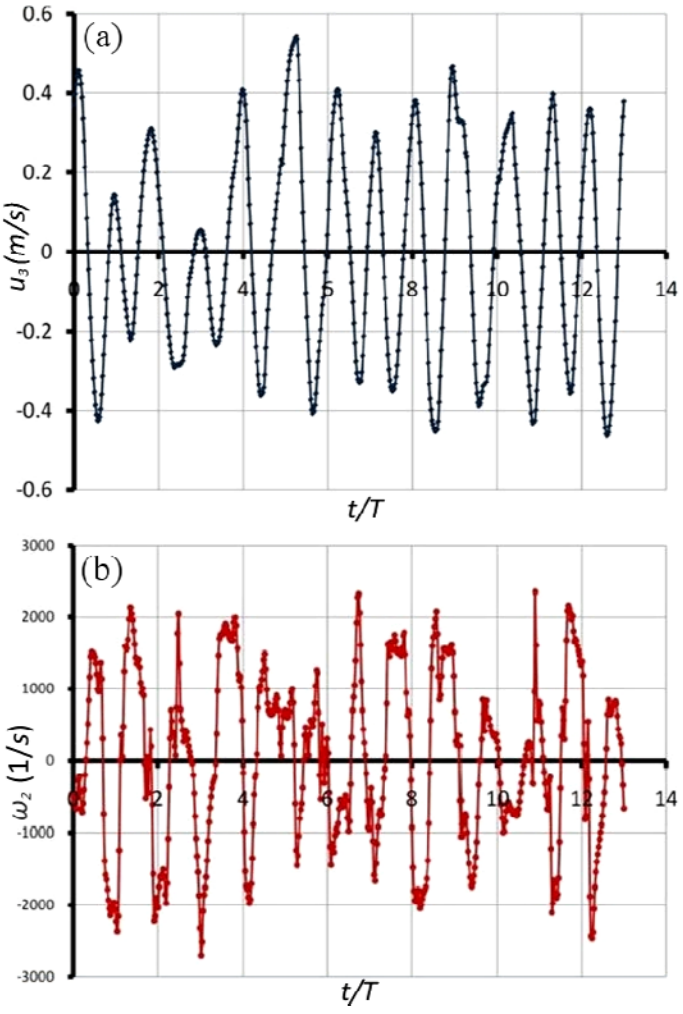

Figure 2.2: Time trace of (a) lateral velocity and (b) spanwise vorticity

spanwise vorticity (ω_2) component from a probe located $1.8D$ behind the cylinder and on the centre line. Both samples exhibit irregularly changing amplitude with zero mean. The existence of spanwise velocity fluctuations illustrates the three-dimensionality of the turbulent wake. Moreover, these signals are a clear indication of vortex shedding.

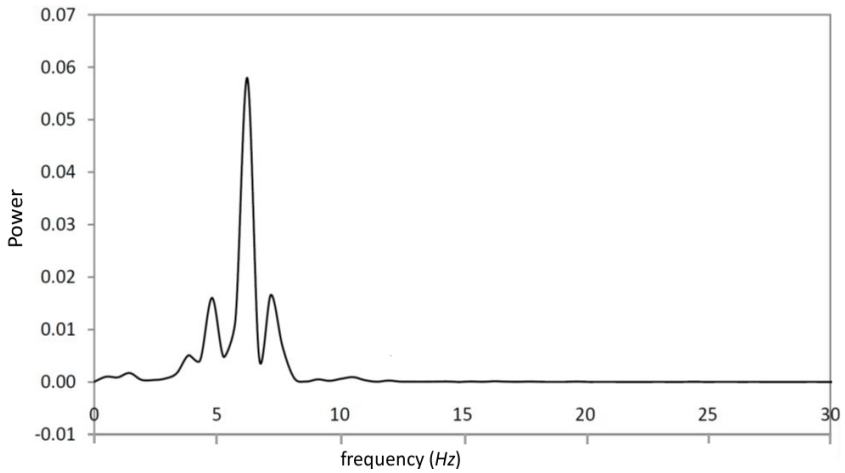

Figure 2.3: Power spectrum based on spanwise velocity component

By performing a Fast Fourier Transform (FFT) on the signals and calculating the power spectrum, the dominant shedding frequency can be identified. The frequency spectrum plotted in Figure 2.3 shows a peak in the spectrum of the spanwise velocity signal which occurs at a frequency of 6.2 Hz. Using cylinder edge-length and approach-flow velocity, this frequency corresponds to Strouhal number of $Str = fD/U_\infty = 0.122$. The same value was obtained from the frequency spectrum of other flow variables, e.g. the pressure and spanwise vorticity. The Strouhal number obtained in the present work is in a reasonable agreement with the results of other experimental and computational studies for Re = 500, e.g. $Str = 0.122 - 0.127$ (using different grids) from a DNS study by Sohankar *et al.* [2], $Str = 0.116 - 0.120$ from a DNS study by Saha *et al.* [27], $Str = 0.13$ from an experimental study by Okajima [28] for aspect ratio AR = 10 and $Str = 0.142$ from an experimental study by Lindquist [34] for AR = 40.

2.3.2 Mean and fluctuating velocity components in the wake:

Figure 2.4 shows an instantaneous flow field and the ensemble-averaged flow pattern for the infinite cylinder. The streamlines are projected onto the center normal plane and laid over the spanwise vorticity field (color contours). The instantaneous flow clearly shows the vortex shedding motion with the associated strong asymmetry. In contrast, the mean flow field reveals a region of recirculation consisting of two symmetric cells, which is in agreement with the flow visualization of circular cylinder wakes presented in previous studies (Bergmann *et al.* [15] Djenidi *et al.* [16]). Upstream of the prism, both plots show a laminar-like flow pattern.

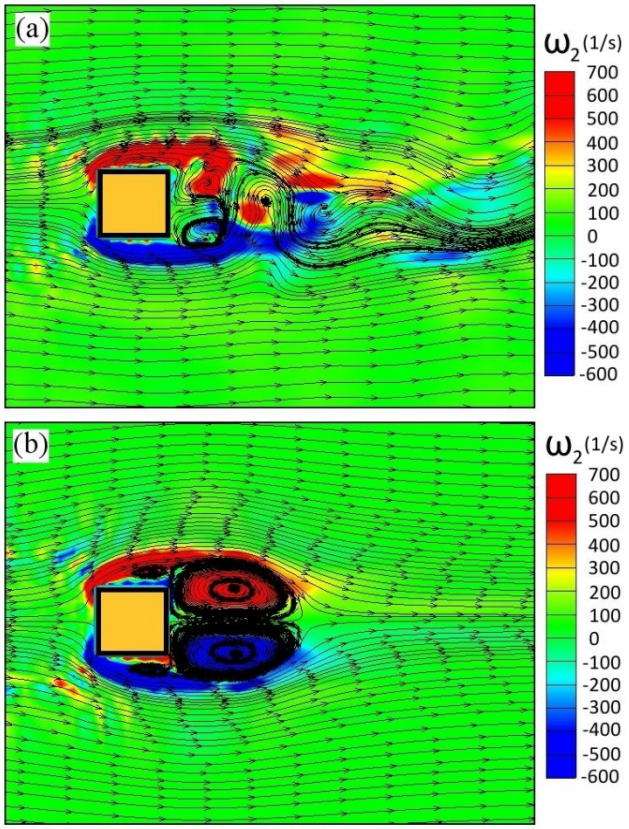

Figure 2.4: Streamlines in center plane (a) instantaneous, and (b) mean

A close-up view of the time-averaged streamlines in the vicinity of the rear corner of the prism is presented in Figure 2.5. The main recirculation vortex behind the body and secondary vortex on the

lateral side are visibly captured. Different structures are separated using different colors. The streamline pattern indicates that the reverse flow along the rear face of the cylinder separates at the rear corner, before reattaching slightly upstream. This is in accordance with previous numerical and experimental studies, e.g. [18] and [36]. Although a relatively coarse mesh is used in the present study, this figure demonstrates that the grid can successfully resolve the reverse flow near the trailing edge of the bluff body.

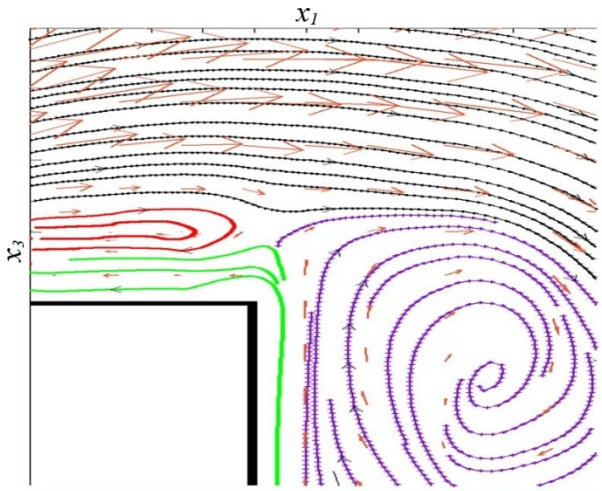

Figure 2.5: Time-averaged stream traces near rear corner of prism

The mean streamwise velocity distribution along the centerline of the wake is plotted in Figure 2.6 (a). The mean velocity was obtained by time-averaging the flow field for nearly 26 shedding cycles; the profiles were also spatially averaged along the cylinder axis. The data distribution is compared with previous studies of the square cylinder wake for different Reynolds numbers. As shown, the mean velocity is successfully resolved by this LES despite using a course grid. The time-averaged streamwise velocity distribution along lateral sections at various x_1/D locations is plotted in Figure 2.6 (b). x_1 and x_3 are measured from the center of the cylinder. For the near-wake profiles, two peaks and a minimum can be observed. The peaks are caused by the acceleration of the flow around the sides of the cylinder, which gradually diminish and completely disappear $3.7D$ from the center of cylinder. The minimum represents

the momentum deficit created by the cylinder, and persists approximately $6.7D$ downstream of the cylinder.

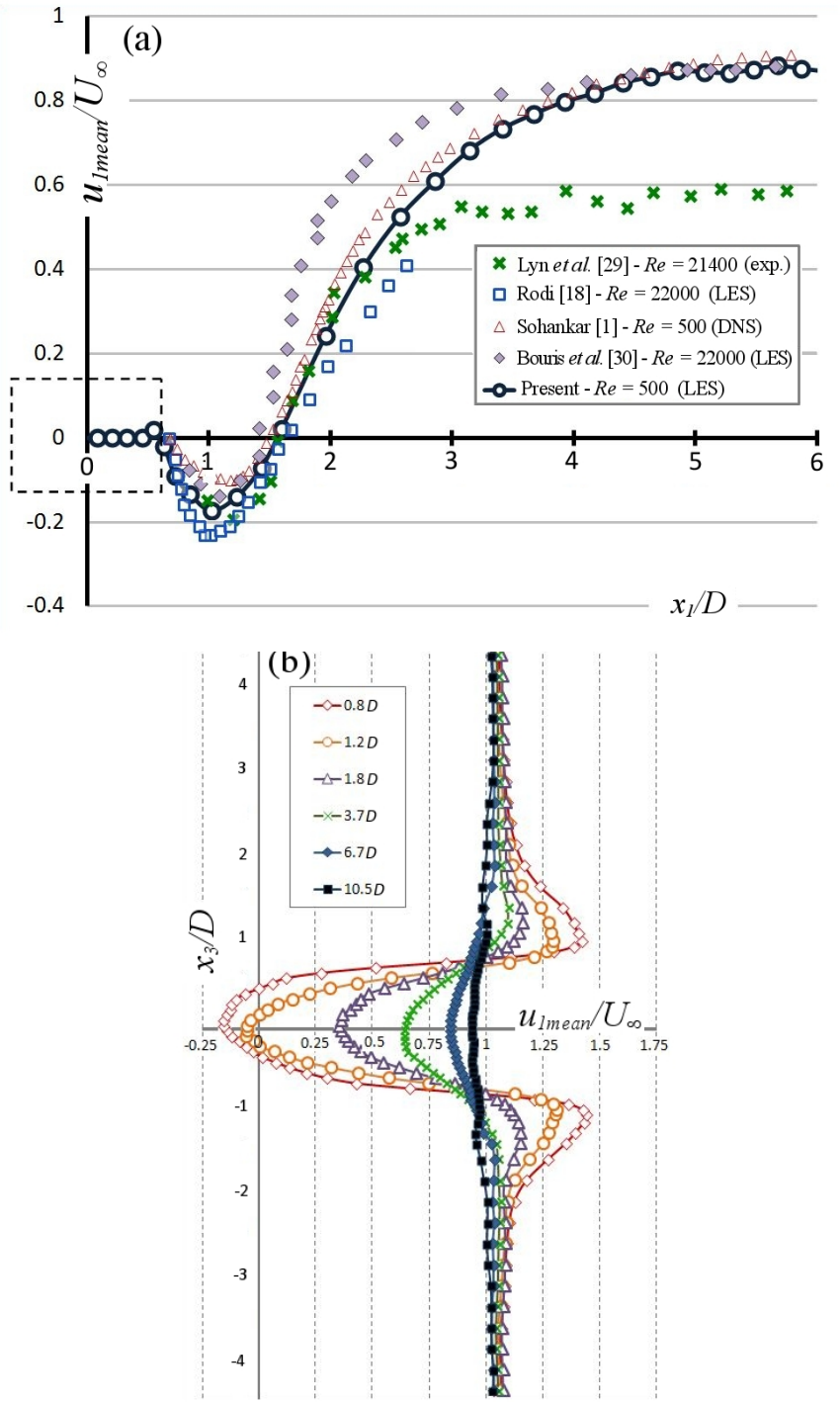

Figure 2.6: Time-averaged streamwise velocity distribution along: (a) the centerline, and (b) transverse sections in the wake

Figure 2.7 illustrates the distribution of the fluctuating energy components along the centerline and within the wake region. Since the fluctuations for the instantaneous velocity field are obtained by

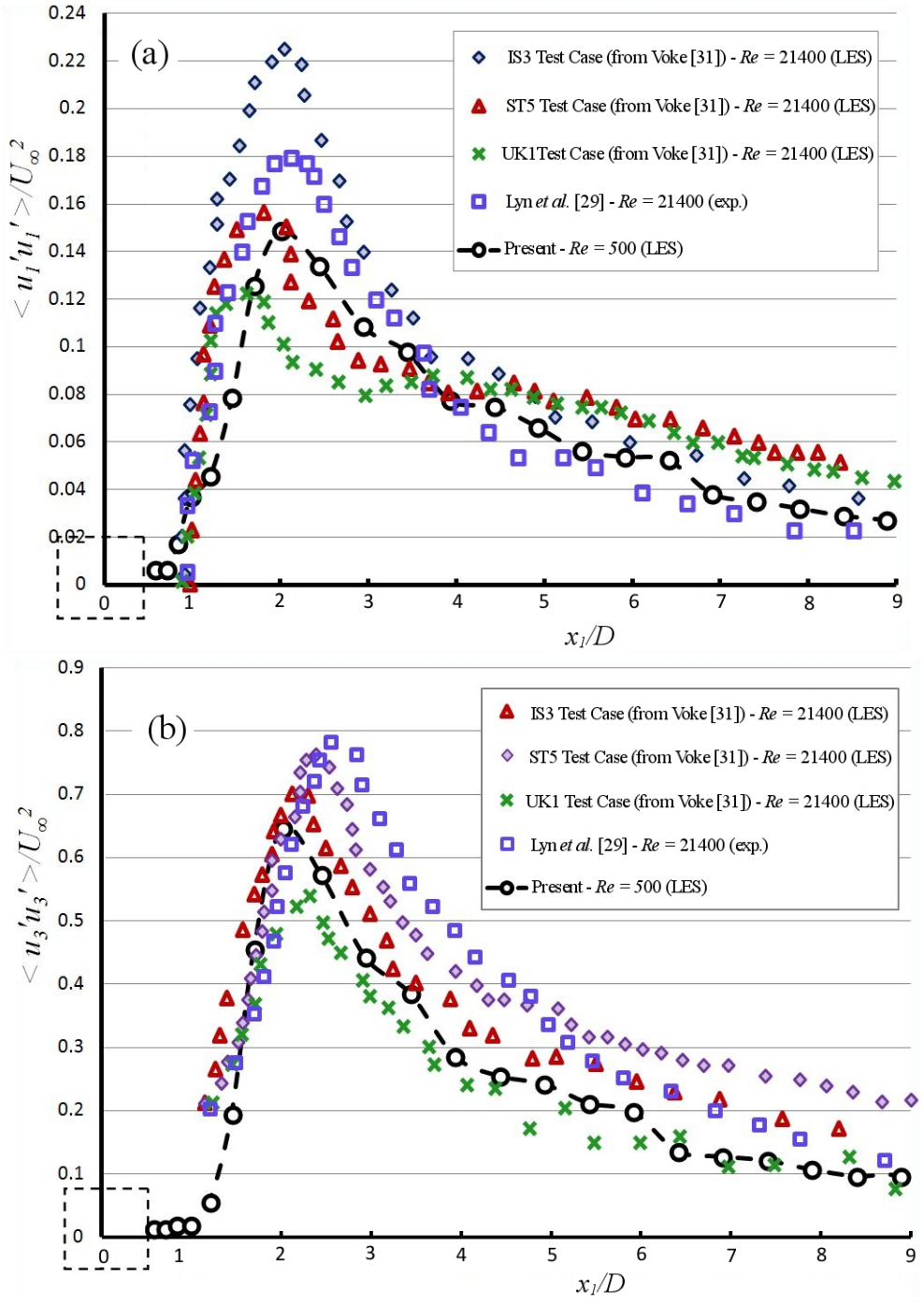

Figure 2.7: Distribution of fluctuating energy along the centerline for: (a) the streamwise velocity component, and (b) transverse velocity component

subtracting the mean velocity from the instantaneous, these fluctuations include both turbulent and periodic fluctuations. The maximum for both components occur at approximately the same location in the wake, i.e. at $x_1/D \approx 2.2$. This peak location corresponds to vortex formation length. Both profiles are compared to experimental study of Lyn *et al.* [29] and three LES study cases from Voke [31] (using the same index key, also referred in Rodi [18]). All the referred studies are mainly for higher Reynolds number since similar data for moderate/low Reynolds number is scarce.

The streamwise velocity profile within the shear layer on the top wall of the cylinder is shown in Figure 2.8. Comparison with similar experimental and numerical results (as done in Figure 2.7), shows that the separated shear layer is reasonably predicted and the simulation is observed to successfully capture the reverse flow region near the wall. The area of reverse flow, the location (and the value) of peak compares well the experimental and LES results of Lyn *et al.* [29] and Voke [31] respectively (likewise, both for higher Reynolds number flows). Overall, the analysis above indicates that the grid size used the present study is sufficient to allow the LES to accurately reproduce the essential features of the flow in both the shear layers on the sides of the cylinder and within the wake region.

2.3.3 Phase-averaged structures:

The phase-averaged values of the spanwise vorticity and velocity vectors are plotted in Figure 2.9 for four different phases. As shown, the recirculation zone and shedding of vortical structures is well captured. In order to identify the centers of the Kármán vortices, a smoothing filter is used in thesevisualizations. The velocity vectors clearly show the recirculation zone in the near-wake, including the region of reverse flow immediately downstream of the cylinder. Comparison of the four phases illustrates the process of vortex shedding; typically, as one vortex structure forms and grows, the other contracts and is displaced downstream. Figure 2.9 (a) plots the first phase ($\pi/2$ or $T/4$) which represents the case when the clockwise vortex reaches its maximum. Moving to the next phase (π), the

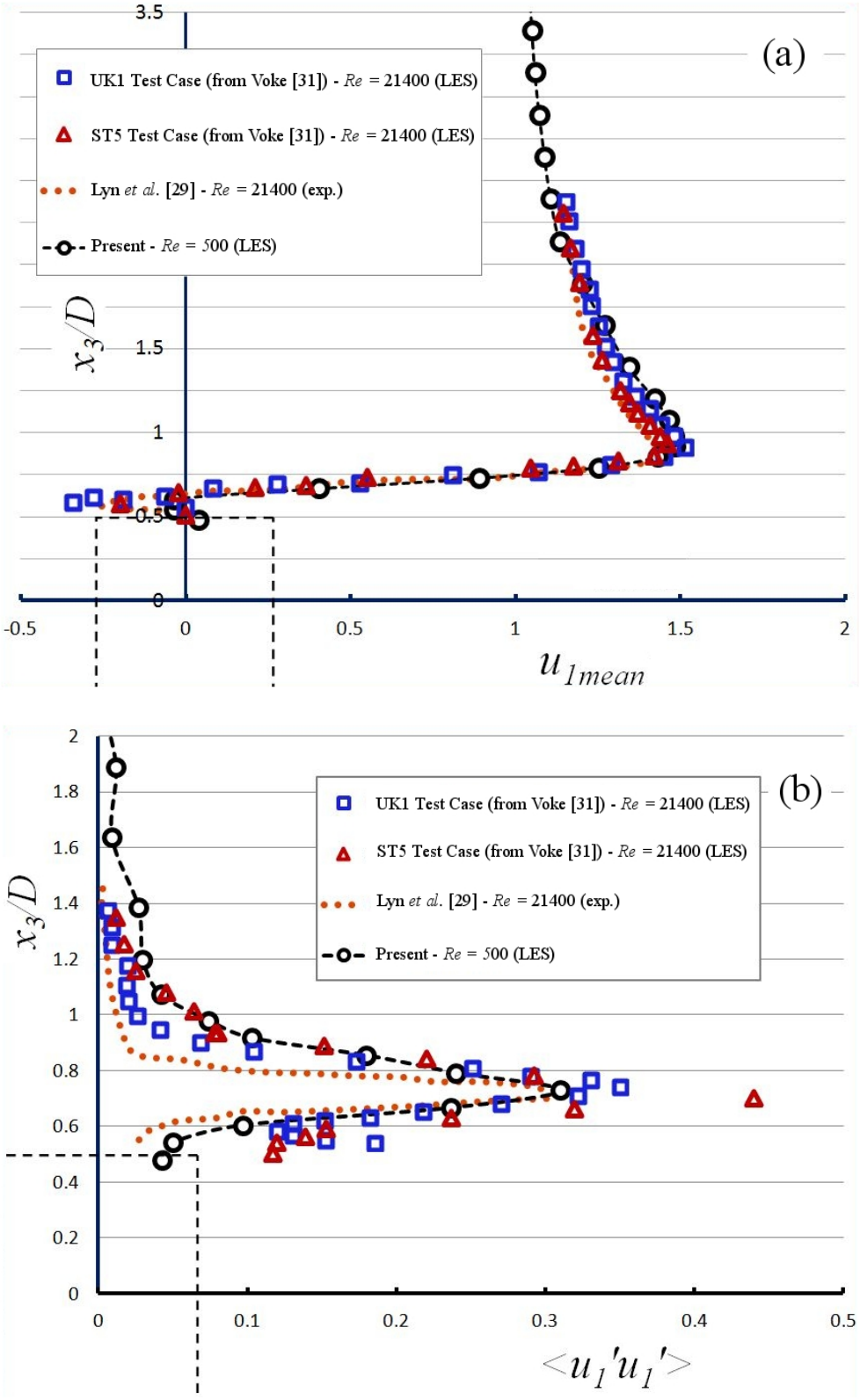

Figure 2.8: Profiles of the (a) mean streamwise velocity, and (b) fluctuations $\langle u_1' u_1' \rangle$ along a transverse section located at the midpoint of the top face of the cylinder.

counter-clockwise vortex evolves, whilst the clockwise vortex is diminished, until a relatively symmetric pattern forms with respect to the centerline, as shown in Figure 2.9 (b). Figures 2.9 (c) and 2.9 (d) show the $3\pi/2$ and 2π phases, respectively, which represent the counterparts to the first and second phase.

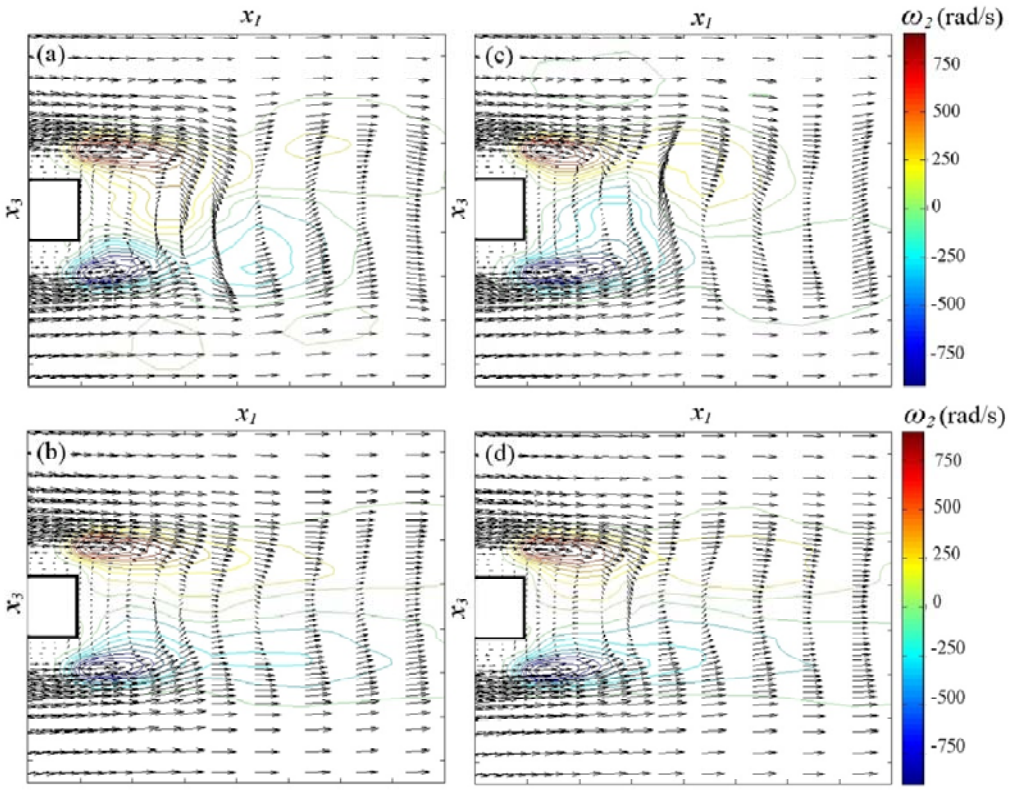

Figure 2.9: Phase-average iso-vorticity contours and vector plots for a) 1/4, b) 1/2, c) 3/4 and d) 1 shedding period *T*

Figure 2.10 shows the phase-averaged transverse velocity distribution along the centerline at two select phases ($T/4$ and $3T/4$). For both phases the first positive/negative peak value occurs at $x_1/D \approx 2.2$ which agrees with the fluctuating velocity distribution shown in Figure 2.7. In the near-wake region, the curve for $3T/4$ is almost exactly anti-symmetric to the curve for $T/4$ plot. However, this anti-symmetry becomes less precise as we move further downstream, i.e. more than 4*D* downstream of the bluff body. This incongruity could be caused due to an insufficient number of samples in each bin. Another consequence of this issue can be visualized in other phases as well; for the $T/2$ and T phases,

both iso-contour and vector plots show deviations from a strict anti-symmetric pattern (a qualitative analysis of Figures 2.9 (b) and 2.9 (d)).

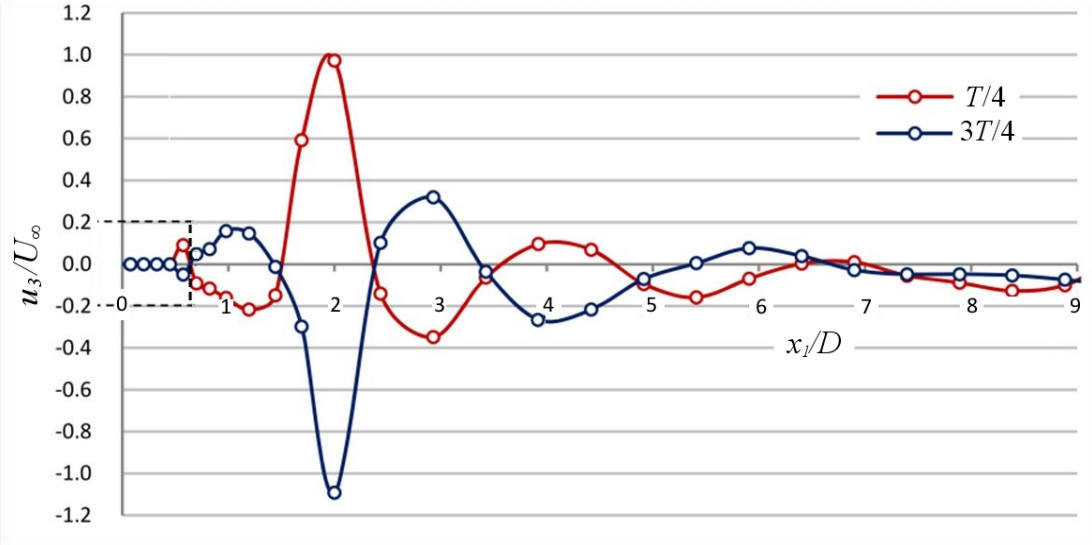

Figure 2.10: Phase-averaged transverse velocity component along the centerline for two phases

To further illustrate the behavior of the phase-averaged velocity field, iso-vorticity contours and vector plots of the time-averaged flow are presented in Figure 2.11. Unlike the phase-averaged profiles ($T/2$ and T), the time-averaged profile exhibits a perfectly symmetric vorticity and velocity distribution as shown in Figure 2.11(a). Figures 2.11(b) and 2.11(c) compare transverse profiles of the streamwise and transverse velocity components for phase- and time-averaged quantities at the same location in the wake. As shown, within the shear layer zone there is a clear difference in the profiles, which is in accordance with previous phase-averaged studies of similar cylinder flows, e.g. Lyn and Rodi [17] and Persillon and Braza [20].

In addition to increasing the number of samples in each bin, the phase-averaged results would be improved by reducing the Δt between snapshots, which would increase the number of intervals in each shedding period. The current set-up results in a deviation of up to $\pm 7°$ in the samples in the same phase bin, which would correspond to about $0.15D$ in spatial distance, which is quite substantial for a phase-average study.

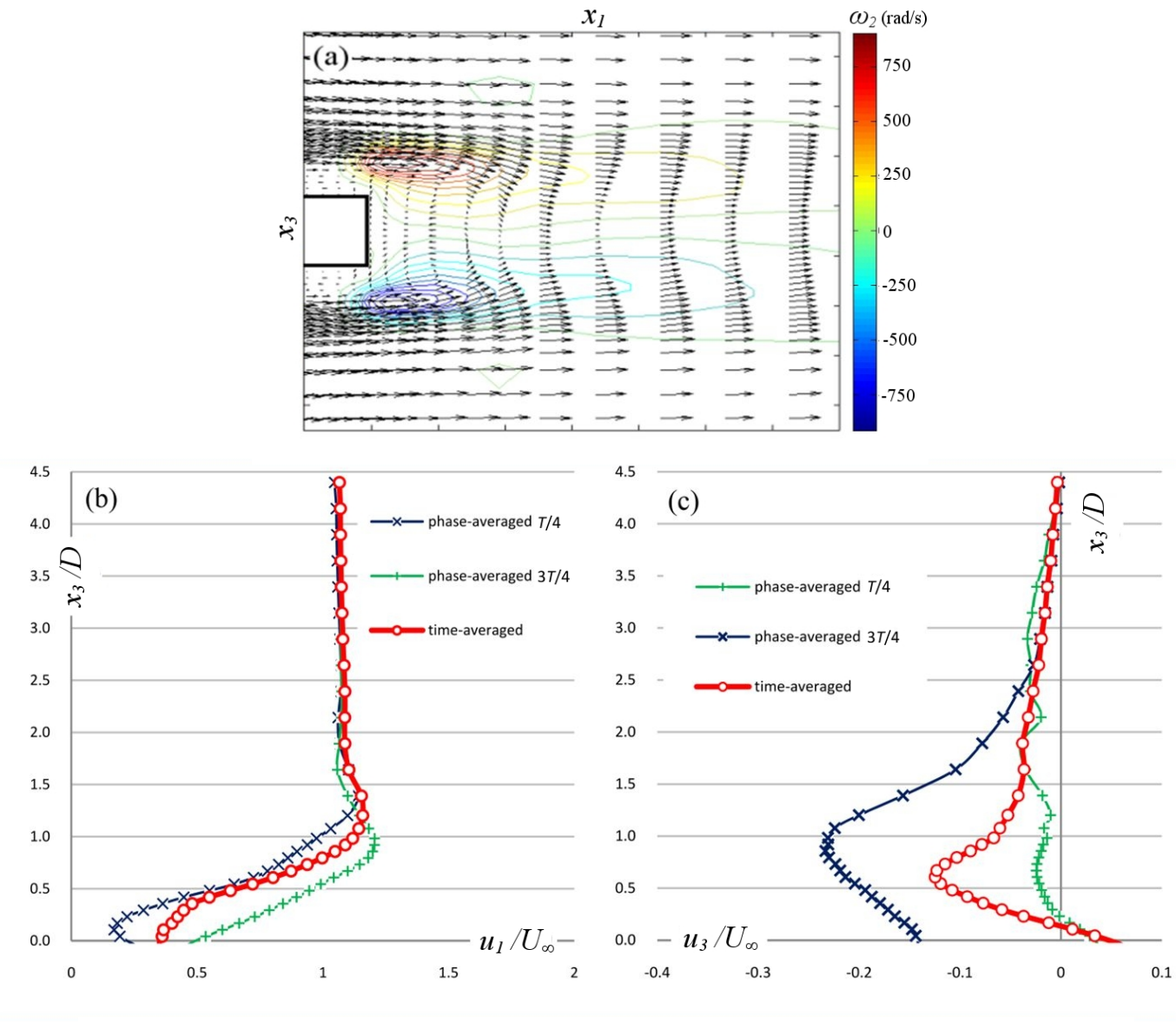

Figure 2.11: (a) Vorticity contours and vector plot of the time-averaged flow in the wake, comparison of the phase-averaged (b) streamwise and (c) transverse velocity component profiles to the time-average

2.4 POD Analysis

2.4.1 Energy spectrum:

Prior to investigating the large-scale energy-containing structures of the flow, the mean flow pattern is obtained in terms of the ensemble average of the snapshots. For the case of this work, the mean flow

was obtained by averaging 1200 instantaneous velocity fields, which were collected during 26 vortex shedding periods each 0.16 seconds in duration. A comparison of the ensemble average versus instantaneous snapshot of the velocity field has been shown in Figure 2.4. The symmetric shape of the wake for the infinite cylinder indicates that the ensemble size used was sufficient to yield a realistic mean field.

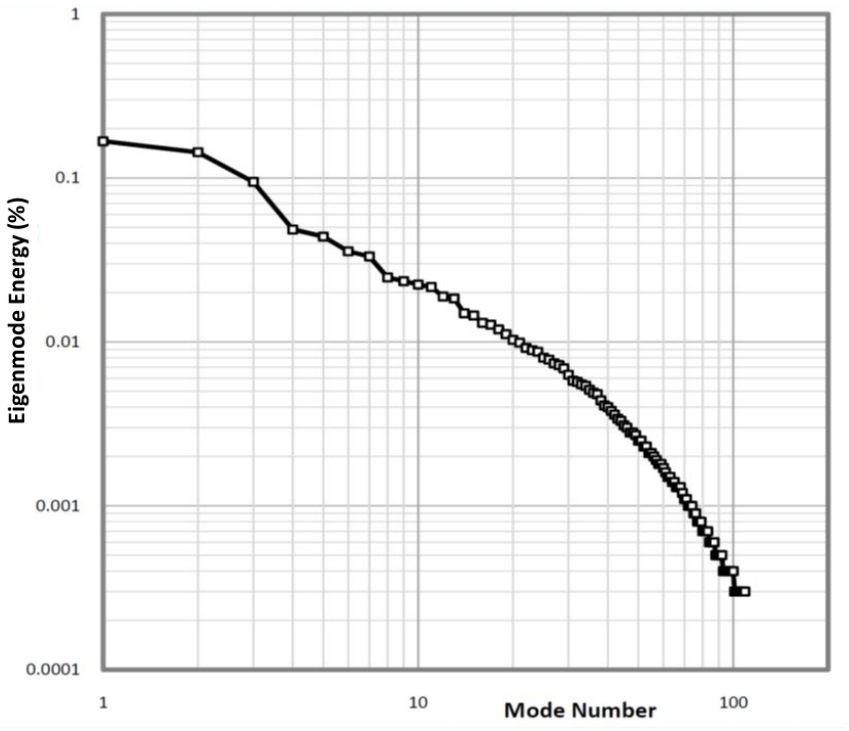

Figure 2.12: Convergence of POD eigenvalues

In order to test the convergence of the POD eigenvalues and identify the most energetic modes, the contribution of the kinetic energy contained in each mode is plotted on a logarithmic scale in Figure 2.12. The lower-order modes correspond to the larger scales which represent the more energetic features of the flow. The higher eigenmodes have smaller eigenvalues and contain information on the smaller-scale flow features. There is a continuous and clear decline in the energy spectra, which means that the POD effectively identifies the energetic modes. As shown in Figure 2.12, more than 90% of the total kinetic energy of the velocity perturbations is captured by only the first 35 modes (1200 modes in total). A

significant characteristic of the energy spectra shown in Figure 2.12 is that some of the eigenvalues can be grouped by pairs. This is in agreement with other studies of the POD analysis of a two-dimensional square cylinder, e.g., Ma and Karniadakis [5], Bergmann et al. [15], Hay et al. [19]. Hay et al. [19] presumed that: "*This property comes from the temporal periodicity of the flow, which here is preserved through any parameter change, and makes the temporal eigenfunctions Fourier modes*." Another physical interpretation of this characteristic is given by Ma and Karniadakis [5]: "*The modes form pairs due to the closeness of the vortex street to a travelling wave, similarly to the two-dimensional flow studied in Deane et al. (1991)* ([14]). *This is also reflected in the eigenmodes of each pair, which are phase-shifted with respect to each other*".

2.4.2 Energetic velocity modes:

Figure 2.13 provides a qualitative picture of the first three spatial POD modes in the center-plane. Using contour-lines of the streamwise and normal velocity components, the large-scale features of the first three dominant eigenmodes are visualized. Blue and red contours refer to negative and positive values of the velocity, respectively. Figures 2.13(a) through (c) portray the streamline flow pattern for the first three modes. To put emphasis on the dominant flow topology, streamlines are only shown for the areas with larger velocity vectors. As shown, for both modes the pattern slightly dissipates downstream.

The first pair has a harmonic travelling-wave character, in which the second mode looks like a phase-shifted pattern of the first mode. Hay et al. [19] made a similar observation: *"The POD modes are almost even or odd functions in x_2 as it is the case for the symmetric configuration*". For the third mode, the flow character is no longer harmonic, but an asymmetric topology can be seen in the streamline pattern (and likewise for the lateral velocity). In agreement with other POD wake studies (e.g. van Oudheusden *et al.* [6]), the first two modes are associated with periodic Kármán vortex shedding and can be combined as shown in Figure 2.15 to reproduce the shedding motions.

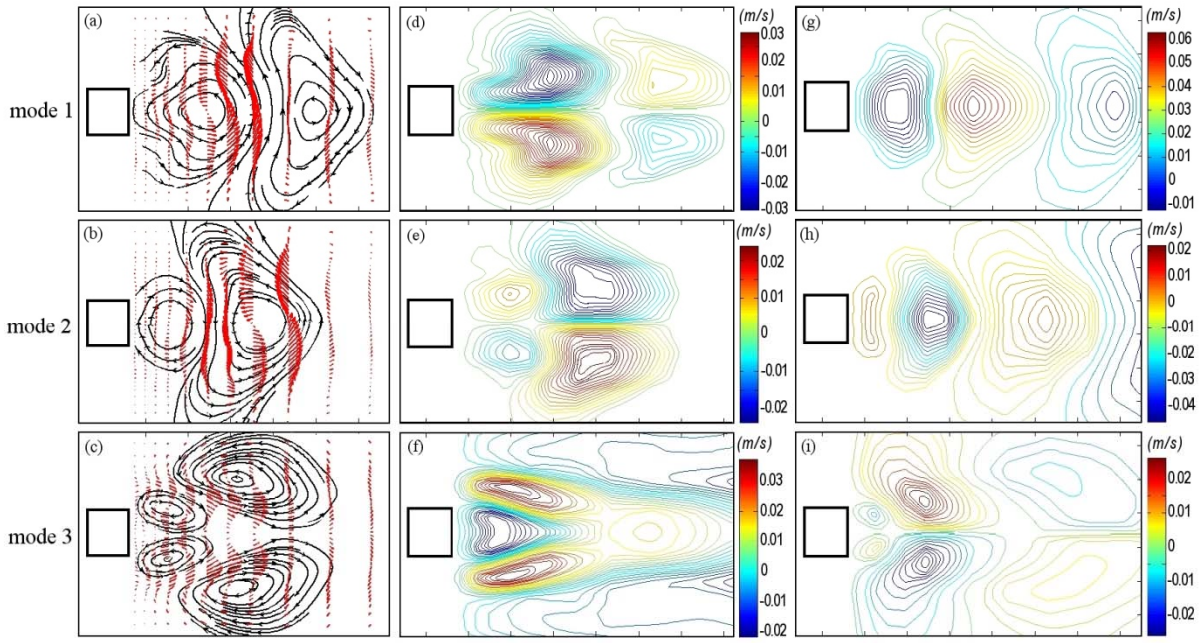

Figure 2.13: Spatial structures of the first 3 eigenmodes: (a) to (c): streamline patterns; (d) to (f): streamwise velocity component; and (g) to (i): transverse velocity component (different contour ranges and levels are used in each of the subfigures)

Another significant characteristic of the first pair of spatial modes is that the large-scale structures are concentrated in the near-wake region, whereas for the third mode, relatively large structures are distributed throughout the wake region; this is even more noticeable for the streamwise velocity component. Therefore, one can conclude that the third eigenmode is of a different nature compared with the first pair. Similar patterns were obtained for the first three modes for the case of a circular cylinder in previous studies, e.g. (Bergmann *et al.* [15], Borggaard *et al.* [21], Buffoni *et al.* [7], Hay *et al.*[19], Ma and Karniadakis [5], Perrin *et al.* [23], Persillon *et al.* [20]) .

To further develop a physical interpretation of the energetic structures and better study the characteristics of and relations between POD eigenmodes, the temporal coefficients, $a_n(t)$, are examined; recall that they signify the amplitude of the eigenmodes for a given snapshot in time. The time variation of the first five temporal coefficients for one shedding cycle is plotted in Figure 2.14(a). As shown, a_1 and a_2 are approximately sinusoidal with almost equal magnitude, but with a phase shift of $\pi/2$. This characteristic can be illustrated further by cross plotting the two-dimensional projection of the

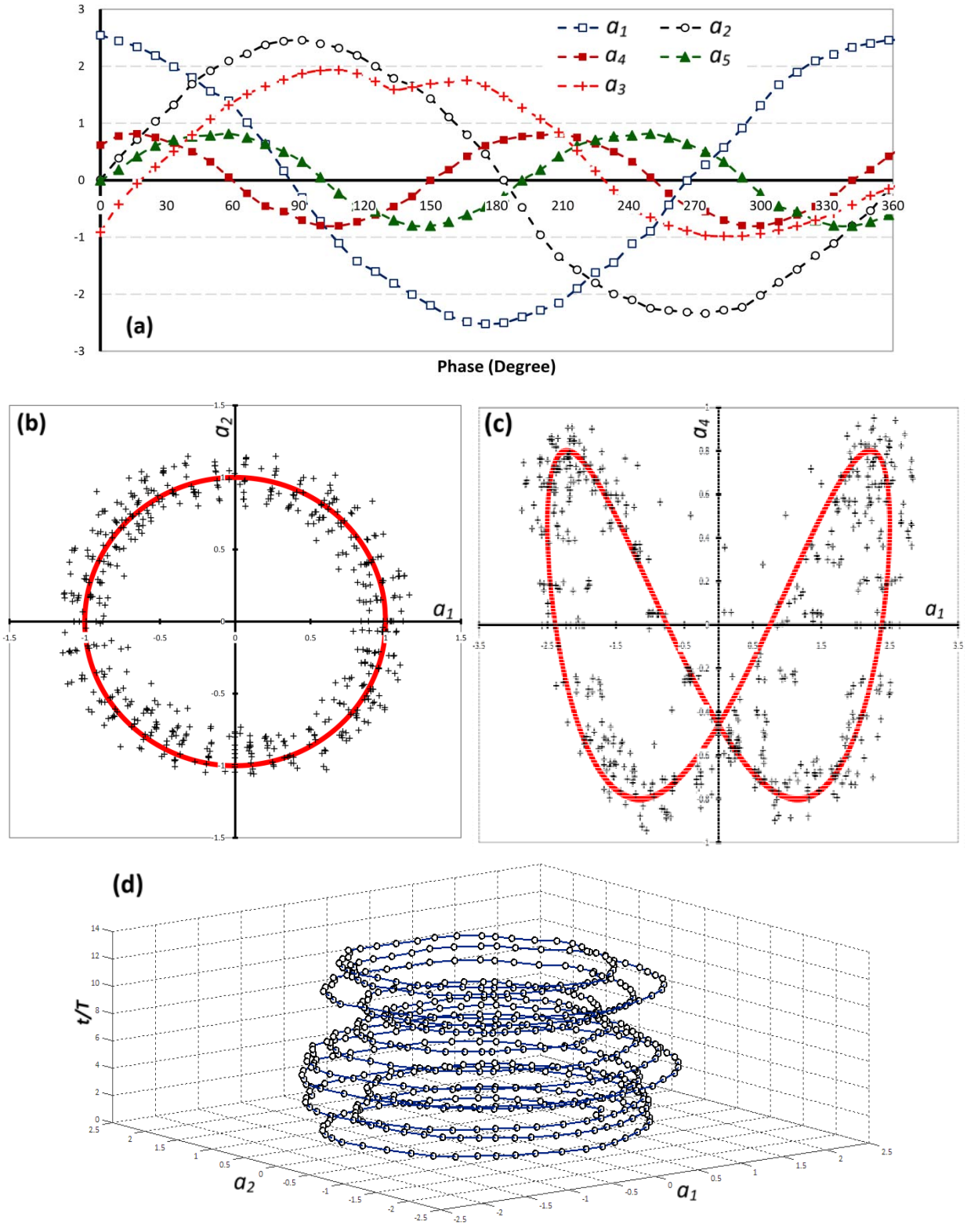

Figure 2.14: (a) Temporal behavior of the first five eigenmodes over one shedding period, (b) cross plot of normalized coefficients [a_1-a_2], (c) cross plot of normalized coefficients [a_1-a_4] and (d) time evolution of coefficients [a_1-a_2] over 13 shedding periods.

phase portrait for one shedding period for normalized pairs of coefficient; the cross plots for $[a_1 - a_2]$ and $[a_1 - a_4]$ are given in Figures 2.14 (b) and (c), respectively. The data points are clearly scattered around the theoretical curves (theoretical curves are plotted based on the predicted phase difference). A three-dimensional portrait of the first two modes evolving in time also validates this characteristic, as shown in Figure 2.14 (d). The curves are in a reasonable agreement with previous studies, e.g. (Borggaard *et al.* [21], Gillies *et al.* [25], Ma and Karniadakis [5], van Oudheusden *et al.* [6], Perrin *et al.* [23]). Another key characteristic of the $[a_1 - a_2]$ pair is that they are both fluctuating with the same frequency equal to the Strouhal frequency as calculated in Section 2.2. This is further evidence that the first two modes are associated with the same coherent structure, i.e. Kármán vortex shedding. As mentioned earlier, one can reproduce the main structures of the Kármán vortex shedding process at any phase, by combining only the first two modes, which reflects the notion of Reduced Order Modeling (ROM), another advantage of using POD.

Both Figures 2.12 and 2.14 indicate that modes 4 and 5 also make pairs, where mode 5 is a phase shift of mode 4. The amplitude of the second pair is notably smaller than the first pair, but the frequency is significantly higher. Physically the second mode pair, i.e. modes 4 and 5, could be associated with the start of evolving instabilities. Their flow topologies are quiet complex and therefore difficult to analyze qualitatively as was done for the first pair.

Between the two pairs sits mode 3, which appears to be a stand-alone mode. It is clear that this mode does not have a periodic variation and therefore is a different type than the other modes. Figures 2.12, 2.13 and 2.14 confirm this scenario. This single mode with substantial energy content could be attributed to the adjustments in the free stream flow due to the existence of the bluff body. Based on Figure 2.12, one would expect to see some harmonic behavior for the next few pairs, e.g. modes 6 and 7 appear to be a pair. The higher modes, however, are more difficult to analyze and to infer a physical interpretation for their behavior.

2.4.3 Reconstruction of turbulent flow:

After obtaining the POD spatial modes ($\phi_k(x_i)$) and corresponding temporal coefficients ($a_k(t)$), reconstruction of instantaneous flow field (at each snapshot time) can be performed by choosing a finite

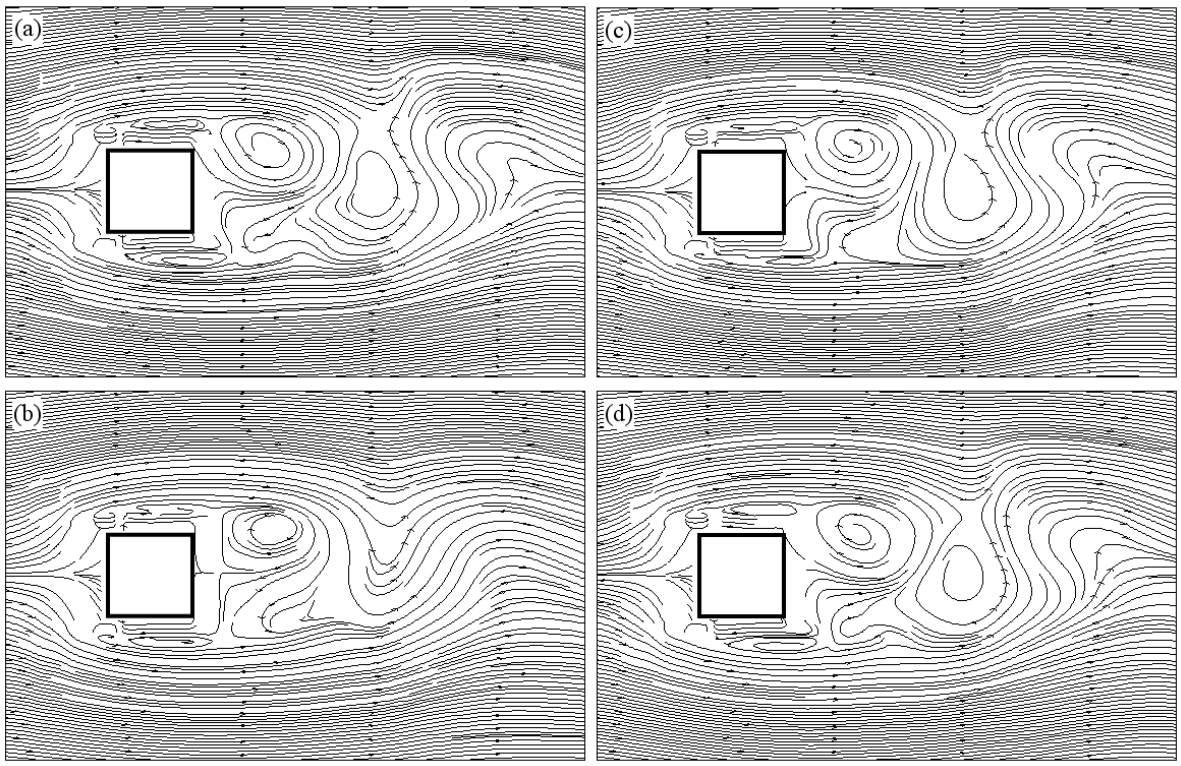

Figure 2.15: (a) Streamlines for instantaneous flow field and the reconstructed flow field for: (b) M_o = 2 , (c) M_o = 24 , and (d) M_o = 60.

number of dominant modes. As explained, POD modes give an optimal decomposition for a turbulent flow field in the sense that much of the flow topology can be captured by using only a few modes. Figure 2.15 (a) shows the streamline pattern of a random snapshot k of the original flow field. The global flow field can be approximately by a linear combination of the mean flow and a finite number of spatial modes, i.e.: $\phi_0(x_i) + \sum_{m=1}^{M_0} a_m(t_k)\phi_m(x_i)$ in which M_0 denotes the number of modes considered. In Figure 2.15 (b), the reconstructed flow field based on the first two dominant modes ($M_0 = 2$) is shown. The first two modes capture about 32% of the total perturbation kinetic energy of the flow. As is shown, the formation of the main vortex structure is well reproduced by the first two dominant modes. In order to

reconstruct the evolution of additional vortices, a reconstruction based on additional spatial modes is carried out. Figures 2.15 (c) and 2.15 (d) show the reconstructed field based on the first 24 and 60 POD modes, respectively. As shown, the last reconstruction is similar enough to the selected snapshot for one to conclude that 60 orthonormal bases are sufficient to accurately reconstruct the flow field, even though a total of 1200 modes exists. In other words, the 60-mode model represents a low-order description of the wake flow with an error of less than 1% in terms of the kinetic energy.

2.4.4 Streamwise sampling plane:

Performing POD on a spanwise sampling plane has been performed, partly for the sake of verifying POD algorithm, where qualitative results for this sampling plane are available from previous studies. The next step is to apply POD to snapshots collected on a streamwise sampling plane. The sampling plane is located about $2D$ behind the rear face of the cylinder. Nearly 400 snapshots were collected to perform this preliminary POD analysis, over a time duration of 9 convective units (D/U_∞). Similar to the first sampling plane, the time step for the simulation was set to $0.001D/U_\infty$ and snapshots were taken every 20th time step.

Figure 2.16 shows the energy decay rate based on 99% total energy filter, which means 99% of total kinetic energy of flow is captured by the first 76 modes, as shown. Here the ensemble averaged field (also known as mode 0) is not subtracted from the total field while doing POD, which explains why the energy contained in the first mode is significantly higher than for the next modes. To allow having number 0 on one axis, the energy spectrum is not plotted on a logarithmic scale as was done for the spanwise sampling plane. The pair-wise decay, which was observed in spanwise plane, can no longer be seen. Instead a gradual, fairly steep decline is visible on the next four modes.

The topology of the first four modes, including the mode 0 is presented in terms of lateral velocity (u_3), spanwise velocity (u_2) and velocity vectors in Figures 2.17, 2.18 and 2.19, respectively. As shown in

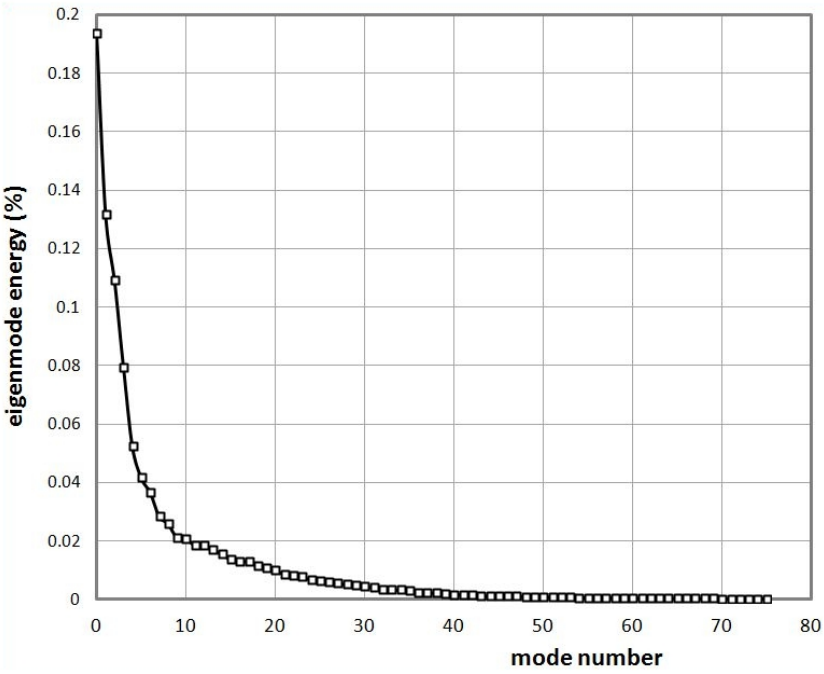

Figure 2.16: Energy spectrum for streamwise sampling pane

Figure 2.17, the ensemble averaged lateral velocity field has a nearly symmetric pattern, which represents the symmetric vortical cells of Figure 2.4. Mode 1 on the other hand, seems to have a different type of topology; an up-wash motion covers close to half of the cylinder length (red curves) and a relatively weaker down-wash motion covers the other half. These up- and down-wash motions persist for modes 2 and 3, with a difference that in mode 2, the cylinder is covered with two up-wash and two down-wash fields. In mode 3, the flow is decomposed into more, but smaller up- and down-wash regions. Mode 4 seems to be of a completely different nature than the first 3 modes; the structures are more elongated in the spanwise direction and more comparable with the ensemble averaged field, but of a significantly smaller order of magnitude, which can be concluded from the values on the color map bars. Mode 5 seems to possess a fairly similar characteristic, in which some of the structures are extended in the spanwise direction. An interesting contrast between modes 4 and 5 is in the direction of the lateral motions; in mode 4, a downward motion field stretches above the cylinder centerline while an upward motion field of the same size sits below the centerline. So, the two structures have a tendency to move towards the cylinder's centerline. Conversely for mode 5, these stretched fields have opposite signs, i.e.

the field above the centerline has an upward sign while the field below the centerline has a downward sign. In this case, the two fields have a tendency to move away from the cylinder's centerline.

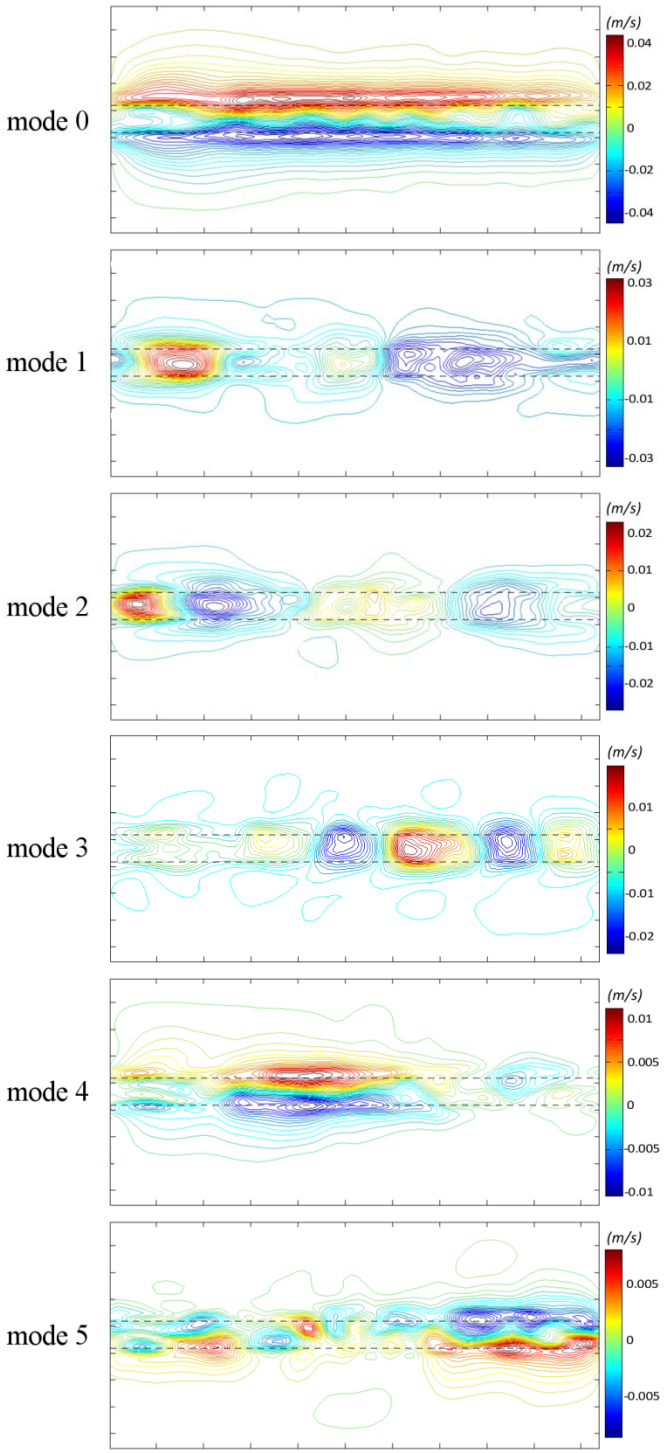

Figure 2.17: Lateral component (ϕ_{u_3}) of the first six POD eigenmodes

Another interesting difference between modes 4 and 5 is the location of the velocity peaks. In mode 4 the more energetic structures seem to be distributed towards one end of the cylinder, i.e. left end

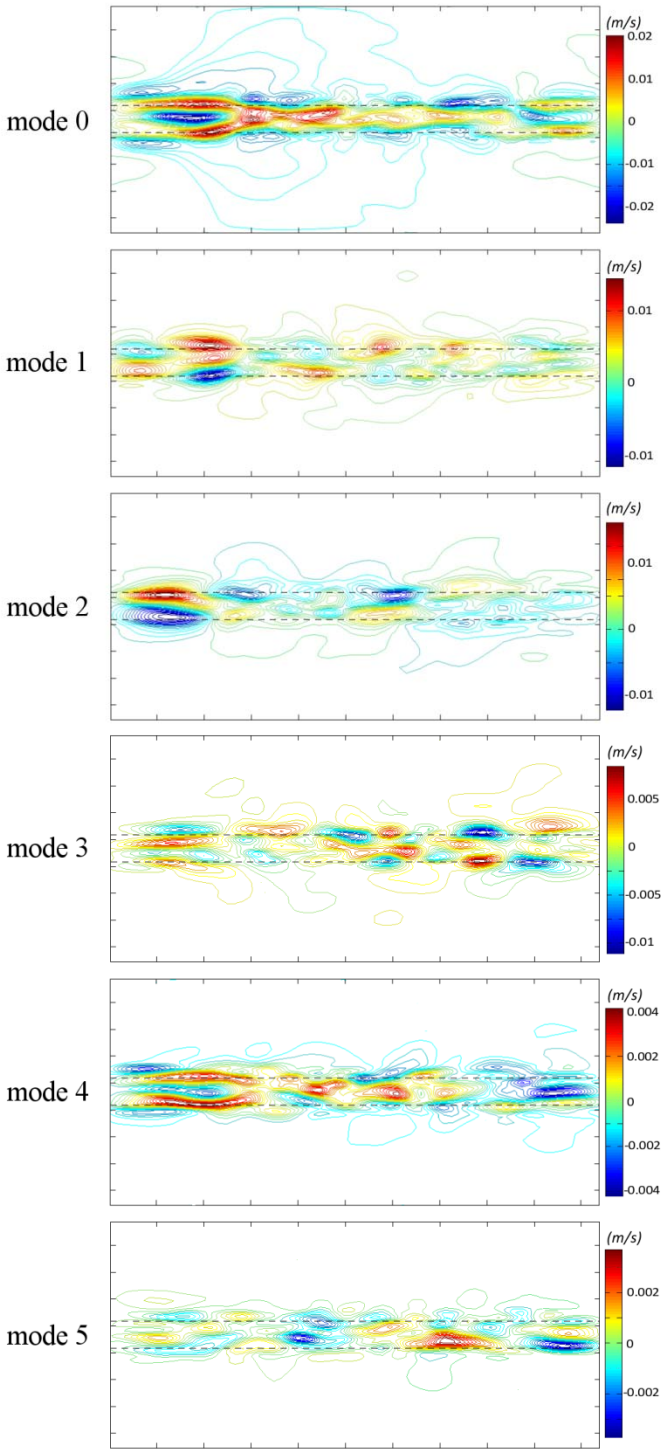

Figure 2.18: Spanwise component (ϕ_{u_2}) of the first six POD eigenmodes

as shown in the figure, whereas in mode 5, the peak region seems to be displaced towards the opposite end. Somewhat similar movement can be detected in modes 1 through 3 as well; the peak is on the left

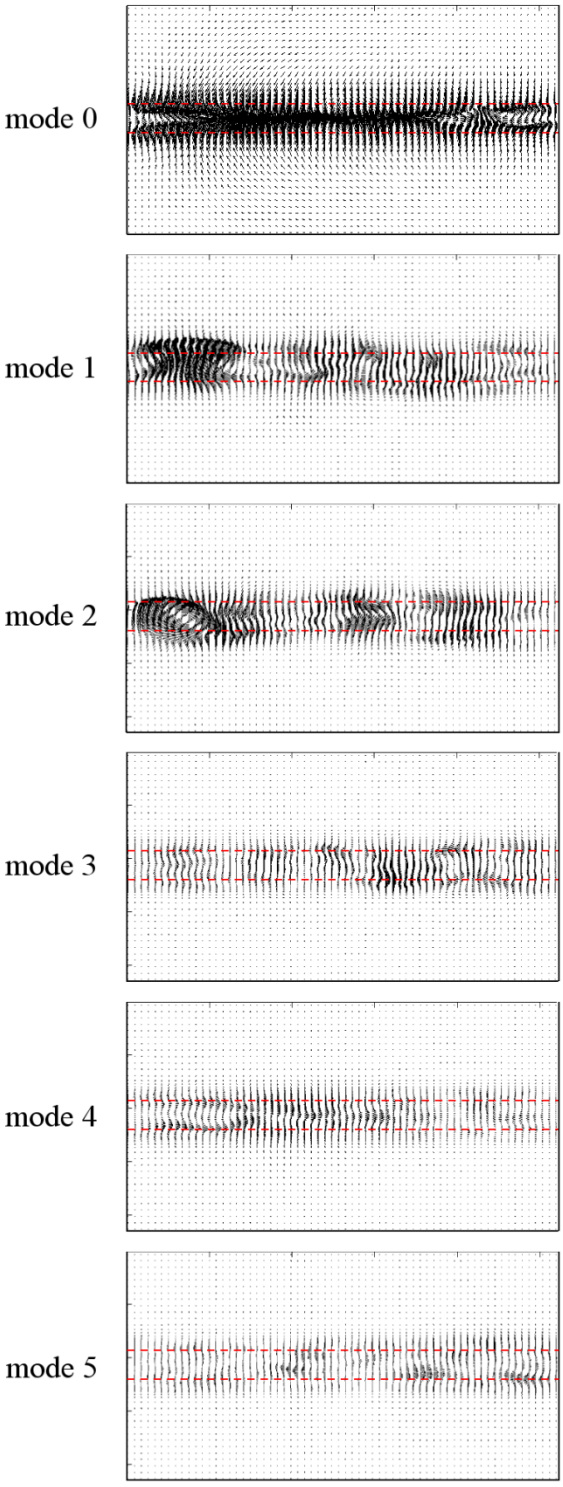

Figure 2.18: Velocity vector field of the first six POD eigenmodes

side in modes 1 and 2, while it goes towards the right side in mode 3.

Figure 2.18 demonstrates the spanwise velocity component of modes 0 through 5. Unlike the lateral velocity component, the ensemble average of the spanwise field does not have a symmetric topology. This figure also reveals that, despite the two-dimensional geometry, the turbulent wake is highly three-dimensional. A similarity between this figure and Figure 2.17 is the distribution of energetic structures; in modes 1 and 2, the energetic structures are more distributed on the left side, while in mode 3 they are moved towards the right side. Likewise between modes 4 and 5, the peak regions relocate from one side to another. Lastly, the noise on the curves in Figures 2.17 and 2.18 suggests an extended study of this sampling plane with a larger number of snapshots.

The velocity vector fields of the first six modes are shown in Figure 2.19. This figure can be used to get a sense of vortical motions in the wake as well. This figure also demonstrates three-dimensionality of the turbulent wake, generated by a simple two-dimensional geometry.

2.5 Conclusion and Outlook

In this study, the wake created behind an infinite square cylinder placed in a free stream flow has been studied. The LES method was used to predict the large-scale velocity fields, and it produced results that were consistent with other LES and DNS performed for the circular cylinder and square prism. The main objective of the paper was to investigate the dominant flow structures embedded in the global flow field with the goal of characterizing these topologies. To study the dynamics of these structures, snapshot POD was applied to two-dimensional slices of the instantaneous velocity field. It was used to provide insight as to the spatial distribution of dominant structures in the turbulent wake. Each eigenmode represents a particular flow structure embedded in the turbulent wake, and some eigenmodes can be associated as pairs. Some dominant flow structures were associated with different modes related to vortex

shedding, which was represented by the first pair, bulk flow adjustment, which was captured by the third mode and higher harmonic fluctuations which are embedded in higher order modes. The results obtained are in agreement with similar POD analysis that has been performed for the wake of a circular cylinder. Performing POD on snapshots collected on the spanwise sampling plane demonstrated three-dimensionality of the coherent structures. This also motivates further POD investigations on other sampling planes (e.g. a horizontal plane or streamwise planes on different locations). Overall, the summary results presented in the paper demonstrate the effectiveness of POD in extracting a low-dimensional description from a high-dimensional process, in this case a turbulent flow. Moreover, it was demonstrated, in a visual sense, the robustness of POD in reconstructing the structure evolutions. A companion study which considers a POD analysis of a square cylinder on a ground plane will use the infinite cylinder study presented in this paper as an important reference case.

References:

[1] J. Fröhlich and W. Rodi, "LES of the flow around a circular cylinder of finite height." *International Journal of Heat and Fluid Flow*, 25: 537-548, 2004.

[2] A. Sohankar, C. Norberg and L. Davidson, "Simulation of three-dimensional flow around a square cylinder at moderate Reynolds numbers." *Physics of Fluids*, 2: 288-306, 1999.

[3] W. Rodi, "Large-eddy simulations of the flow past bluff bodies; state of the art." *JSME International Journal*, Series B, 41(2): 361-374, 1998.

[4] A. Sohankar, L. Davidson and C. Norberg, "Large Eddy Simulation of Flow Past a Square Cylinder: Comparison of Different Subgrid Scale Models." *Journal of Fluids Engineering*, 122: 39-47, 2000.

[5] X. Ma and G.E. Karniadakis, "A low-dimensional model for simulating three-dimensional cylinder flow." *Journal of Fluid Mechanics*, 458: 181-190, 2002.

[6] B. W. Van Oudheusden, F. Scarano, N. P. Van Hinsberg and D. W. Watt, "Phase-resolved characterization of vortex shedding in the near wake of a square-section cylinder at incidence." *Experiments in Fluids,* 39: 86-98, 2005.

[7] M. Buffoni, S. Camarri, A. Iollo and M.V. Salvetti, "Low-dimensional modelling of a confined three-dimensional wake flow." *Journal of Fluid Mechanics*, 569: 141-150, 2006.

[8] R. Perrin, M. Braza, E. Cid, S. Cazin, P. Chassaing, C. Mockett, T. Reimann and F. Thiele, "Coherent and turbulent process analysis in the flow past a circular cylinder at high Reynolds number" *Journal of Fluids and Structures*, 24: 1313-1325, 2008.

[9] R. Giordano, T. Astarita and G. M. Carlomagno, *Vortex shedding in the near wake of a finite cylinder.* The 14th International Symposium on Applications of Laser Techniques to Fluid Mechanics, Lisbon, Portugal, July 7-10, 2008.

[10] O. Frederich, J. Scouten, D.M. Luchtenburg and F. Thiele, *Large-scale dynamics in the flow around a finite cylinder with ground plate.* The Sixth International Symposium on Turbulence and Shear Flow Phenomena. Seoul, Korea, June 22-24, 2009.

[11] M. Germano, U. Piomelli, P.Moin and W.H. Cabot, "A dynamic subgrid-scale eddy viscosity model." *Physics of Fluids A,* 3: 1760-1765, 1991.

[12] L. Sirovich, "Turbulence and the dynamics of coherent structures." Parts I, II and III. *Quarterly of Applied Mathematics*, 45: 561-571 and 573-590, 1987.

[13] D. K. Lilly, "A proposed modification of the Germano subgrid-scale closure method." *Physics of Fluids A,* 4: 633–635, 1992.

[14] A. E. Deane, I. G. Kevrekidis, G. E. Karniadakis and S. A. Orszag, "Low dimensional models for complex geometry flows: Application to grooved channels and circular cylinders." *Physics of Fluids A*, 3: 2337-2354, 1991.

[15] M. Bergmann, L. Cordier and J. Brancher, "Optimal rotary control of the cylinder wake using POD Reduced Order Model." *Physics of Fluids*, 17: 097101, 2005.

[16] H. Djeridi, M. Braza, R. Perrin, G. Harran, E. Cid and S. Cazin, "Near-Wake Turbulence Properties around a Circular Cylinder at High Reynolds Number." *Flow, Turbulence and Combustion*, 71: 19–34, 2003.

[17] D.A. Lyn and W. Rodi, "The flapping shear layer formed by flow separation from the forward corner of a square cylinder." *Journal of Fluid Mechanics*, 267: 353-376, 1994.

[18] J. D. Kim, B. Havel, H. Hangan and R. Martinuzzi, *Numerical and experimental investigation of the near wake dynamics for a square prism*, Fourth International Conference on Advances In Fluid Mechanics, Ghent, Belgium, May 15-17, 2002.

[19] A. Hay, J. Borggaard, I. Akhtar and D. Pelletier, "Reduced-order models for parameter dependent geometries based on shape sensitivity analysis." *Journal of Computational Physics*, 229: 1327–1352, 2010.

[20] H. Persillon and M. Braza, “Physical analysis of the transition to turbulence in the wake of a circular cylinder by three-dimensional Navier-Stokes simulation.” *Journal of Fluid Mechanics*, 365: 23-88, 1998.

[21] J. Borggaard, A. Hay and D. Pelletier, “Interval-Based Reduced-Order Models for Unsteady Fluid Flow.” *International Journal of Numerical Analysis and Modeling*, 4: 353–367, 2007.

[22] S. G. Siegel, J. Seidel, C. Fagley, D. M. Luchtenburg, K. Cohen and T. Mclaughlin, “Low-dimensional modelling of a transient cylinder wake using double proper orthogonal decomposition.” *Journal of Fluid Mechanics*, 610: 1–42, 2008.

[23] R. Perrin, M. Braza, E. Cid, S. Cazin, A. Barthet, A. Sevrain, C. Mockett and F. Thiele, “Obtaining phase averaged turbulence properties in the near wake of a circular cylinder at high Reynolds number using POD.” *Experiments in Fluids*, 43: 341–355, 2007.

[24] B. R. Noack, K. Afanasiev, M. Morzynski, G. Tamador and F. Thiele, “A hierarchy of low-dimensional models for the transient and post-transient cylinder wake.” *Journal of Fluid Mechanics*, 497: 335–363, 2003.

[25] E. A. Gillies, “Low-dimensional control of the circular cylinder wake.” *Journal of Fluid Mechanics*, 371: 157-178, 1998.

[26] I. Akhtar, J. Borggaard and A. Hay, “Shape Sensitivity Analysis in Flow Models Using a Finite-Difference Approach.” *Mathematical Problems in Engineering*, 2010: 1-23, 2010.

[27] A. K. Saha, G. Biswas and K. Muralidhar, “Three-dimensional study of flow past a square cylinder at low Reynolds numbers.” *International Journal of Heat and Fluid Flow* 24: 54–66, 2003.

[28] A. Okajima, “Strouhal numbers of rectangular cylinders” *Journal of Fluid Mechanics*, 123: 379-398, 1982.

[29] D. Lyn, S. Einav, W. Rodi and J. Park, “A laser Doppler elocimetry study of ensemble-averaged characteristics of the turbulent near wake of a square cylinder.” *Journal of Fluid Mechanics*, 304: 285-319, 1995.

[30] D. Bouris and G. Bergeles, “2D LES of vortex shedding from a square cylinder.” *Journal of Wind Engineering and Industrial Aerodynamics*, 80: 31-46, 1999.

[31] P. K. Voke, “Flow past a square cylinder: test case LES2.” *Direct and large-eddy simulation Workshop; 2nd, Direct and large-eddy simulation, ERCOFTAC Series,* Kluwer Academic, 5: 355-373, 1997.

[32] R. Mittal, “Progress on LES of flow past a circular cylinder”, *Annual Research Briefs, Center of Turbulence Research*: 233–241, Stanford University, 1996.

[33] P. Beaudan, P. Moin, “Numerical experiments on the flow past a circular cylinders at subcritical Reynolds numbers”, *Report No. TF-62, Thermosciences Division, Department of Mechanical Engineering*, Stanford University, 1994.

[34] C. Lindquist and E. D. R. Vieira, *Flow around square cylinders in several attack angles*, Proceedings of ENCIT 2010, 13th Brazilian Congress of Thermal Sciences and Engineering, Uberlandia, MG, Brazil, December 5-10, 2010.

[35] K. Shimada and T. Ishihara, “Application of a k-ε model to the prediction of aerodynamic characteristics of rectangular cross-section cylinders”, *Journal of Fluids and Structures,* 16(4): 465-485, 2002.

[36] C. W. Knisely, “Strouhal numbers of rectangular cylinders at incidence: a review and new data”, *Journal of Fluids and Structures* 4: 371-393, 1990.

Chapter 3

Effect of a Wall on the Wake Dynamics of an Infinite Square Cylinder

A similar version of this chapter has been submitted as:

> M. Samani and D. J. Bergstrom, "Effect of a Wall on the Wake Dynamics of an Infinite Square Cylinder", *10th International ERCOFTAC Symposium on Engineering Turbulence Modeling and Measurements* (under review).

The flow simulation results and the POD analysis were developed by the first author. Partial development of the POD routine formulation as well as initiating the LES code were performed by the second author.

Preamble:

The connecting link between the preparatory study (infinite cylinder in free stream) and the target point (flow over roughened surfaces) of this research is to investigate the influence of a nearby wall on turbulent wake structures. For the sake of this "connecting" study, a solid wall was implemented in proximity of the cylinder, which was studied in step 1. The effect of the wall was studied by considering different gaps between the wall and bluff body. A Reynolds number of Re = 500 (based on the free stream velocity and the cylinder side length) is set which is similar to the first study case and makes it possible to focus on the wall effect only. Ultimately the cylinder was placed on the surface to lay the groundwork for the next step, i.e. flow over a rib-roughened surface (by making a sequence of these obstacles as explained before).

The major contribution of this chapter to the overall study and main emphasis of this step is to compare the results of the current case(s) with the preparatory and the target studies and lay the groundwork for the next step.

Abstract

The present study investigates the influence of a solid wall on the wake structure of an infinite cylinder of square cross-section when it is placed in proximity to a wall. Three different cases have been studied by changing the distance between the cylinder and the bottom wall. For each case, the coherent wake structures have been identified by the use of Proper Orthogonal Decomposition (POD), and the results are compared with the case of an infinite cylinder in a free stream. A coarse-grid Large Eddy Simulation (LES) is used to generate the input data for the POD analysis. The analysis documents the coherent structures in the wake and their interaction with the energetic structures generated by the solid wall.

3.1 Introduction

Many industrial applications include flows over bluff bodies located in the vicinity of a wall, such as pipelines mounted above the ground and elevated walkways or bridges exposed to a cross-wind. In such applications, it important to understand how the presence of the wall modifies the drag and lift forces, as well as the flow pattern in the wake. Although a number of numerical and experimental works consider unconfined bluff bodies as well as flows over bluff bodies located in the centre of a channel, there are fewer studies which consider the bluff body in proximity to a wall. Furthermore, the majority of previous studies have focused on the circular cylinder; in contrast, flow over square cylinder in proximity to a wall has not been as extensively studied. In this context, knowledge of the interactions between the energetic structures created by prismatic bluff bodies and a bounding wall is far from complete.

For a square cylinder, at sufficiently high Reynolds numbers, the flow separation point is fixed by the upstream sharp corners. However, the mean wake flow pattern will change when the gap between the wall and body is sufficiently small. The mean wake pattern no longer consists of a pair of symmetric

recirculation zones. Even though the wake flow is still dominated by the periodic Kármán vortex shedding, the vortices shed from each side of the cylinder are of unequal strength. More specifically, the vortex shed closest to the wall is weakened, which then leads to an asymmetric wake structure. As the cylinder moves closer to the wall, the asymmetry increases, and eventually vortex shedding is entirely suppressed on the bottom side of the cylinder due to the wall. (e.g. Bailey *et al.* [6], Bosch *et al.* [7], Wang *et al.* [10])

A pioneering experimental study for a low Reynolds number ($Re = 170$) flow around a circular cylinder in proximity of wall was performed by Taneda [1]. Different gap ratios (g/D, where g is the gap distance and D is the cylinder diameter) were examined and documented in his work. Later, Bearman and Zdrakovich [2], continued this research for a higher Reynolds number ($Re = 45000$) and different gap ratios in the range of $0.2 \leq g/D \leq 0.4$. The thickness of the turbulent boundary layer (TBL) on the ground plane at the cylinder position was $\delta/D = 0.8$ in their work. The fluctuating drag and lift forces on the cylinder in terms of the gap ratio and the TBL thickness were studied by Taniguchi and Miyakoshi [3]. They also identified a critical gap ratio and examined the formation of vortex streets for different gaps. They concluded that "*the formation of Kármán vortex streets was abruptly interrupted when the bottom of the cylinder came in contact with the outer layer of the boundary layer developed on the wall*" [3]. Buresti and Lanciotti [4] performed the same study for a wider range of Reynolds number and gap ratios. Their results indicate that increasing the gap width leads to a rapid decrease of the mean lift coefficient, whereas the mean drag coefficient is extensively influenced by the TBL thickness. Later an experimental study by Lei *et al.* [5] showed that both the drag and lift coefficients strongly depend on the gap ratio. They also showed that at some specific gap ratios, the lift force changes direction. Bailey *et al.* [6] performed an experimental study of a square cylinder for different gap ratios and $Re = 19000$. They classified the wake flow into three distinct regimes based on the gap width: (i) if $g/D > 0.85$, then the wall has no significant effect, (ii) when $0.4 < g/D < 0.85$, the influence of the wall appears but does not have a dominant effect on the lift and drag coefficient, and (iii) when $g/D < 0.4$, vortex

shedding is suppressed due to the small gap width. This critical gap ratio was previously documented by Bosch *et al.* [7] as $g/D = 0.35 - 0.5$, Durao *et al.* [8] as $g/D = 0.35$, and later by Martinuzzi *et al.* [9] as $g/D = 0.3$ by measuring the pressure fluctuations for different gap ratios (all square cylinder cases). Price *et al.* [11] employed Particle Image Velocimetry and Hot Film Anemometry techniques to study a circular cylinder near a solid wall for $Re = 1200 - 4960$. The influence of boundary layer separation was also investigated in their work. They classified the flow into four regimes based on the gap width and boundary layer thickness. In a more recent experimental study by Wang *et al.* [10], the flow characteristics in the near-wake of a circular cylinder were investigated. They analyzed the instantaneous fields and by the use of vortex identification methods documented the evolution of the vorticity. They also found that the Strouhal number (St) and convection velocity of the shed vortex are independent of the gap ratio. In a comprehensive study by Lin *et al.* [12], these flow characteristics were studied in more detail and for a wide range of gap ratios (0.0 to 4.0). The mechanism of vortex shedding suppression was explained in detail (for circular cylinder cases) and a similarity in the streamwise velocity profile, when the periodic shedding originates, was detected in their study.

As previously mentioned, this study will also consider the limiting case when the square cylinder is located on the wall, so that the cylinder represents a single prismatic rib. An early LES simulation of a single rib in a fully developed channel flow was performed by Werner *et al.* [12]. Martinuzzi and Tropea [13] subsequently performed an experimental study for this arrangement. They studied the separation and reattachment regions and investigated the flow structures. As documented by Zdravkovich [15-16] the influence of the wall depends mainly on the following factors: the Reynolds number, the type of boundary layer (i.e. laminar or turbulent), the gap ratio (g/D) and the thickness of boundary layer (δ/D). For the present flow arrangement, the free stream velocity (U_∞), the cylinder side length (D) and dynamic viscosity of the fluid (ν) can be used to define the Reynolds number ($Re = U_\infty D/\nu$). In the current study, a Reynolds number of $Re = 500$ is adopted. The approach flow includes a turbulent boundary layer with thickness of $\delta/D = 0.2$.

In summary, the present study considers a square cylinder placed in proximity to a bounding wall. Three different gap ratios were considered: $g/D = 1.0,\ 0.5$ and 0. The last case resembles a prismatic obstacle on a ground plane and provides a reference case for flow in a rib-roughened channel. POD following the method of Sirovich [17] will be used to decompose the LES results into orthogonal eigenmodes, which will facilitate analysis of the flow structure. Results are compared to POD analysis of wake flow behind a square cylinder in proximity of a wall by Shi *et al.* [28].

3.2 Computational Details

The LES technique used in this study was verified and validated in a previous benchmark study of flow over an infinite square cylinder [18]. To formulate the governing equations, a spatial filter is applied to the incompressible Navier-Stokes (NS) and continuity equations,

$$\frac{\partial \overline{\boldsymbol{u}}_{\boldsymbol{i}}}{\partial t} + \frac{\partial\left(\overline{\boldsymbol{u}}_{\boldsymbol{i}}\overline{\boldsymbol{u}}_{\boldsymbol{j}}\right)}{\partial \boldsymbol{x}_{\boldsymbol{j}}} = -\frac{\partial p}{\partial \boldsymbol{x}_{\boldsymbol{i}}} + \frac{1}{Re}\frac{\partial^2 \overline{\boldsymbol{u}}_{\boldsymbol{i}}}{\partial \boldsymbol{x}_{\boldsymbol{j}}\partial \boldsymbol{x}_{\boldsymbol{j}}} - \frac{\partial \tau_{ij}}{\partial \boldsymbol{x}_{\boldsymbol{j}}} \tag{3.1}$$

and

$$\frac{\partial \overline{\boldsymbol{u}}_{\boldsymbol{i}}}{\partial \boldsymbol{x}_{\boldsymbol{i}}} = 0, \tag{3.2}$$

where $\overline{\boldsymbol{u}}_{\boldsymbol{i}}$ is the filtered velocity component, t is the time, p is the local pressure, ρ is the fluid density, $\boldsymbol{x}_{\boldsymbol{i}}$ is the corresponding Cartesian coordinate and τ_{ij} is the subgrid-scale stress (SGS) component. A dynamic Smagorinsky subgrid-scale model was employed to model the SGS stress following the method of Germano *et al.* [19] and Lilly [20]. The use of clipping and local volume-averaging was used to stabilize the dynamic coefficient; plane averaging was not required.

A non-uniform $64\times64\times64$ collocated grid was used to discretise the flow domain which extended $24D\times10D\times8D$ in the x_1, x_2 and x_3 directions respectively. As shown in Figure 3.1, the mesh was refined

near the square cylinder and in proximity to the wall. By applying periodic boundary conditions on the four lateral side surfaces, flow over an infinitely long prism was simulated. The flow is driven by a pressure gradient and initial perturbations were added to ensure a turbulent boundary layer state. The filtered Navier-Stokes equations were discretised utilizing a cell-centered finite-volume method and a semi-implicit second-order Crank-Nicolson scheme was used for the temporal discretisation. The discrete transport equations were solved using a two-step fractional step procedure together with a pressure correction scheme to ensure conservation of mass.

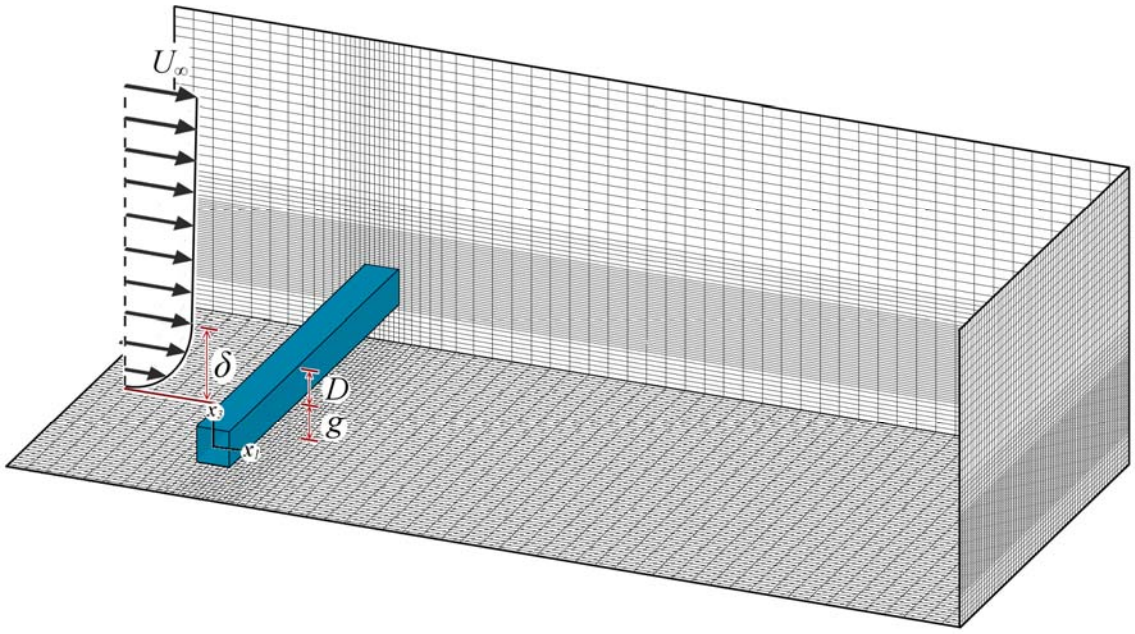

Figure 3.1: Flow configuration and layout of computational grid

The characteristic shedding frequency in the wake flow can be expressed by the non-dimensional Strouhal number given by

$$Str = \frac{f_s D}{U_\infty}, \tag{3.3}$$

where f_s denotes the shedding frequency of the vortices. The sectional drag and lift coefficients represent the non-dimensionalized drag (F_D) and lift forces (F_L) per unit length on the cylinder:

$$C_D = \frac{F_D}{\frac{1}{2}\rho U_\infty^2 D} \quad \text{where} \quad F_D = \sum_i \left(\tau_{top} + \tau_{bottom}\right)_i dx_{1_i} + \sum_j \left(P_{left} - P_{right}\right)_j dx_{3_j} \tag{3.4}$$

and

$$C_L = \frac{F_L}{\frac{1}{2}\rho U_\infty^2 D} \quad \text{where} \quad F_L = \sum_i \left(\tau_{left} + \tau_{right}\right)_i dx_{3_i} + \sum_j \left(P_{bottom} - P_{top}\right)_j dx_{1_j} \tag{3.5}$$

where ρ is the density and τ and P represent the wall shear stress and pressure, respectively. Both of these contributions to the forces act periodically on the bluff body with a frequency relevant to f_s .

Turbulent structures are complex and highly time dependent. POD is a powerful tool to extract an orthogonal set of spatial eigenmodes and then derive optimally correlated structures or the so called coherent structures by combining these energetic eigenmodes. The first step is to collect the discrete, instantaneous fields, known as snapshots, from the flow on the sampling planes. Then, an autocorrelation matrix is generated from the collected snapshots. For example, if one chose a sampling plane perpendicular to the cylinder axis ($\Omega = [x_1 - x_3]$ plane), then the autocorrelation matrix would be,

$$C(t,t') = \frac{1}{M}\int_\Omega \left[u_i'(x_1,x_3,t)u_i'(x_1,x_3,t')\right] dx_1 dx_3, \tag{3.6}$$

in which M is the total number of snapshots and $u_i'(x_1,x_3,t)$ represents the fluctuating velocity field which can be obtained by subtracting the mean field from the instantaneous. As shown, C is a two-point correlation-in-time matrix, between snapshots taken at times t and t'. An eigenvalue problem can be formulated based on the correlation matrix:

$$\int C(t,t')a_n(t')dt' = \lambda_n a_n(t). \tag{3.7}$$

Solution of this eigenvalue problem gives a series of eigenvalues (λ_n) and eigenvectors ($a_n(t)$). From the eigenvalues, one can measure the fraction of turbulent kinetic energy (TKE) contained in each mode

and accordingly collect energetic modes. Looking at the λ_n trend, it can be noticed that the convergence of energy is very fast; in fact, it convergence is faster than any other linear representation. That means, the first few modes give the main contribution to TKE and therefore can be used to reproduce the flow field, which is the spirit of using POD. The eigenvectors $(a_n(t))$ can be projected onto the velocity field to produce the eigenmode number n as

$$\phi_n(x_1, x_3) = \sum_{k=1}^{K} a_n(t_k) u_i'(x_1, x_3, t_k). \tag{3.8}$$

At the end, the discrete instantaneous snapshots can be reconstructed by using a limited number of empirical eigenmodes (M_0) in the following series:

$$u(x_1, x_3, t_n) = \sum_{m=1}^{M_0} a_m(t_n) \phi_m(x_1, x_3) \tag{3.9}$$

The database for POD analysis originates from the LES output on different sampling planes. Nearly 1100 snapshots were collected over 24 vortex shedding cycles (for the cases with vortex shedding in the wake; for other cases the same amount of snapshots over the same time frame was collected). That makes about $\Delta t = 3 \times 10^{-3}$ seconds (or 7.5°) spacing between the snapshots.

3.3 Selected Results and Discussion

3.3.1 Flow simulation results:

As mentioned previously, the numerical methodology used to simulate the flow was validated in an earlier benchmark study [18] of an infinite cylinder in a free stream. However, as a result of the nearby wall, some characteristic features of the present flow differ from the benchmark study. The deviation of the aerodynamic forces acting on the cylinder, especially the lift force, is of practical importance in

engineering applications. For the no-wall case ($g/D = \infty$), the lift force has a periodic profile with an average value of zero. However, with the presence of a nearby wall, the average value of the lift coefficient, $\overline{C_L}$, moves slightly away from zero, while the frequency of the oscillations remains the same.

Figure 3.2 displays the power spectrum obtained by performing a Fast Fourier Transform (FFT) of the temporal variation of the lift coefficient. As shown, the dominant peak is stronger for larger gaps. The magnitude of the peak reduces as the cylinder approaches the wall and at some point there is no longer a

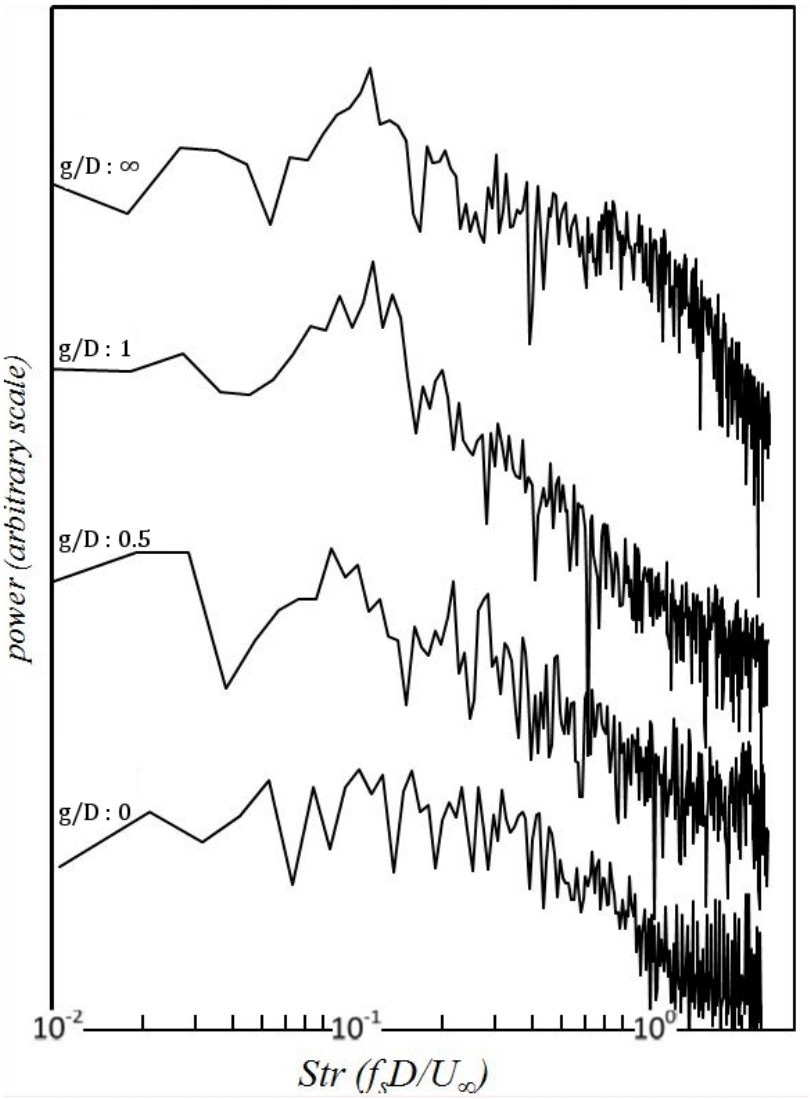

Figure 3.2: power spectra of lift forces for different gap heights

single dominant peak in the spectrum. This indicates that the bottom vortical cell is completely suppressed by the wall. Based on Figure 3.2, this occurs somewhere in the range $0 < g/D < 0.5$, which is in accordance with previous studies, e.g. [6], [7] and [8].

Another conclusion which can be drawn from Figure 3.2 is that the shedding frequency (and consequently the Strouhal number) remains unchanged by the presence of the wall. This is consistent with the observation by Wang *et al.* [10] that the Strouhal number is independent of gap ratio as mentioned. On the other hand, the amplitude of the oscillations is dramatically affected by the presence of the wall.

For all three values of the gap ratio, the shear and pressure forces on the cylinder in the streamwise direction create a drag force. In fact, the drag force is created by the pressure difference on the front and rear sides of the cylinder, and also from the shear stresses acting on the sides; the blockage created by the cylinder causes a favorable pressure gradient that contributes to the net drag force. The mean drag ($\overline{C_D}$) and lift ($\overline{C_L}$) coefficients for four different values of the gap ratio are shown in Figure 3.3. The drag coefficient increases as the gap ratio is increases, while the lift coefficient decreases. This trend is in accordance with experimental study by Bosch *et al.* [7].

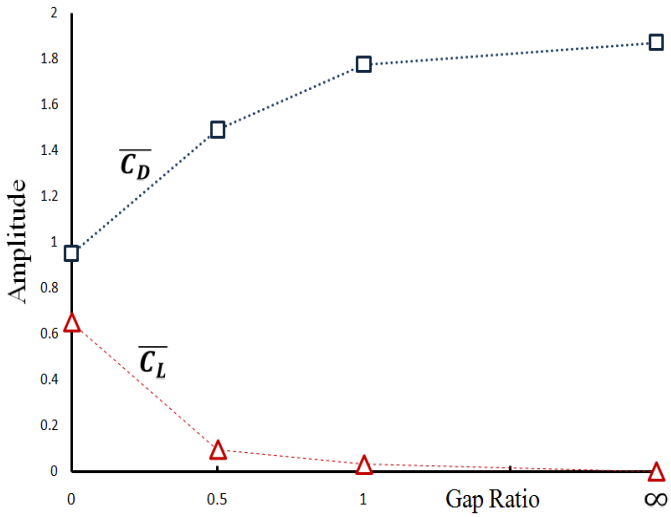

Figure 3.3: The variation of the mean drag and lift coefficients with gap ratio

			$\overline{C_D}$				$\lvert\overline{C_L}\rvert$			
	Approach	*Re*	$\frac{g}{D}=0$	$\frac{g}{D}=0.5$	$\frac{g}{D}=1$	$\frac{g}{D}=\infty$	$\frac{g}{D}=0$	$\frac{g}{D}=0.5$	$\frac{g}{D}=1$	$\frac{g}{D}=\infty$
Mahir [30]	numerical	250	-	1.59	1.78	-	-	-	-	-
Lei *et al.* [5]	experimental	13,100	-	1.29	1.41	-	-	-	-	-
Bhattacharyya *et al.* [24]	numerical	500	1.9	2.9	-	2	-	0.2	-	-
Kumaran *et al.* [22]	numerical	500	-	2.9	3.4	1.91	-	0.1	-0.003	0.003
Bhattacharyya *et al.* [31]	numerical	200	-	2.8	2.95	-	-	0.4	0.3	-
Nishino [32]	experimental	40,000	-	1.24	1.31	-	-	0.05	0.01	-
Roshko *et al.* [33]	experimental	20,000	0.8	1.12	1.24	-	0.59	0.09	0.03	-
Hiwada *et al.* [34]	experimental	20,000	0.77	1.20	1.27	-	-	-	-	-
Dutta *et al.* [35]	experimental	420	-	-	-	2.03	-	-	-	-
Davis *et al.* [36]	experimental & numerical	470	-	-	-	1.95	-	-	-	-
Present study	numerical	500	1	1.48	1.74	1.89	0.63	0.07	0.02	0

Table 3.1: the mean drag ($\overline{C_D}$) and lift ($\overline{C_L}$) coefficients for four different values of the gap ratio; comparison to data in literature

Table 3.1 compares the mean drag and lift coefficients documented in other literature. As is shown, there are some disagreements between the existing results and measurements (e.g. $\overline{C_D}$ for $g/D = 0.5$ by [22], [24] and [31] being different from all the others), which suggest further study is needed on this flow arrangement. Nevertheless, they all follow more or less same trend as shown in Figure 3.3.

Time-averaged flow patterns are plotted and compared to the instantaneous values, in the form of streamlines overlaid on vorticity contours in Figure 3.4. For all cases, the primary separation on the

cylinder occurs at the leading edge, as imposed by the square geometry. For $g/D = 1$, a secondary separation on the bottom wall can be observed in the instantaneous field, Figure 3.4(c). Although the time-averaged streamlines do not show this secondary separation, it can be inferred from the positive

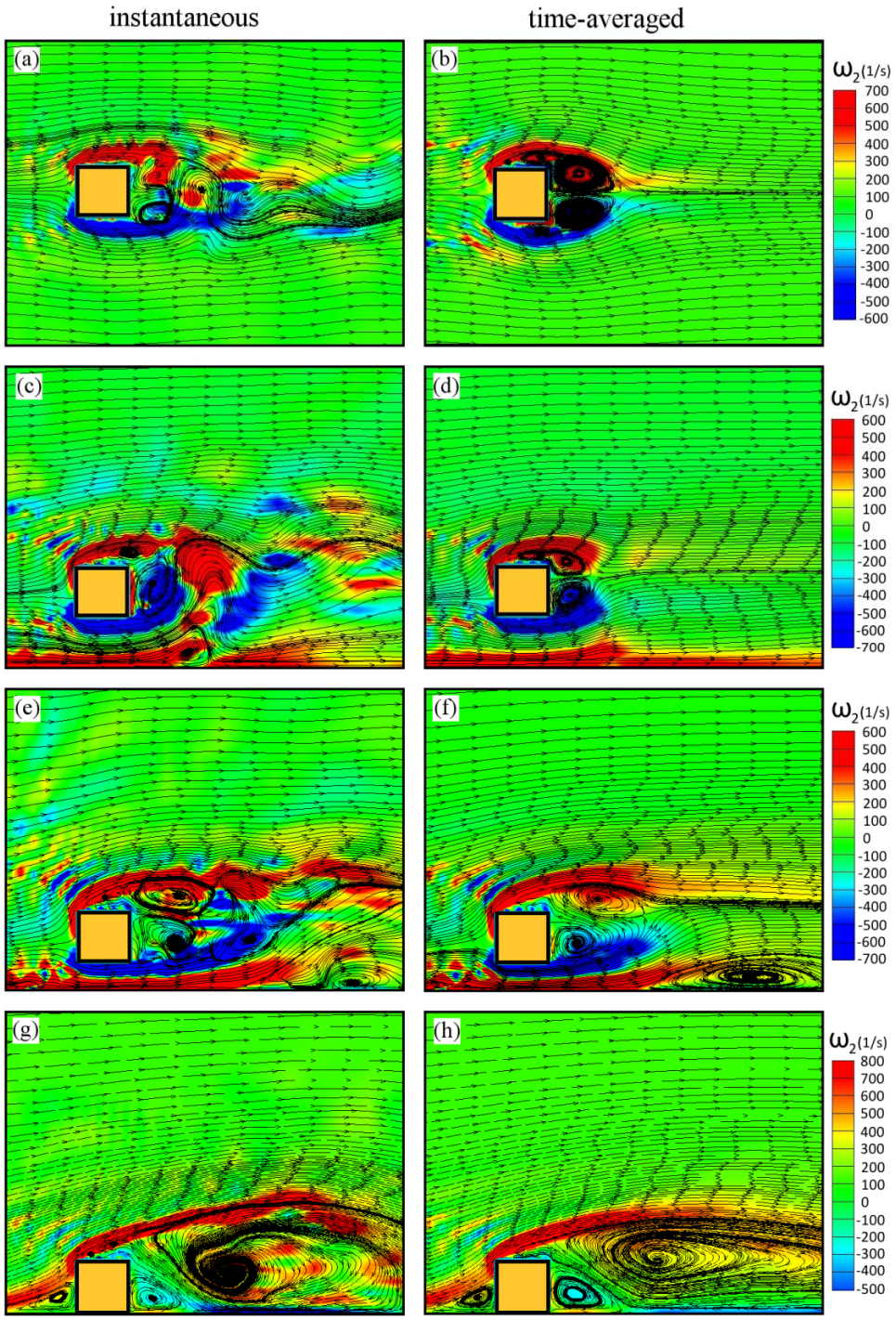

Figure 3.4: Effect of gap width on flow structure: (a) and (b): $g/D = \infty$, (c) and (d): $g/D = 1$, (e) and (f): $g/D = 0.5$, (g) and (h): $g/D = 0$

vorticity contours on the bottom wall, Figure 3.4(d). For smaller gaps, the secondary separation is more prominent and shifted downstream, Figures 3.4(e) and 3.4(f). The size of this secondary vortical cell becomes relatively large, even larger than the primary cells in the cylinder wake. In general, as the cylinder approaches the wall, the wake pattern is deflected upward, such that the top recirculation bubble in the wake is aligned almost parallel to the ground plane. Similar wake flow structures were observed in

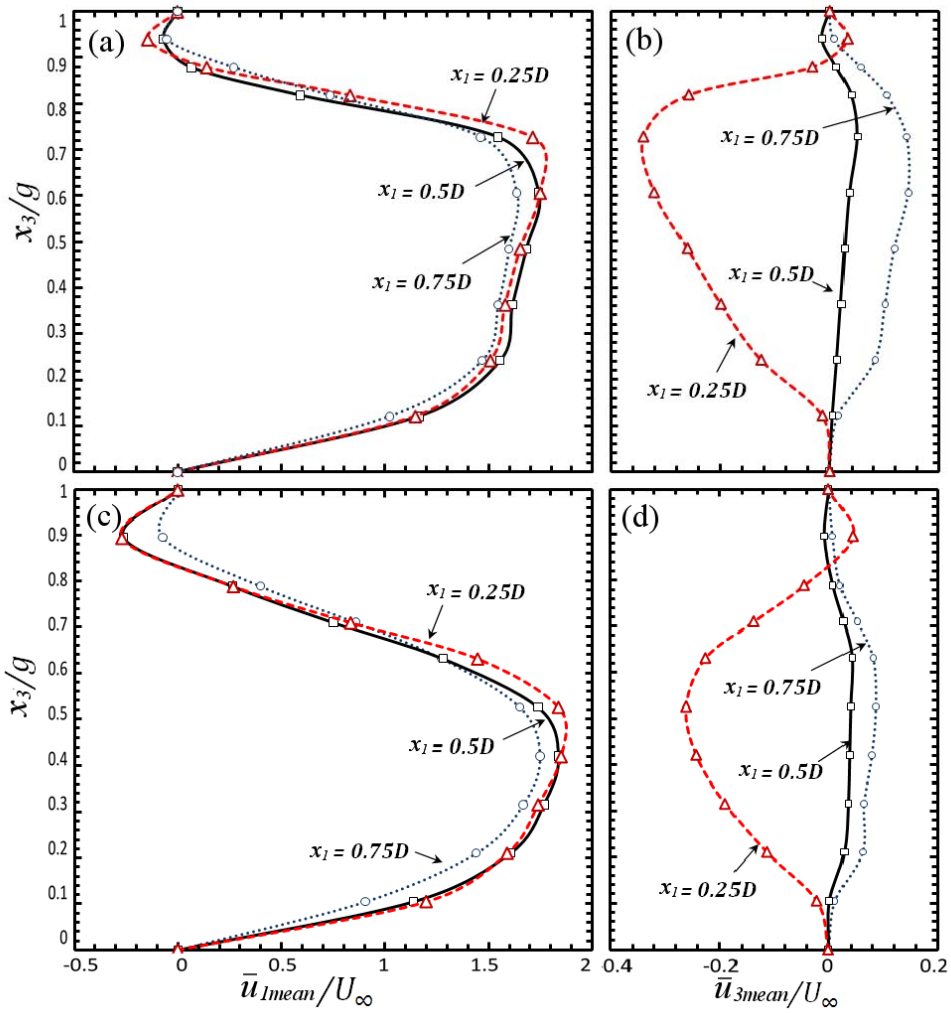

Figure 3.5: Averaged velocity profiles in the gap region, (a): $\bar{u}_1$ for $g/D = 1$, (b): $\bar{u}_3$ for $g/D = 1$, (c): $\bar{u}_1$ for $g/D = 0.5$ and (d): $\bar{u}_3$ for $g/D = 0.5$

previous studies, e.g. [21], [22] and [23]. When the cylinder is located on the ground plane, the secondary cell on the wall merges with the top recirculation bubble and forms a single large vortical region behind

the obstacle. For this geometry, the bottom recirculation bubble in the wake is completely suppressed by the wall, Figures 3.4(g) and 3.4(h).

Time-averaged velocity profiles in the gap between the lower face of cylinder and the wall are plotted in Figure 3.5 for gap ratios of $g/D = 1$ and $g/D = 0.5$ and for three different streamwise locations. The locations are measured from the leading edge of the cylinder. As shown, the streamwise flow in the gap is generally higher than the free stream value. However, along the lower surface of the cylinder, the flow decelerates and a small region of reverse flow is observed. Interestingly, the size of this region seems to be the same for both gap ratios; although in Figure 3.5(c) the reverse flow region looks to be twice the width of the region in Figure 3.5(a), since the vertical axis denotes the relative height (x_3/g), the actual sizes are almost equal. The vertical velocity profile is observed to be more dependent on the streamwise location: the velocity is mainly downward close to the leading-edge of the cylinder, but turns upward close to the exit of the gap. This upward flow at the trailing-edge is due to the interaction between the wake vortices and the vortex attached to the wall, which deflects the exit flow upward (see Figures 3.4(d) and 3.4(f)). The predicted velocity profiles are in a good agreement with those documented in the existing literature, e.g. [24-26].

3.3.2 POD analysis:

As explained earlier, POD enables to decompose a flow field into a set of flow structures, (sometimes referred to as topologies) that make different individual contributions to the overall flow. A proper criterion to determine the contribution of each structure is to measure the relative turbulent kinetic energy (TKE) of each topology. Figure 3.6 compares the energy spectrum for the four different gap ratios considered. For the no-wall case (denoted $g/D = \infty$), the first two modes contain a larger fraction of the total TKE compared to the other cases. This can be explained by the fact that the flow for the free cylinder is dominated by the periodic Kármán vortex shedding. For gap ratio's of $g/D = 1$ and $g/D = 0.5$, although vortex shedding still exists, it is not as energetic as for the no-wall case. This

dominancy almost disappears for the case where the cylinder is located on the wall (denoted $g/D = 0$). Another characteristic of the free cylinder case without any bounding wall is that the energy of the next few modes is significantly smaller than the same modes of the cases where a wall is present; this is especially noticeable for modes 4 to 10. This may suggest that for the three cases with a wall present, the structures represented by modes 4 to 10 are associated with and perhaps generated by the solid wall. Although the energy spectrum is helpful in comparing the distribution of eigenmodes, it only provides partial information.

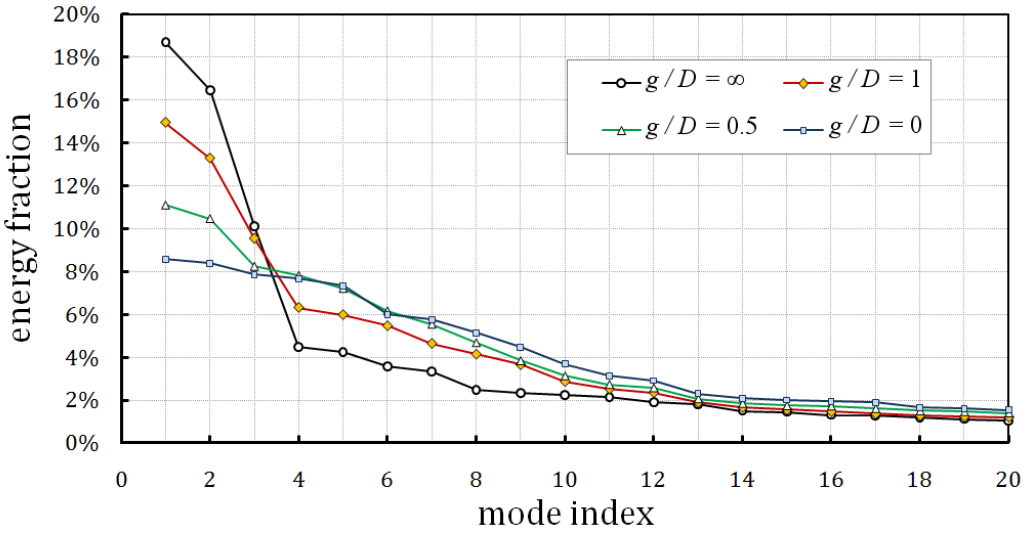

Figure 3.6: Decay of energy for different gap ratios

Figure 3.7 displays the first three POD modes, for the four cases studied in terms of the streamwise velocity component (ϕ_{u_1}). For the no-wall case, the first two modes represent a travelling wave characteristic, where the second mode is a phase shift of the first mode, see Figures 3.7(a) and 3.7(b). These periodic modes are attributed to the Kármán vortex shedding. On the other hand, the third mode is of a different nature than the first two, as can be noticed from its topology, Figure 3.7(c). The travelling wave characteristic is still noticeable in the first two modes of the $g/D = 1$ case, Figures 3.7(d) and 3.7(e). It seems that the wall does not strongly influence the vortex shedding; although the structures are somewhat distorted and inclined away from the wall, the travelling wave characteristic persists. However,

some distinct near-wall structures begin to appear in the third mode, Figure 3.7(f). For smaller gap ratios the second mode does not give the impression of being a phase-shifted version of the first mode, but instead appears to be strongly affected by the nearby wall, Figures 3.7(g) and 3.7(h). The energetic structures originated by the wall are stronger than for the previous case and being to appear in the second mode. Finally, for case where the cylinder sits on the wall, while the first two modes show some wave-like behavior, it is distinct from the vortex shedding case, Figures 3.7(j) and 3.7(k). Unlike the previous three cases, the topology of the third mode is not significantly different from the first two, and hence the third mode is not of a different nature from the first two, Figure 3.7(l). This also explains why the energy content does not change significantly from eigenmode 2 to 3 for the $g/D = 0$ case shown in Figure 3.6. This is another example of how the energy spectrum can be linked to the mode topologies to explain thecoherent structures in a turbulent flow.

The first three eigenmodes for the wall-normal component velocity component (ϕ_{u_2}) are displayed in Figure 3.8, using the same layout as in Figure 3.7. Figures 3.8(a) through (f) support the previous discussion regarding the nature of the first three modes. Unlike the case of the streamwise velocity, the energetic wall related structures do not appear in the first three modes, even for the case of a narrow gap as in Figures 3.8(g) and 3.8(h). However, at some point, the wall begins to deform and change the shape of the structures, as shown in Figure 3.8(i).

Lastly, the first three energetic structures in terms of streamlines overlaid on the spanwise vorticity contours (ϕ_{ω_2}) are presented in Figure 3.9. The streamlines provide a sense of the complex flow patterns created by the different modes. In fact, this figure is the "richest" in terms of portraying the flow topology and its influence by the wall; the formation of smaller vortex structures at the wall, for smaller gap ratios, can be detected. This figure also illustrates how as the wall approaches, the energetic structures generated by the wall become more prominent and begin to dominate the lower modes. For example, for the case of the cylinder on the wall, even the first mode is influenced by the interaction of wall structures and the prismatic obstacle. A remarkable conclusion which can be drawn from this figure is that a nearby solid

wall not only pushes the structures upward (note the center of vortical structures), but also the structures tend to lean backward (note the distribution of vortical structures from the streamline patterns). This topology (and conclusion) is in accordance with previous study of square cylinder near a solid wall by Shi *et al.* [28].

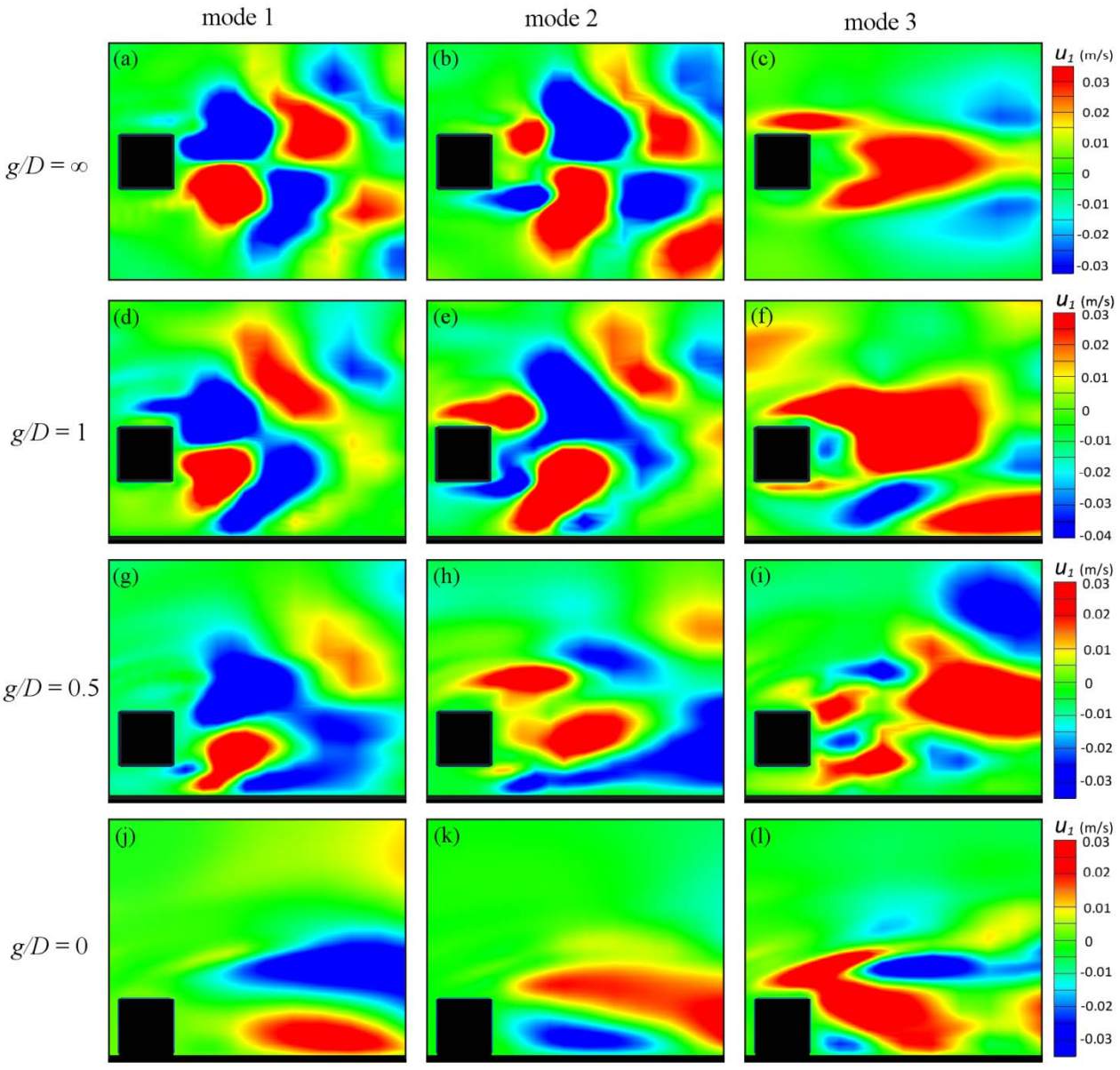

Figure 3.7: First three modes for the streamwise velocity component ϕ_{u_1}: (a) to (c): $g/D = \infty$, (d) to (f): $g/D = 1$, (g) to (i): $g/D = 0.5$, (j) to (l): $g/D = 0$

3.4 Conclusion and Recommendations

In this study, the effect of the wall proximity on the wake dynamics of flow over a square cylinder was investigated for different gap ratios. The numerical predictions provided by the LES were first verified as consistent with the results of other studies. The results indicated that although a nearby wall

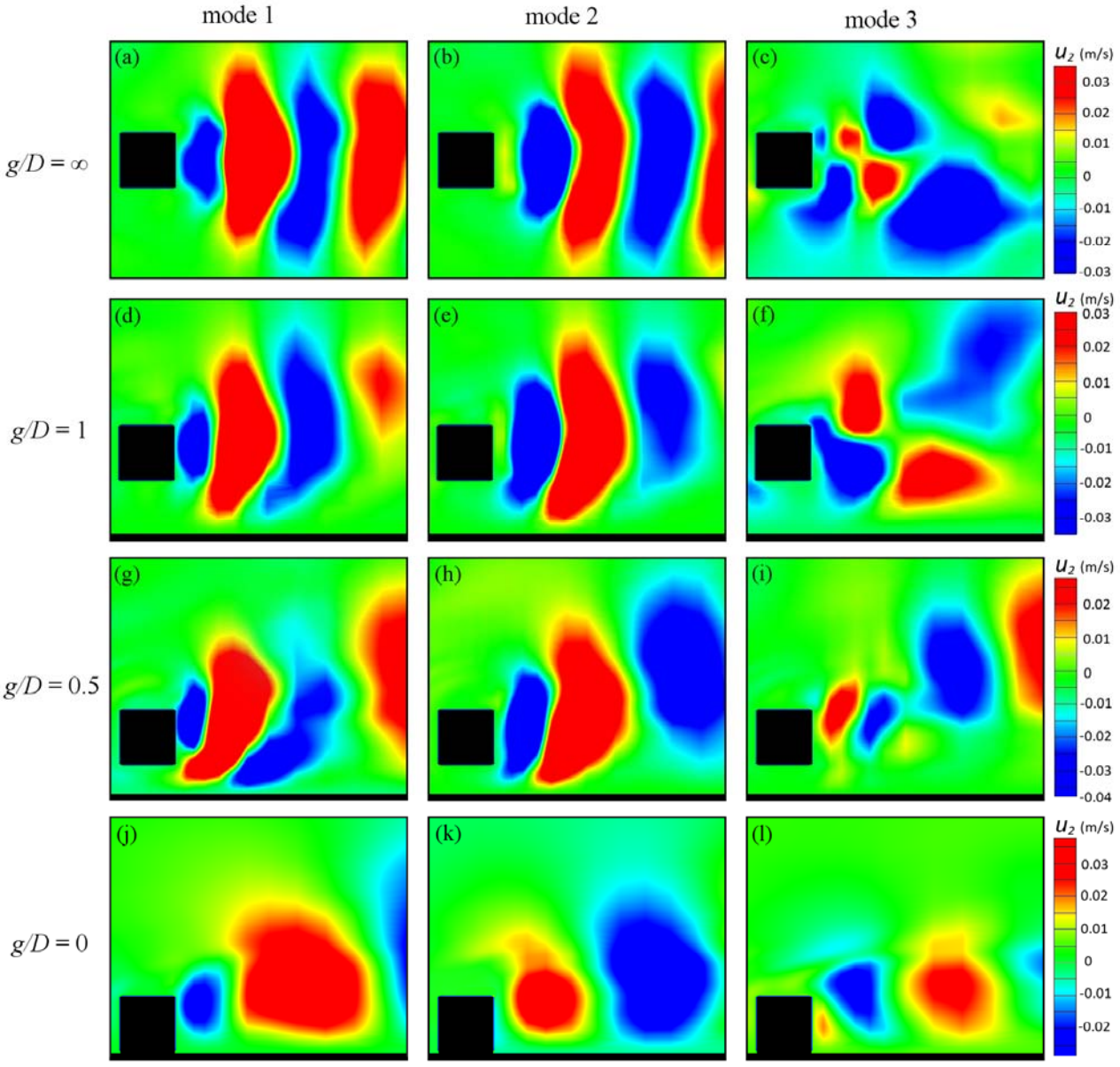

Figure 3.8: First three modes for the wall normal velocity component ϕ_{u_2}: (a) to (c): $g/D = \infty$, (d) to (f): $g/D = 1$, (g) to (i): $g/D = 0.5$, (j) to (l): $g/D = 0$

alters the values of the lift and drag coefficients, $\overline{C_L}$ and $\overline{C_D}$, its effect on the shedding frequency and Strouhal number is minimal. A POD analysis was performed to characterize the wake flow structures and identify those structures associated with the nearby wall. It was observed that the energy decay rate is slower for smaller gap widths, which means that the role of wall in the formation of energetic structures is more significant (than the role of cylinder itself) for smaller gap spaces. Lastly, it was observed that the vortical structures are being pushed away and lean backward in proximity of a solid wall.

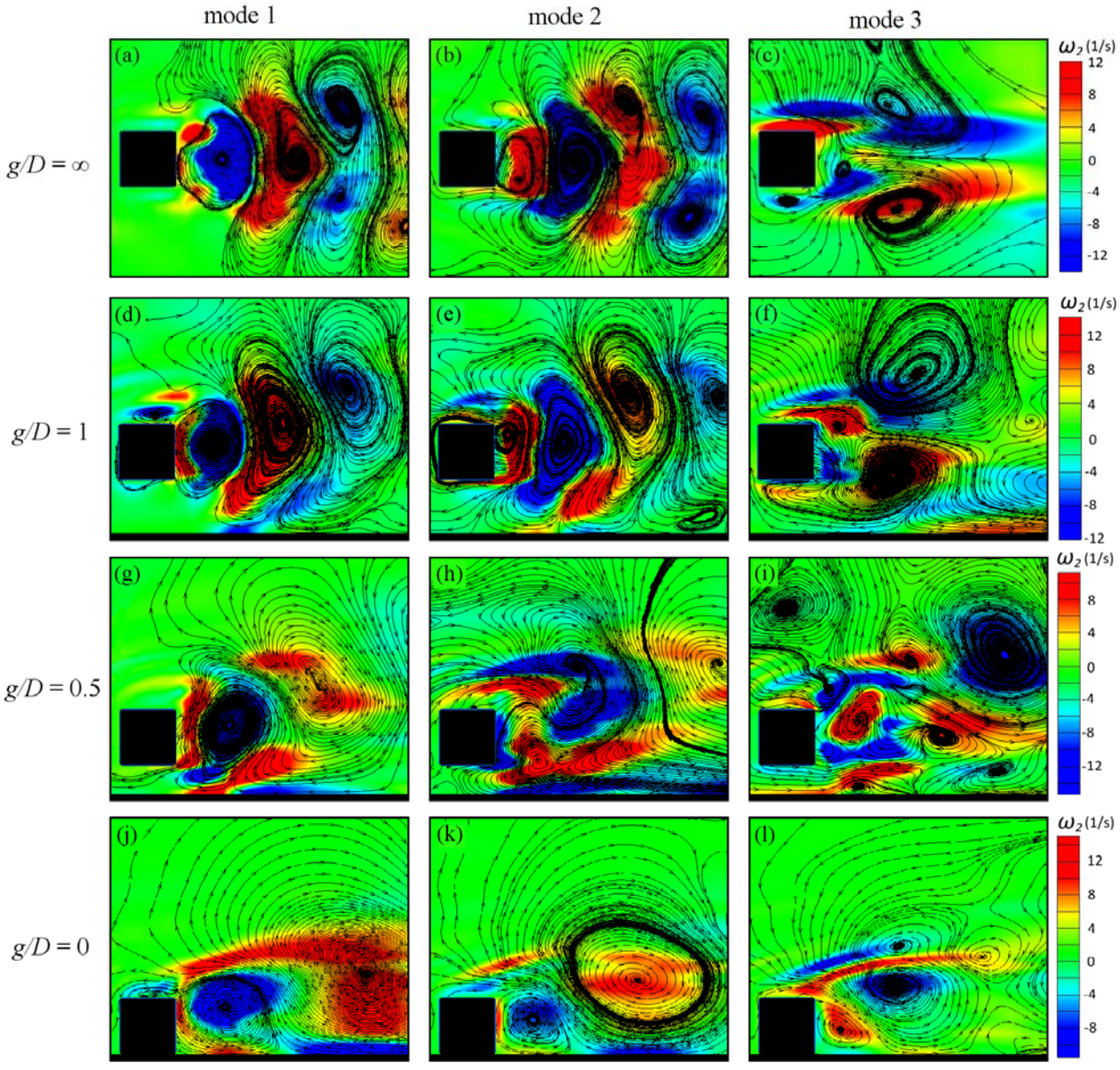

Figure 3.9: First three modes for the spanwise vorticity component ϕ_{ω_2}: (a) to (c): $g/D = \infty$, (d) to (f): $g/D = 1$, (g) to (i): $g/D = 0.5$, (j) to (l): $g/D = 0$

References

[1] S. Taneda, "Experimental investigation of vortex streets." *Journal of the Physical Society of Japan*, 20: 1714-1721, 1965.

[2] P. W. Bearman and M. M. Zdravkovich, "Flow around a circular cylinder near a plane boundary." *Journal of Fluid Mechanics*, 89: 33-47, 1978.

[3] S. Taniguchi and K. Miyakoshi, "Fluctuating fluid forces acting on a circular cylinder and interference with a plane wall." *Experiments in Fluids* 9: 197-204, 1990.

[4] G. Buresti and A. Lanciotti, "Mean and fluctuating forces on a circular cylinder in cross flow near a plane surface," *Journal of Wind Engineering and Industrial Aerodynamics*, 41: 639-650, 1992.

[5] C. Lei, L. Cheng and K. Kavanagh, "Re-examination of the effect of a plane boundary on force and vortex shedding of a circular cylinder." *Journal of Wind Engineering and Industrial Aerodynamics*, 80: 263-286, 1999.

[6] S. C. C. Bailey, G. A. Kopp and R. J. Martinuzzi, "Vortex shedding from a square cylinder near a wall." *Journal of Turbulence* 3: 1-18, 2002.

[7] G. Bosch, M. Kappler and W. Rodi, "Experiments on the flow past a square cylinder placed near a wall." *Experimental Thermal and Fluid Science* 13: 292–305, 1996.

[8] D. F. Durao, P. S. T. Gouveia and J. C. F. Pereira, "Velocity characteristic of the flow around a square cross section cylinder placed near a channel wall." *Experiments in Fluids* 11: 341–350, 1991.

[9] R. J. Martinuzzi, S. C. C. Bailey, G. A. Kopp, "Influence of wall proximity on vortex shedding from a square cylinder." *Experiments in Fluids* 34: 585–596, 2003.

[10] X. K. Wang and S. K. Tan, "Near-wake flow characteristics of a circular cylinder close to a wall." *Journal of Fluids and Structures*, 24: 605-627, 2008.

[11] S. J. Price, D. Sumner, J. G. Smith, K. Leong and M. P. Païdoussis, "Flow visualization around a circular cylinder near to a plane wall." *Journal of Fluids and Structures*, 16 (2): 175–191, 2002.

[12] W. -J. Lin, C. Lin, S. -C. Hsieh and S. Dey, "Flow characteristics around a circular cylinder placed horizontally above a plane boundary." *Journal of Engineering Mechanics*, 135: 697-715, 2009.

[13] H. Werner and H. Wengle, "Large-Eddy Simulation of Turbulent Flow over a Square Rib in a Channel." *Advances in Turbulence* 2: 418-423, 1989.

[14] R. Martinuzzi and C. Tropea, "The Flow Around Surface-Mounted, Prismatic Obstacles Placed in a Fully Developed Channel Flow." *Journal of Fluids Engineering*, 115: 85-92, 1993.

[15] M. M. Zdravkovich, *Flow Around Circular Cylinders, 1: Fundamentals*. Oxford University Press Inc., 1997.

[16] M. M. Zdravkovich, *Flow Around Circular Cylinders, 2: Applications*. Oxford University Press Inc, 2003.

[17] L. Sirovich, "Turbulence and the dynamics of coherent structures." Parts I, II and III. *Quarterly of Applied Mathematics*, 45: 561-571 and 573-590, 1987.

[18] M. Samani, M. Einian, D.J. Bergstrom, *Use of Proper Orthogonal Decomposition to Investigate the Large-Scale Dynamics in the Wake Region of an Infinite Square Cylinder*, 18th Annual Conference of the CFD Society of Canada, London, ON, Canada, May 17-19, 2010.

[19] M. Germano, U. Piomelli, P. Moin and W. H. Cabot, "A dynamic subgrid-scale eddy viscosity model." *Physics of Fluids*, A3: 1760-1765, 1991.

[20] D. K. Lilly, "A proposed modification of the Germano subgrid-scale closure method." *Physics of Fluids A,* 4: 633–635, 1992.

[21] S. Sarkar, "Large-Eddy Simulation of Wake and Boundary Layer Interactions Behind a Circular Cylinder." *Journal of Fluids Engineering*, 131: 1-13, 2009.

[22] M. Kumaran and S. Vengadesan, “Flow Characteristics Behind Rectangular Cylinder Placed Near a Wall.” *Numerical Heat Transfer*, Part A, 52: 643–660, 2007.

[23] I. Khabbouchi, M. S. Guellouz and S. Ben Nasrallah, “A study of the effect of the jet-like flow on the near wake behind a circular cylinder close to a plane wall.” *Experimental Thermal and Fluid Science* 44: 285–300, 2013.

[24] S. Bhattacharyya and D. K. Maiti, “Shear flow past a square cylinder near a wall.” *International Journal of Engineering Science*, 42: 2119–2134, 2004.

[25] T. Y. Kim, B. S. Lee and D. H. Lee, “Study on the Unsteady Wakes Past a Square Cylinder near a Wall.” *Journal of Mechanical Science and Technology*, 19 (5): 1169-1181, 2005.

[26] D. K. Maiti, “Numerical study on aerodynamic characteristics of rectangular cylinders near a wall.” *Ocean Engineering* 54: 251–260, 2012.

[27] G. Bosch and W. Rodi, “Simulation of vortex shedding past a square cylinder near a wall.” *International Journal of Heat and Fluid Flow*, 17 (3): 267–275, 1996.

[28] L. L. Shi, Y. Z. Liu and J. J. Wan, “Influence of wall proximity on characteristics of wake behind a square cylinder: PIV measurements and POD analysis.” *Experimental Thermal and Fluid Science*, 34: 28–36, 2010.

[29] A. Sohankar, C. Norberg and L. Davidson, “Simulation of three-dimensional flow around a square cylinder at moderate Reynolds numbers.” *Physics of Fluids*, 2: 288-306, 1999.

[30] N. Mahir, “Three-dimensional flow around a square cylinder near a wall” *Ocean Engineering*, 36: 357-367, 2009.

[31] S. Bhattacharyya and S. Dhinakaran,“Vortex shedding in shear flow past tandem square cylinders in the vicinity of a plane wall”, *Journal of Fluids and Structures*, 24: 400–417, 2008.

[32] T. Nishino, *Dynamics and Stability of flow past circular cylinder in ground effect*, Thesis for the degree of Doctor of Philosophy, University of Southampton, October 2007.

[33] A. Roshko, A. Steinolfson and V. Chattoorgoon, *Flow forces on a cylinder near a wall or near another cylinder*, Proceedings of the 2nd U.S. National Conference on Wind Engineering Research, Colorado State University, Fort Collins, June 22-25, 1975.

[34] M. Hiwada, I. Mabuchi, M. Kumada and H. Iwakoshi, "Effect of the turbulent boundary layer thickness on the flow characteristics around a circular cylinder near a plane surface", *Transactions of the Japan Society of Mechanical Engineers,* B 52: 2566-2574, 1986.

[35] S. Dutta, P. K. Panigrahi and K. Muralidhar, "Experimental investigation of flow past a square cylinder at an angle of incidence", *Journal of Engineering Mechanics*, 134: 788–803, 2008.

[36] R. W. Davis, E. F. Moore and L. P. Purtell, "A numerical-experimental study of confined flow around rectangular cylinders", *Physics of Fluids*, 23: 46–59, 1984.

Chapter 4

Turbulent Couette Flow with Rib-Roughness: A Study of the Coherent Structures using Proper Orthogonal Decomposition

A similar version of this chapter has been submitted as:

> M. Samani and D. J. Bergstrom, "Turbulent Couette flow with rib-roughness: a study of the coherent structures using Proper Orthogonal Decomposition", *International Journal of Heat and Fluid Flow* (under review).
>
> The flow simulation results and POD analysis were developed by the first author. Partial development of the POD routine formulation as well as initiating the LES code were contributed by the second author.

In addition a part of this chapter was presented at the following conference:

- M. Samani and D.J. Bergstrom, *Use of POD to Investigate Large-Scale Structures in Turbulent Flow with Rib-Roughness*, The 63rd Annual Meeting of the American Physical Society's Division of Fluid Dynamics (DFD), Long Beach, California, USA, November 21-23, 2010.

  The flow simulation results and POD analysis were developed by the first author. Partial development of the POD routine formulation as well as initiating the LES code were performed by the second author.

Preamble:

After verifying and validating the LES technique and POD algorithm in the first step, and making proper revisions to the LES code in the second step, the ultimate target of this research can be addressed, which is to study turbulent flows over rough walls and investigate the structures generated by the roughness, by making comparison to similar turbulent flows over smooth walls. In order to make this comparison in similar flow conditions, an asymmetric channel with one smooth wall and one roughened wall was implemented in a single study.

To make this last step special and unique, both in terms of simulation and POD analysis, the pressure gradient was removed and a moving top surface was added instead, such that the flow would solely be driven by the motion of the top surface. So, unlike the previous study cases, the available literature on this study case (asymmetric Couette channel flow) is scarce. As a result, this chapter has contributions in both aspects of this study (LES and POD) and therefore both aspects are equally emphasized.

This chapter recaps the contributions and outcomes of the first two steps and opens up some innovative ideas in terms of using POD capabilities to improve the accuracy and fidelity of turbulent flow simulation for future studies.

Abstract

A numerical study of the structures in turbulent Couette flow with roughness on one wall is performed. The hydrodynamic roughness was created by a series of ribs of square cross-section mounted perpendicular to the flow and distributed uniformly in the streamwise direction. The effect of both roughened and smooth surfaces was examined by implementing a moving top surface which was smooth and a roughened bottom wall. The domain was discretized using a non-uniform collocated grid and the flow solved using a second-order finite volume code. Large Eddy Simulation (LES) with a dynamic Smagorinsky subgrid-scale model was used to obtain the large-scale velocity field. Comparison with experiments and other numerical studies indicated that the predictions for the resolved-scale and fluctuating velocity fields were realistic. The velocity distribution near the top wall has the prototypic characteristics of a smooth surface, while transitional roughness was present on the bottom wall. The mean resolved-scale velocity field is characterized by a secondary flow consisting of two counter-rotating cells aligned in the streamwise direction. Proper Orthogonal Decomposition (POD) was used to investigate the dynamic behavior of the large-scale three-dimensional, time-dependent flow structures. The results show that in the proximity of each rib, the structures are mostly influenced by the neighboring ribs, while the topology in core region is mainly determined by the flow type, i.e. Couette flow. Some structures in the core region are shown to be displaced upwards by the rough surface. The topology of the coherent structures was also analysed and the contribution of each structure to the total fluctuating kinetic energy was determined. Qualitative analyses of these topologies provided insight as to the interaction of the ribs with the turbulence in the core region. Lastly, a quantitative analysis of POD temporal coefficients was performed, which revealed a quasi-periodic time-variation of the POD components.

4.1 Introduction

There have been many previous numerical and experimental studies of turbulent flow over smooth surfaces. However, in reality a perfectly smooth surface does not exist as any surface has some finite roughness and therefore all practical flows occur over rough surfaces. Despite this fact, far less information is available for turbulent flows over rough walls.

Due to the geometric simplicity, two-dimensional spanwise ribs have been previously used to simulate roughness elements. These simple two-dimensional geometries can generate highly three-dimensional structures in the inner layer and cause significant changes in the turbulence motions in the outer flow. Accordingly, one can divide the flow field into two regions: the wall dominant region where the surface roughness has a direct effect, and the outer region, where the effect of the surface is indirect. For rib roughness elements, due to the existence of sharp corners, the geometry predetermines the separation point which is the leading corner of the element, or the rear corner for low Reynolds number flows. The flow separation creates a small wake region behind the ribs, and the pressure distribution on the ribs creates a pressure drag which increases the effective wall shear stress.

A pioneering experimental study of turbulent channel flow with roughness elements on one wall was performed by Hanjalic and Launder [1]. With the advent of computational methods and the rapid development of computers, numerical analysis of two- and three-dimensional roughness elements has attracted more attention. Direct numerical simulation (DNS) of pressure driven channel flow with transverse rib roughness was performed by Miyake *et al.* [3]. Later, Ikeda and Durbin [4] performed DNS of a configuration with uneven rib heights. In a Large Eddy Simulation (LES) study, Cui *et al.* [5], studied mean and instantaneous flow structures of this arrangement for different spacing between elements. Leonardi *et al.* [6-7] performed DNS of turbulent channel flow with a rib-roughened wall for a wide range of w/k values, where w is the separation distance between the rib elements and k is the rib height. Nagano *et al.* [8] performed a Direct Numerical Simulation (DNS) study of channel flow with rib

roughness including heat transfer for different type of elements and different spacing, and investigated the statistical properties of both the velocity and thermal fields. They also studied rectangular ribs with non-square cross sections. Jimenez [9] studied the interaction between the viscous sublayer and the outer flow in turbulent near-wall flow, and concluded that at sufficiently large Reynolds numbers the dependency of the outer flow structures on the surface roughness is very weak. Using both hot-wire anemometry and DNS, Krogstad *et al.* [10] studied a fully turbulent pressure-driven symmetric channel flow for cases with smooth walls and rod-roughness on both walls. Similar symmetric configurations have been studied by other authors, e.g. Bakken *et al.* [11] and Ashrafian *et al.* [12]. Orlandi *et al.* [13] investigated the effect of element shape and orientation on the turbulence structure using DNS. Later, Burattini *et al*. [14] performed simultaneous experimental and numerical analyses of asymmetric channel flow with roughness on one wall for a range of Reynolds numbers. They extensively studied the statistical moments of the velocity fluctuations, length scales and turbulent energy spectra, and their variation with Reynolds number.

In the current study, a two-dimensional turbulent channel flow is considered, which is driven not by a pressure gradient, but rather by the motion of one wall relative to the other, i.e. turbulent Couette flow. Aydin and Leutheusser [2] experimentally studied plane Couette flow, in one case with two smooth walls, and in the other case with two rough walls. They compared the mean velocity distribution and turbulent intensities between the smooth and rough wall cases, and the flow was symmetric for both cases. To the authors' knowledge no one has yet studied turbulent plane Couette flow with rib roughness on one wall. By performing DNS of a plane Couette flow, Papavassiliou and Hanratty [15] investigated large scale secondary flow structures, which cannot be observed in pressure-driven flows. Notwithstanding the capability and accuracy of DNS in resolving the complete range of turbulent motions, the large eddies dominate the turbulent transport and therefore in this study the turbulent flow is simulated using the LES approach. Wang and Bergstrom [16] applied LES for a simulation of turbulent Couette flow for a similar Reynolds number. The main focus of this study was on analyzing the large-scale velocity structures in

turbulent Couette channel flow and the flow topology associated with the roughness elements using Proper Orthogonal Decomposition (POD). Moehlis *et al.* [17] employed POD to model a plane Couette flow. Their work was extended later by Smith *et al.* [18] to obtain a low-dimensional model in a minimal flow unit. Tsukahara *et al.* [19] extracted three-dimensional spatial POD modes from a DNS analysis of a plane Couette flow.

In the present study, rib elements are periodically arranged in the streamwise direction. The Reynolds number based on the velocity of the top wall and channel half-width is set to $Re = 2600$ with the aim of facilitating comparisons to the existing literature. Since the Reynolds number is relatively low and the rib height, k, is relatively large compared to the channel height, h, the roughness elements are expected to have a noticeable influence on the turbulent structures. Of specific interest is the interaction of the rib wakes with the outer flow above. Note that the choice of this geometry also allows direct comparison between the smooth and rough wall, since they have the same friction velocity (U_τ) value. The snapshot POD method of Sirovich [20] is used to investigate the flow results from LES. The POD analysis specifically considers two-dimensional velocity and vorticity components in plane sections which are aligned perpendicular and parallel to the outer flow. This analysis required use of a relatively large number of snapshots spread over a sufficiently long time period so that the velocity fields are independent of each other, which was efficiently accomplished using the LES approach to simulate the turbulent velocity field.

4.2 Computational Methodology

4.2.1 Flow physics, transport equations and numerical approach:

To model the turbulent flow in this study, the LES method was employed. First, a spatial filter is used to filter the incompressible Navier-Stokes (NS) and continuity equations to obtain

$$\frac{\partial \bar{\boldsymbol{u}}_{\boldsymbol{i}}}{\partial t} + \frac{\partial\left(\bar{\boldsymbol{u}}_{\boldsymbol{i}}\bar{\boldsymbol{u}}_{\boldsymbol{j}}\right)}{\partial \boldsymbol{x}_{\boldsymbol{j}}} = -\frac{\partial p}{\partial \boldsymbol{x}_{\boldsymbol{i}}} + \frac{1}{Re}\frac{\partial^2 \bar{\boldsymbol{u}}_{\boldsymbol{i}}}{\partial \boldsymbol{x}_{\boldsymbol{j}}\partial \boldsymbol{x}_{\boldsymbol{j}}} - \frac{\partial \tau_{ij}}{\partial \boldsymbol{x}_{\boldsymbol{j}}} \tag{4.1}$$

and

$$\frac{\partial \bar{\boldsymbol{u}}_{\boldsymbol{i}}}{\partial \boldsymbol{x}_{\boldsymbol{i}}} = 0, \tag{4.2}$$

where $\bar{\boldsymbol{u}}_{\boldsymbol{i}}$ is the filtered velocity, t is the time, p is the local pressure, ρ is the density, $\boldsymbol{x}_{\boldsymbol{i}}$ is the corresponding Cartesian coordinate and τ_{ij} is the subgrid-scale stress (SGS) term. In this work, an eddy viscosity formulation was employed to express the SGS stress in terms of the resolved-scale velocity field, i.e.

$$\tau_{ij} - \frac{1}{3}\delta_{ij}\tau_{kk} = -2\nu_{SGS}\bar{S}_{ij}, \tag{4.3}$$

where $\bar{S}_{ij} = \frac{1}{2}\left(\partial \bar{u}_i/\partial x_j + \partial \bar{u}_j/\partial x_i\right)$. To model the SGS viscosity (ν_{SGS}), the dynamic Smagorinsky model of Germano *et al.* [21] was implemented, in which ν_{SGS} is given by

$$\nu_{SGS} = C_s \Delta^2 |\bar{S}|, \tag{4.4}$$

where $|\bar{S}| = \left(2\bar{S}_{ij}\bar{S}_{ij}\right)^{\frac{1}{2}}$, Δ is the filter width and the dynamic coefficient C_s is determined as a variable of space and time. Further details of the mathematical procedure can be found in [21] and [22]. In the present formulation, both clipping and local volume averaging were used to stabilize the value of C_s.

A non-uniform collocated grid was used to discretize the governing equations using a cell-centered finite volume method. The discrete momentum equation was advanced in time using a semi-implicit Crank-Nicolson scheme as part of a fractional-step method. To ensure mass conservation at each time step, a pressure correction scheme was implemented using a multi-grid solver. The time step was set to a constant value of $\Delta t = 2 \times 10^{-4}$ which corresponds to the Courant–Friedrichs–Lewy (CFL) number of 0.35 and meets the convergence condition.

The theoretical relation for the mean velocity profile in a turbulent flow on a smooth surface is given by the classical two-layer wall-law of von-Kármán [23], i.e.

$$\begin{cases} {x_3}^+ \leq 5 & \Longrightarrow \quad {u_1}^+ = {x_3}^+ ; \qquad (4.5.a) \\ {x_3}^+ > 30 & \Longrightarrow \quad {u_1}^+ = \left(\frac{1}{\kappa}\right) ln\, {x_3}^+ + B\,. \qquad (4.5.b) \end{cases}$$

Here ${u_1}^+$ and ${x_3}^+$ are the dimensionless streamwise velocity and wall-distance components respectively, κ is the von-Kármán constant (≈ 0.41) and B is a constant (≈ 5).

For a rough surface, the form drag caused by the pressure forces on the roughness elements significantly modifies the resistance presented to the flow by the wall. Even though viscous drag exists, often it is relatively small compared to the form drag. The effect of roughness on the mean velocity profile can be expressed in wall units as follows,

$${u_1}^+ = \frac{1}{\kappa} \ln {x_3}^+ + B \pm \Delta {u_1}^+. \qquad (4.6)$$

In the above equation, ${u_1}^+$ is the mean velocity normalized by the friction velocity (U_τ) and ${x_3}^+$ is the dimensionless wall-normal distance normalized by the viscous length scale (ℓ_τ), where

$${u_1}^+ = \frac{u_1}{U_\tau}, \qquad (4.7a)$$

$$U_\tau = \sqrt{\frac{\tau_w}{\rho}}, \qquad (4.7b)$$

$$\tau_w = \mu \left(\frac{\partial u_1}{\partial x_3}\right)_{\text{wall}}, \qquad (4.7c)$$

$$\ell_\tau = \frac{\nu}{U_\tau}, \qquad (4.7d)$$

and

$${x_3}^+ = \frac{x_3}{\ell_\tau}. \qquad (4.7e)$$

The roughness effect is given by the last term, Δu_1^+, which is called the roughness function and reflects the roughness geometry, i.e. the shape, height and distribution of the roughness elements. When plotted on a semi-log plot, the roughness function mathematically acts as a shift to the velocity profile for a smooth wall and as such quantifies the effect of roughness.

In the present study, the bottom wall is characterized by ribs of height k separated by a distance w. Figure 4.1 shows the channel configuration and defines the geometrical parameters. The top wall of the channel is located a distance of h (= 2δ) above the bottom wall, so that h/k = 16. The ribs are characterized by a pitch-to-height ratio of w/k = 7.5. This ratio was chosen because it is close to the value for which the maximum drag force occurs for a given rib height, and hence yields the maximum shift in the velocity profile ΔU^+, according to Leonardi *et al.* [6]. Since their study considered Poiseuille channel flow with one roughened wall, this value has not been verified for the Couette flow case.

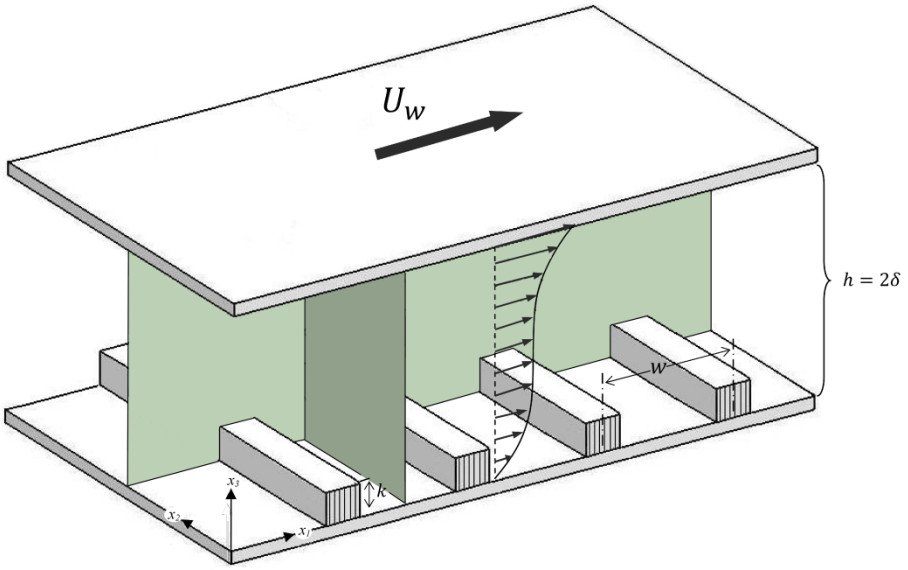

Figure 4.1: Geometrical sketch of the channel showing sampling planes

For plane Couette flow, the flow is driven solely by the movement of the top wall. The velocity of the top wall and channel half-width can be used to define the Reynolds number $Re = U_o h/\nu$, where the reference velocity is given by $U_o = U_w/2$. According to the study of Bech *et al.* [24], the transitional

Reynolds number for Couette flow in a channel with smooth walls is $Re_T \approx 720$ (or $Re_{\tau T} \approx 26$) and the critical Reynolds number for fully developed turbulent flow is $Re_C \approx 1000$ (or $Re_{\tau C} \approx 35$). In this work, the Reynolds number is set to $Re = 2600$ which ensures that the flow is fully turbulent and corresponds to a Reynolds number of $Re_\tau = 90$ based on the friction velocity.

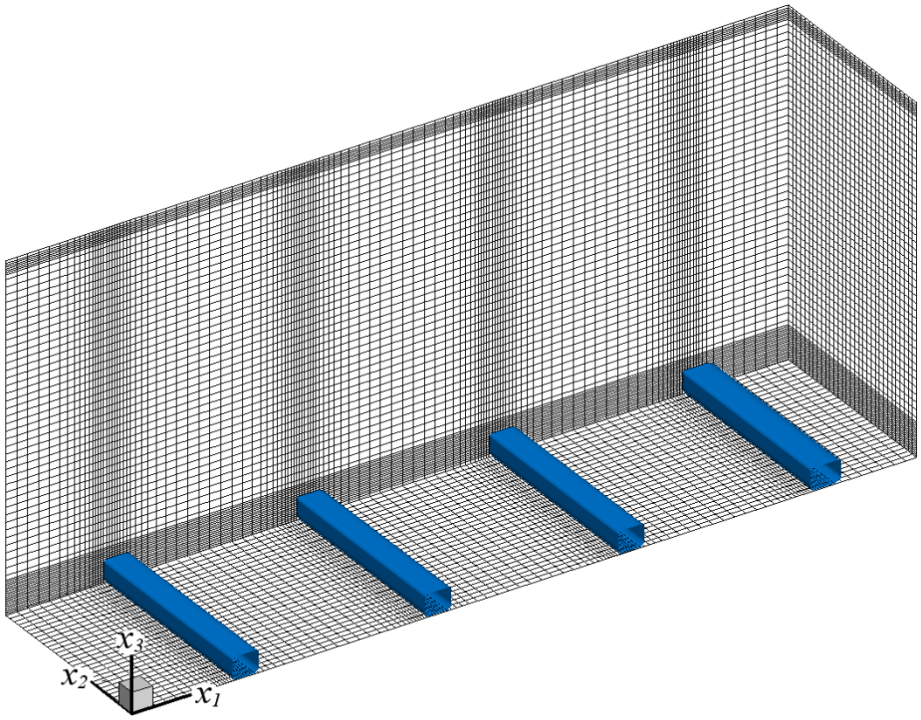

Figure 4.2: projected computational grid

To resolve the turbulent flow field, computations were performed on a rectangular domain of size $4.6\delta \times 1.0\delta \times 2.0\delta$ ($36k \times 8k \times 16k$) using a $128 \times 32 \times 64$ non-uniform grid, as shown in Figure 4.2. The flow behaves as an infinitely long and infinitely wide channel, since periodic boundary conditions were imposed on the streamwise and lateral surfaces of the domain. Blocks of $16 \times 32 \times 16$ control volumes were used to resolve the rib geometry, and the center of the first interior control volume is located at $x_3^+ = 1.27$ for the smooth wall and $x_3^+ = 0.94$ for the rough wall. Even though a relatively small number of control volumes was used to resolve the flow, the near-wall resolution is sufficient to resolve the flow very close to the wall, e.g. within the viscous sub-layer on the smooth wall.

4.2.2 Implementation of Proper Orthogonal Decomposition:

Given a set of apparently random and complex flow fields, it would be desirable to determine an optimally correlated relationship among them, which is the motivation for using the POD methodology to analyze turbulent flows. The correlated features or so called "coherent structures" represent the energy containing structures in an evolving flow dynamics. In this case, the two-dimensional fluctuating velocity and vorticity fields are used as the input data. The fluctuating field can be obtained by subtracting the mean field from the instantaneous field, e.g. for the velocity field in a streamwise sampling plane, $\boldsymbol{u_i'(x_2, x_3, t) = u_i\ (x_2, x_3, t) - \overline{u}_i(x_2, x_3)}$. A two-point velocity correlation matrix can be generated using these fluctuating fields, i.e.

$$C(t,t') = \frac{1}{N}\int_{\Omega} [\boldsymbol{u_i'(x_2, x_3, t)u_i'(x_2, x_3, t')}]\, d\boldsymbol{x_2}\, d\boldsymbol{x_3}, \tag{4.8}$$

where N is the total number of snapshots and Ω denotes the spatial domain. After solving the following eigenvalue problem

$$\int C(t,t')a_n(t')dt' = \lambda_n a_n(t), \tag{4.9}$$

a series of eigenvalues and corresponding eigenvectors are obtained. The eigenvalue of each mode represents twice the turbulence kinetic energy (TKE) associated with that mode, and consequently summation of the eigenvalues gives twice the total TKE for the flow. The coefficient $(a_n(t))$ represents the amplitude corresponding to spatial mode $\boldsymbol{\phi_n(x_2, x_3)}$, and can be used to decompose the time-dependent fluctuating part of the velocity field into a sum of orthonormal spatial modes $(\boldsymbol{\phi_n(x_2, x_3)})$ and associated temporal coefficients $(a_n(t))$, i.e.

$$\boldsymbol{u_i'(x_2, x_3, t)} = \sum_{n=1}^{N} a_n(t)\boldsymbol{\phi_n(x_2, x_3)}. \tag{4.10}$$

To obtain the 2D "coherent structures", one can use the following relation

$$\phi_m(\boldsymbol{x_2}, \boldsymbol{x_3}) = \sum_{k=1}^{K} a_m(t_k)\boldsymbol{u_i'}(\boldsymbol{x_2}, \boldsymbol{x_3}, t_k). \quad (4.11)$$

Finally, a specific velocity field of the total ensemble can be reproduced as follows,

$$u(y, z, t_n) = \sum_{m=1}^{M} a_m(t_n)\phi^m(y, z). \quad (4.12)$$

The snapshots were collected after the initial transient field had decayed so that the turbulent flow was statistically stationary. The instantaneous velocity field was sampled on two-dimensional slices (snapshots) of the flow field taken perpendicular to the rods (x_1-x_3 plane) and perpendicular to the flow direction (x_2-x_3 plane). In each plane, two-dimensional velocity and vorticity components were used as the computational data for the POD analysis. In total N = 2200 snapshots were sampled over a time duration of 180 non-dimensional time units (w/U_w). As noted previously, part of the motivation for using a relatively small-scale LES was to facilitate collection of the ensemble of snapshots required for the POD.

4.3 Selected Results and Discussion

4.3.1 Validation of Couette flow results:

In order to validate the LES results, select features of the turbulent mean flow were compared to the results from previous studies. The resolved-scale time-averaged velocity profile, normalized using the outer scales, is plotted in Figure 4.3, along with the results of some other smooth-wall and rough-wall studies. Note that the profile is averaged in time and also averaged spatially along the gap between two consecutive ribs. Due to the existence of recirculation zones in the gap between the ribs, a small region of reverse flow is evident in the vicinity of the ground surface. A practical practice in such cases, e.g. as done in [26], is to define a virtual origin which corresponds to the location where mean velocity is zero. As expected, the turbulent velocity profile deviates significantly from the linear profile obtained for

laminar flow indicated by the dashed line. Recall that the flow along the top wall is characteristic of a smooth surface. Near the top wall, the present results show fairly good agreement with previous studies on smooth walls, e.g. the experimental study of [2] and LES of [16], especially in close proximity to the wall.

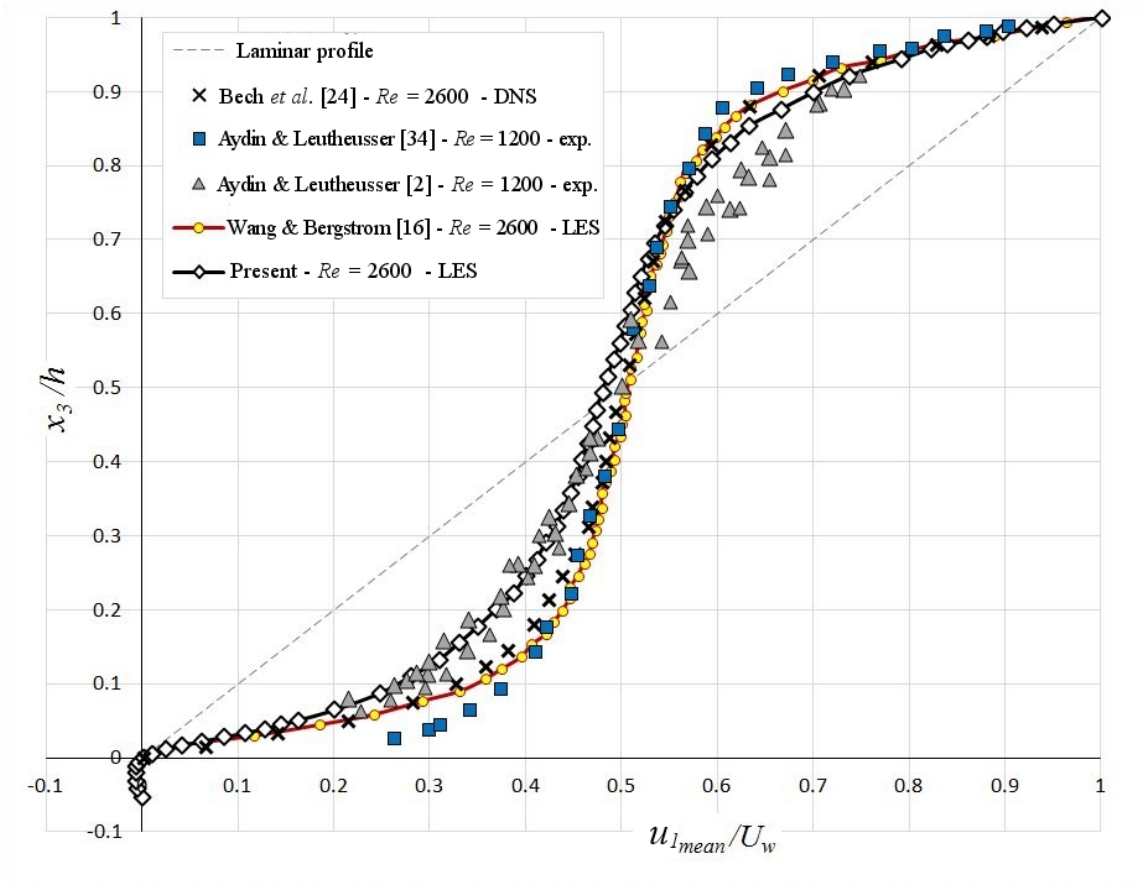

Figure 4.3: Mean velocity distribution across the channel

As one moves away from the top wall towards the center of the channel, the present profile deviates from the smooth wall profile and moves toward the rough profile of Aydin and Leutheusser [2]. This behavior indicates that the rib roughness on the bottom wall affects the flow near the top wall, which is expected considering fairly high blockage of rib elements. At the present time it is not clear what flow mechanism is responsible for this behavior. A similar effect has been observed in Poiseuille flows with rib-roughness on just a single wall, e.g. [1, 5, 13]. The mean velocity profile near the bottom wall clearly shows the influence of the ribs, which reduce the velocity below that on a smooth surface. In this case,

there is close agreement over much of the lower half of the channel with the profile measured by Aydin and Leutheusser [2] for a channel with roughness on both walls at a much higher Reynolds number.

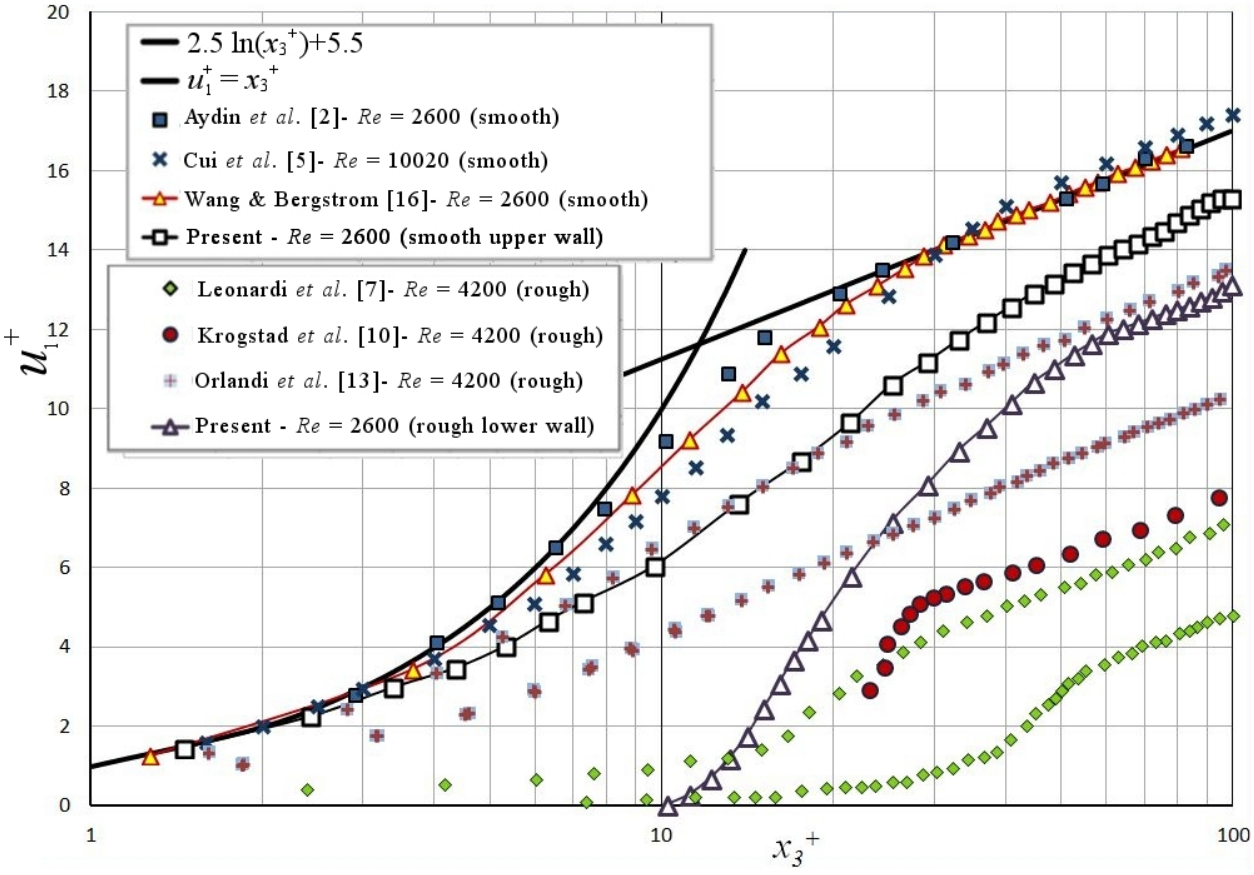

Figure 4.4: Mean velocity distribution expressed in wall coordinates

To further investigate the mean velocity field, the velocity profiles are presented using universal wall coordinates in Figure 4.4. The velocity profiles are plotted referenced to the nearest wall, in anticipation of comparing smooth and rough wall characteristics. Note that reference profiles are provided for both symmetric ([2, 16]) and asymmetric ([6, 13]) cases; for the symmetric flows, a single velocity profile is shown, while for the asymmetric flows, smooth and rough wall profiles are included. Near the top wall, the velocity profile sits below the smooth wall velocity profiles of [2] and [16]. This is consistent with other studies which used roughness on only one wall [5, 7, 8, 13], and indicates that the effect of roughness has a strong effect on the velocity profile on the opposite wall. Note that very close to the top

wall, the present velocity profile approaches the linear profile of the viscous sublayer on a smooth surface. The velocity profile on the rough wall exhibits the characteristic roughness shift due to the enhanced wall shear stress created by the ribs. The value of the roughness shift in this study was $|\Delta u_1{}^+|$ = 2.1, which indicates that the flow is in the transitional roughness regime ([9]). Table 4.1 compares this value with some previous Poiseuille flow studies with different Reynolds numbers and geometries. The fact that the ribs produced only transitional roughness in the present study may be due to the nature of the flow, i.e. Couette versus Poiseuille, and also reflect the difference in Reynolds number. Note that the velocity profile on the rough wall has only a small logarithmic region, and transitions to the wall in a manner which indicates that viscous effects are still important. This is partly due to the fact that it is transitional roughness, and also reflects the fact that in the gap between ribs, the resistance at the wall is entirely due to viscosity.

	Re	*w/k*	$\|\Delta u_1{}^+\|$
Leonardi *et al.* [6]	4200	4	6.2
Leonardi *et al.* [7]	4200	7	7.7
Krogstad *et al.* [10]	4200	8	7.1
Orlandi *et al.* [13]	4200	7	6.5
This work	2600	7.5	2.1

Table 4.1: Comparison of roughness shift in different studies

In terms of the LES predictions for the turbulence field, the resolved-scale streamwise velocity fluctuation along the wall normal direction is presented in Figure 4.5 for both walls. As before, this profile is time-averaged and also averaged spatially over the gap between two consecutive ribs. On the smooth wall, the peak value in the present profile is approximately $u_{1_{rms}}/U_\tau = 2.55$, which is slightly less than that obtained by previous studies, e.g. $u_{1_{rms}}/U_\tau = 2.6$ by Bech *et al.* [24], $u_{1_{rms}}/U_\tau = 2.7$ by

Aydin and Leutheusser [2] and $u_{1_{rms}}/U_\tau = 2.8$ by Wang and Bergstrom [16]. Likewise, the location of the peak is shifted slightly away from the wall in the present simulation; the location is approximately ${x_3}^+ = 18$, compared with ${x_3}^+ = 11$ for Aydin and Leutheusser [2], ${x_3}^+ = 12$ for Bech *et al.* [24] and ${x_3}^+ = 14$ for Wang and Bergstrom [16]. In the core region of the channel, the present prediction tends to a constant value which is in agreement with the other studies. Overall, the resolved-scale streamwise velocity fluctuation on the smooth wall does not appear to be strongly affected by the roughness on the opposite side of the channel.

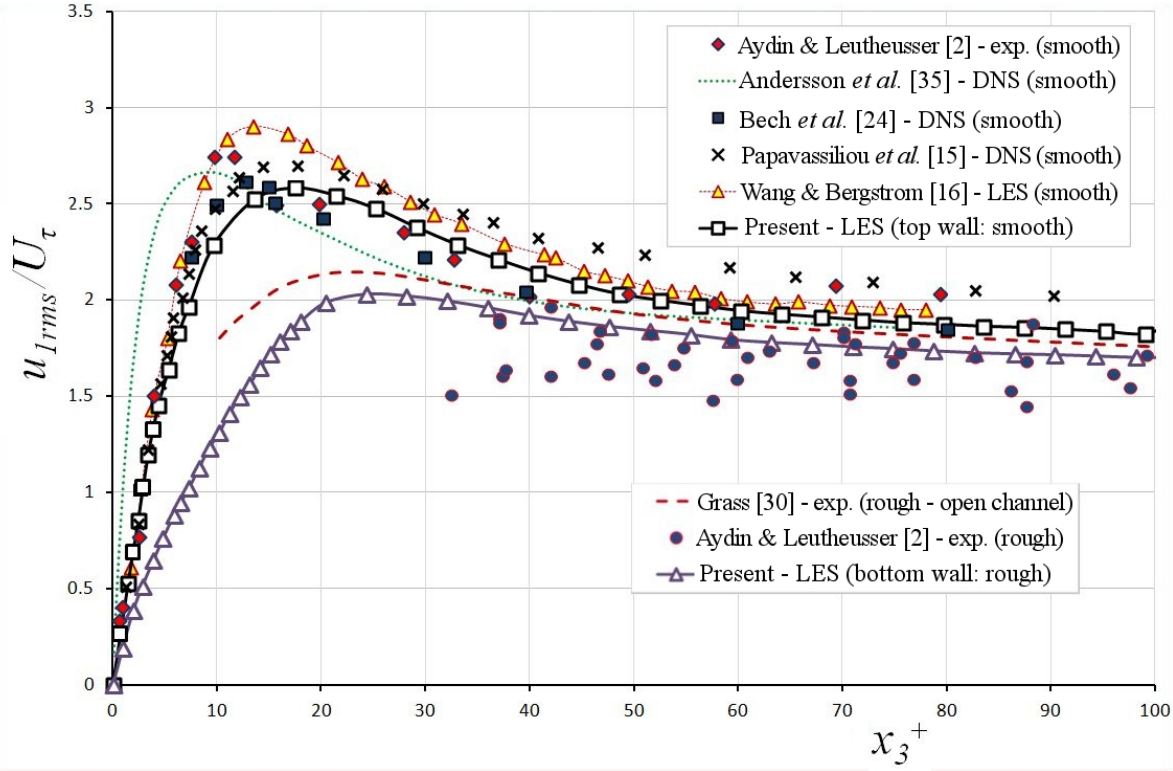

Figure 4.5: Profile of resolved-scale streamwise velocity fluctuation in wall coordinates

The profile of $u_{1_{rms}}/U_\tau$ for the rough wall is close to the measurements of Aydin and Leutheusser [2], as well as the open channel data of Grass [30], especially in the core region. The observed reduction in the peak and core values compared to the smooth wall case is consistent with the experimental results. This characteristic was attributed by Krogstad *et al.* [25] to the break-up of the streamwise vortices due to the rib elements.

Purely two-dimensional Couette flow is characterized by a constant shear stress profile. Figure 4.6 displays the budget of the total normalized shear stress plotted across the channel, including contributions from the viscous, resolved-scale and SGS transport. Note that the data in the reverse flow region on the rough surface are excluded from the plots. As previously mentioned, the wall normal distance is measured from the wall surface, i.e., just below the neutral axis. The viscous contribution ($\frac{\mu}{\tau_w}\langle\frac{\partial u_{1mean}}{\partial x_3}\rangle$) peaks

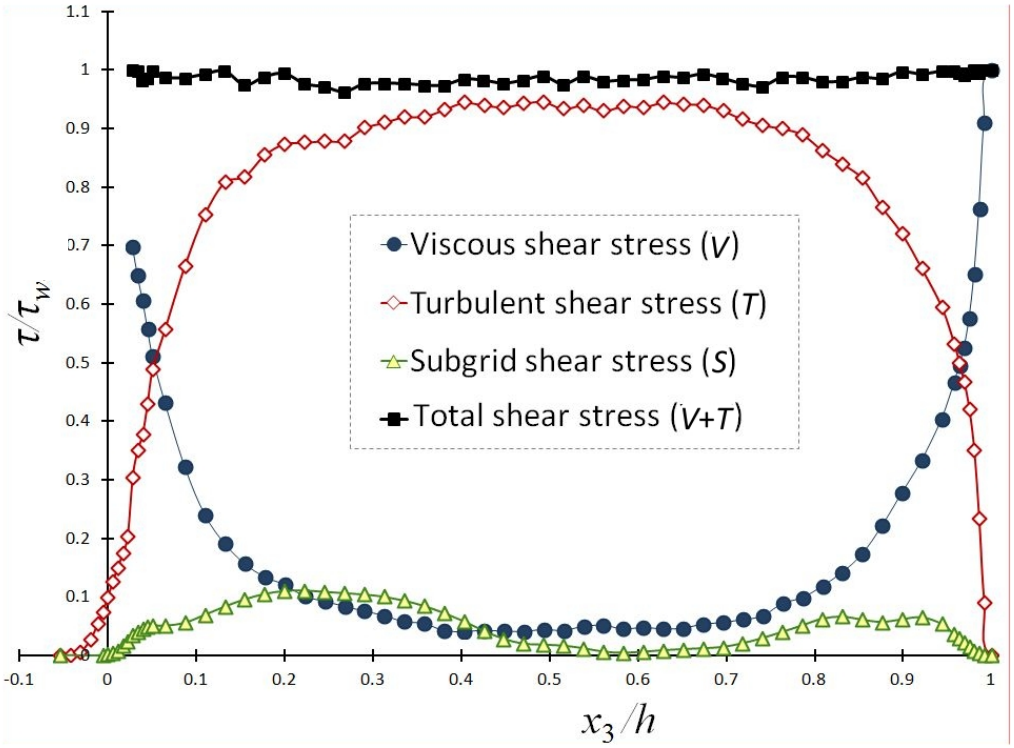

Figure 4.6: Shear stress profile across the channel

close to the walls, where the turbulent contribution is damped, and diminishes in the core region. The resolved-scale shear stress ($-\frac{\rho}{\tau_w}\overline{u_1'u_3'}$) exhibits the opposite trend, since turbulent transport is dominant in the core region. The sum of the viscous and resolved-scale contributions yields an approximately constant value equal to unity across the channel. The profile for the SGS stress contribution, ($\frac{\tau_{x_1x_3}}{U_\tau^2}$), is asymmetric, and is largest in proximity to the rough wall. Not included in the present figure is the contribution of the secondary flow, which is discussed later in the paper (see Figure 4.15). The SGS stress and secondary flow contributions tend to balance each other.

The time-averaged flow patterns have been compared to the instantaneous values in Figure 4.7 using streamlines and spanwise vorticity contours. More than 2200 samples were used to perform the time-averaging on the LES fields. The primary separation at the leading edge is well captured in both cases. The vorticity contours indicate that a high spanwise vorticity component exists near the upstream corner of ribs. In the core region of the channel, there are vortical structures of opposite sign, which do not appear to penetrate into the region between the ribs.

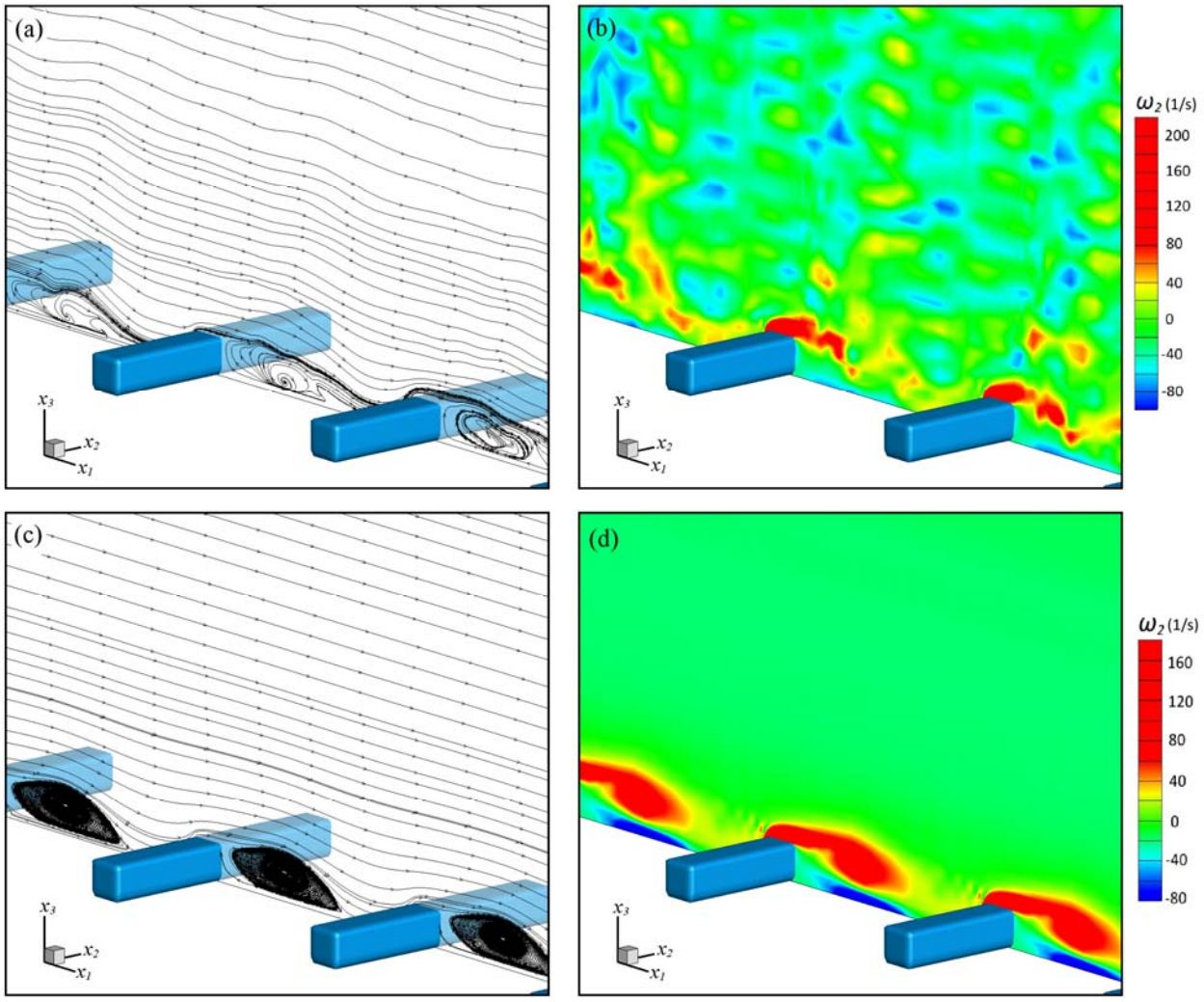

Figure 4.7: Mean and instantaneous flow patterns in terms of streamlines and spanwise vorticity: (a)-(b): instantaneous (ω_2); (c)-(d): mean ($\omega_{2_{mean}}$)

The time-averaged pattern of streamlines is shown for a single pair of ribs in Figure 4.8. The initial separation and reattachment phenomena are well captured, and the primary and two secondary recirculation zones are also resolved, which agree well with the results of other studies, e.g. [5] and [6]. The length of the recirculation cell and reattachment length are approximately 4*k* and 1.2*k*, respectively. These values are also comparable to previous measurements of rib-roughened walls, e.g. 4.8*k* by Leonardi *et al.* [6] and 5*k* by Liu *et al.* [27]. Note that these characteristics have significant implication for the form drag on the ribs.

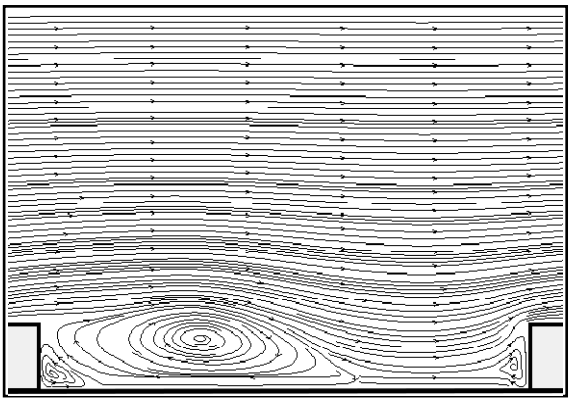

Figure 4.8: Time-averaged streamlines in spanwise plane

A qualitative analysis of the instantaneous flow in Figures 4.7(a) reveals that roughness elements have impact to some extent, on the mean flow in the outer region. However, the time-average streamlines far above the ribs are nearly parallel. In contrast, close to the rough wall the flow direction is drastically changed by the ribs, and in the proximity of the roughness elements the flow becomes spatially heterogeneous and three-dimensional. This feature is more noticeable in vector plots of the instantaneous velocity for different sections across the channel as shown in Figure 4.9. Figure 4.9(a) displays the vector field at an elevation of approximately $x_3 = 0.5k$ above the ground plane. Although the geometry is two-dimensional, complex spanwise motions, i.e. in the third dimension, are clearly evident. These spanwise features diminish as the sampling section moves toward the centre of the channel. Just above the crest of the ribs, a few weak spanwise motions can still be detected (Figure 4.9(b)) but further away from the ribs

(Figure 4.9(c)) the vectors are nearly parallel, indicating negligible impact of roughness elements on the mean flow in the outer region.

The above analysis documents the characteristics of the mean and instantaneous velocity fields predicted by the LES. Comparisons with other simulations and experiments indicate that the LES prediction provides a realistic simulation of low Reynolds number turbulent flow over a rib-roughened wall. The next section will use POD to specifically analyse the flow structure, especially the most energetic flow structures associated with the roughness elements.

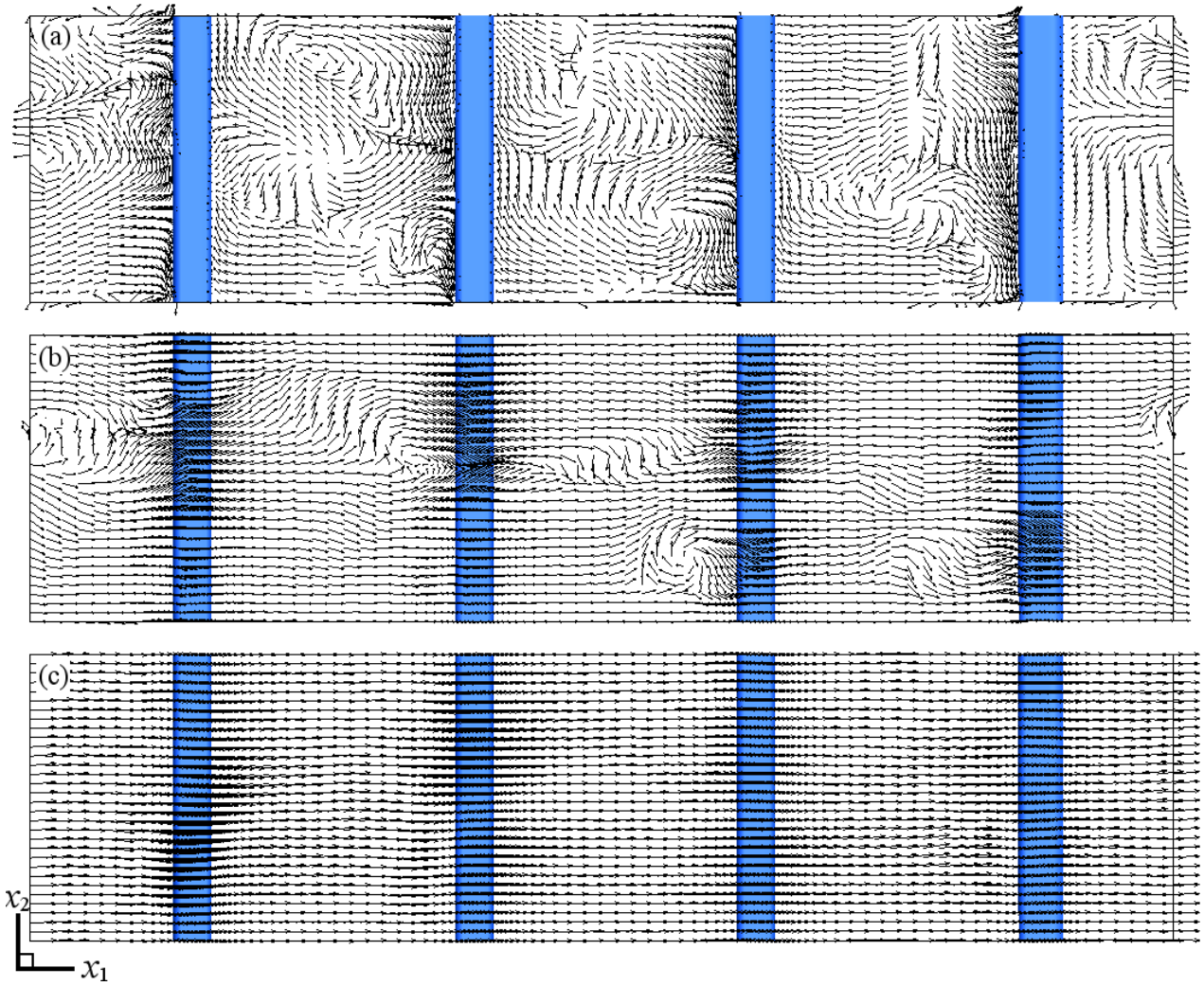

Figure 4.9: Instantaneous velocity vector field for different x_1-x_2 planes across the channel: at (a) 0.5*k*, (b) 1.4*k* and (c) 7*k*, above the ground plane

4.3.2 Proper Orthogonal Decomposition:

4.3.2.1 Spanwise sampling plane

A first step in POD analysis is to determine the fraction of energy contained in each mode and hence identify the more energetic topologies embedded in the turbulent flow. Figure 4.10 displays the energy

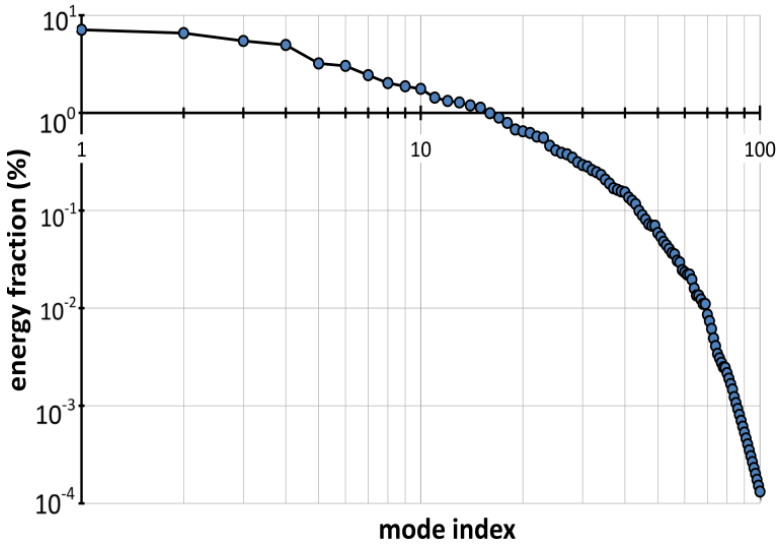

Figure 4.10: POD eigenmodes energy spectrum

spectrum for the POD analysis on a log-log plot; the POD was performed on a spanwise (x_1-x_3) sampling plane. The spectrum, which spans five decades, indicates that consecutive modes contain less and less energy, which is consistent with the basic premise of POD. The first eleven modes capture almost 46 percent of the total fluctuating energy. The mean flow field, which is often referred to as mode 0, carries a large portion of the total energy (almost 44%) and is not included in the spectrum shown in Figure 4.10. The energy contained in each of the first four modes is similar, and there is a noticeable drop in energy content after the fourth mode. This suggests that the fifth mode is of a different nature from the first four. Often it is useful to "bundle" the modes in different groups based on energy content to assess the role of different eigenmodes, although a firm conclusion cannot be drawn from the energy plot alone.

Figure 4.11 displays the streamwise velocity contour plots of the first four POD modes, for a plane in the spanwise direction (x_1-x_3 plane). The overall pattern of each mode can be segregated into three topologies associated with the smooth wall (SW), the roughened wall (RW) and the bulk flow (BF). In Figure 4.11, longitudinal structures can be observed in the proximity of both walls: the RW structures are inclined to the wall. This characteristic is more pronounced in modes 3 and 4, Figures 4.11(c) and 4.11(d), respectively. The BF structures are typically larger and less stretched in the streamwise direction compared to SW and RW structures. For the first two modes, the BF structures are located near the center of the channel, while for modes 3 and 4; they are displaced towards the smooth wall.

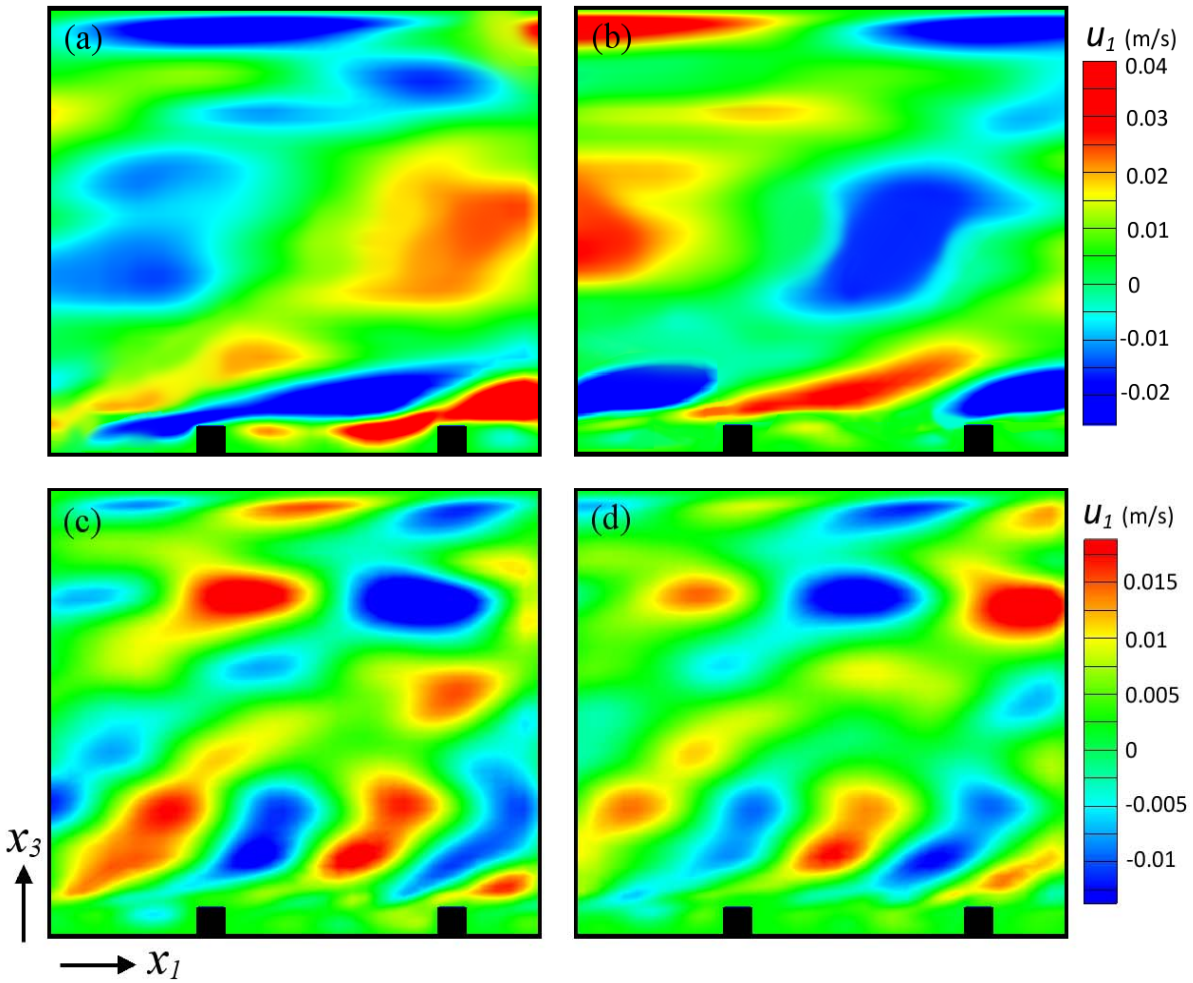

Figure 4.11: First four modes of the ϕ_{u_1} component

All three topologies exhibit traveling wave characteristics with a phase shift relative to each other. The first two modes are dominated by the BF structures, whereas for modes 3 and 4, the RW structures are dominant.

Contours of the first four modes of the wall-normal velocity component are displayed in Figure 4.12. The SW topologies are stretched in the streamwise direction, whereas the RW topologies also extend in the wall normal direction. In the first two modes, the RW and BF topologies merge to form the large dominating structures. For the next two modes, the separate BF structures are absent, and the SW structures are larger than those on the RW. Similar to the case of the streamwise component, a traveling wave characteristic, with a phase shift can be noticed in all four eigenmodes.

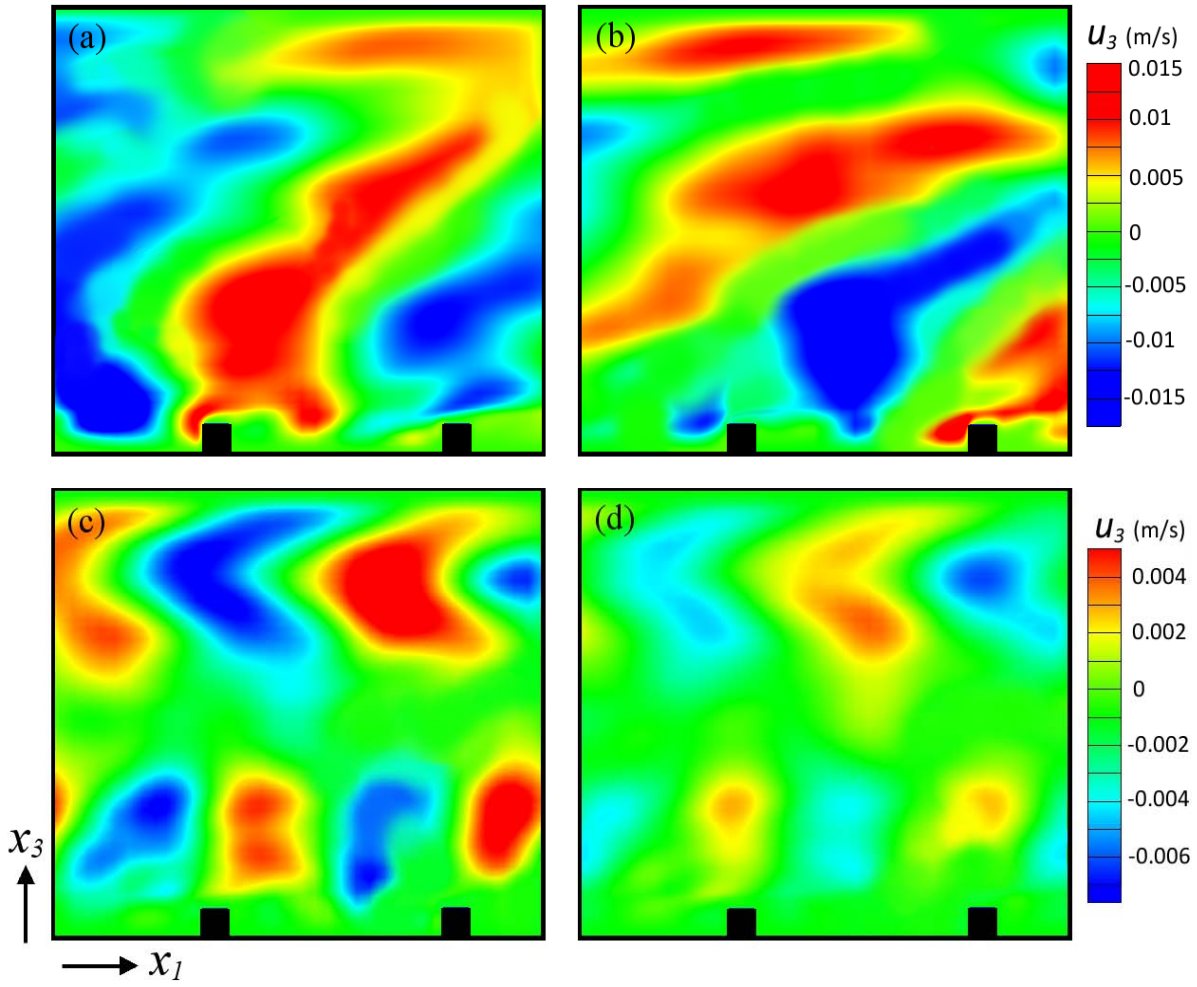

Figure 4.12: first four modes of the ϕ_{u_3} component

Figure 4.13 displays the first four eigenmodes for the spanwise component of the vorticity (ω_2). For Couette flow, the vortex strength of the RW and SW structures is much higher than that of the BF structures: accordingly, in Figure 4.13, the BF structures are very weak and difficult to distinguish. The SW structures are stretched in the streamwise direction, and located very close to the wall. In contrast, the RW structures are somewhat inclined and located just above the rib elements. An interesting feature is the presence of multiple structures near the leading corner of each rib. This feature is most noticeable for the first mode. Overall, the dominant components of the eigenmodes of the spanwise vorticity component are located close the channel walls. This is in contrast to the eigenmodes of the streamwise and wall normal velocity components, which tended to fill the entire channel including the core.

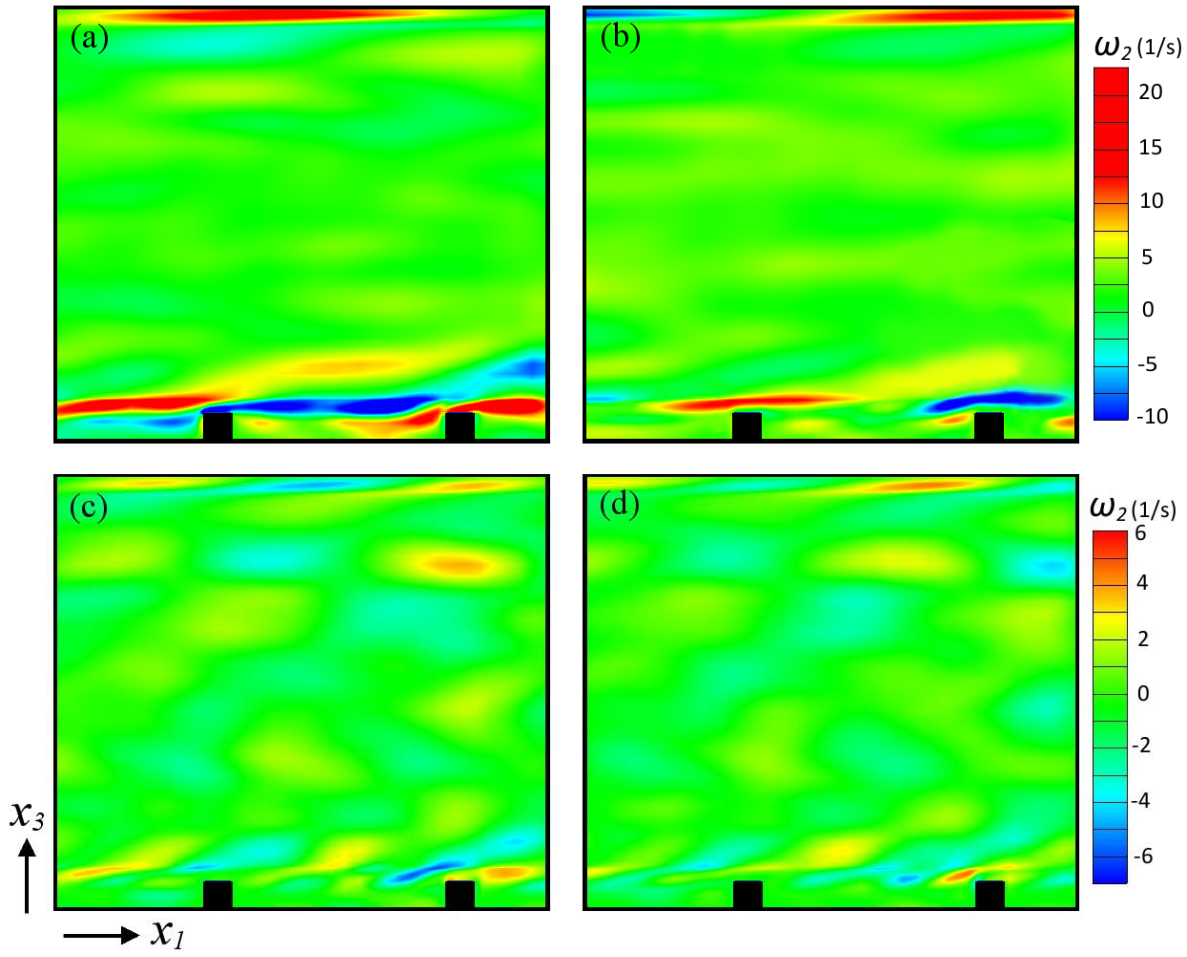

Figure 4.13: first four modes of the ϕ_{ω_2} component

Lastly, in terms of a qualitative analysis of the eigenmodes in the (x_1-x_3) plane, it is useful to make a comparison to the case of a single rib placed on a ground plane (as was done in Chapter 3). Figure 4.14 displays the first two eignenmodes for the streamwise and wall-normal components. Similar to the rib-roughened wall considered in the present study, the topology of the streamwise component is elongated in the x direction (Figures 4.14 (a) and 4.14(b)) but unlike the case of Couette flow, the structures incline downward towards the ground plane. Furthermore, the longitudinal structures are relatively shorter than for the case of Couette flow. For the wall-normal component, the energetic structures are extended in the wall normal (x_3) direction, whereas for the case of Couette flow, they incline in the streamwise direction. A traveling wave characteristic is evident for both geometries.

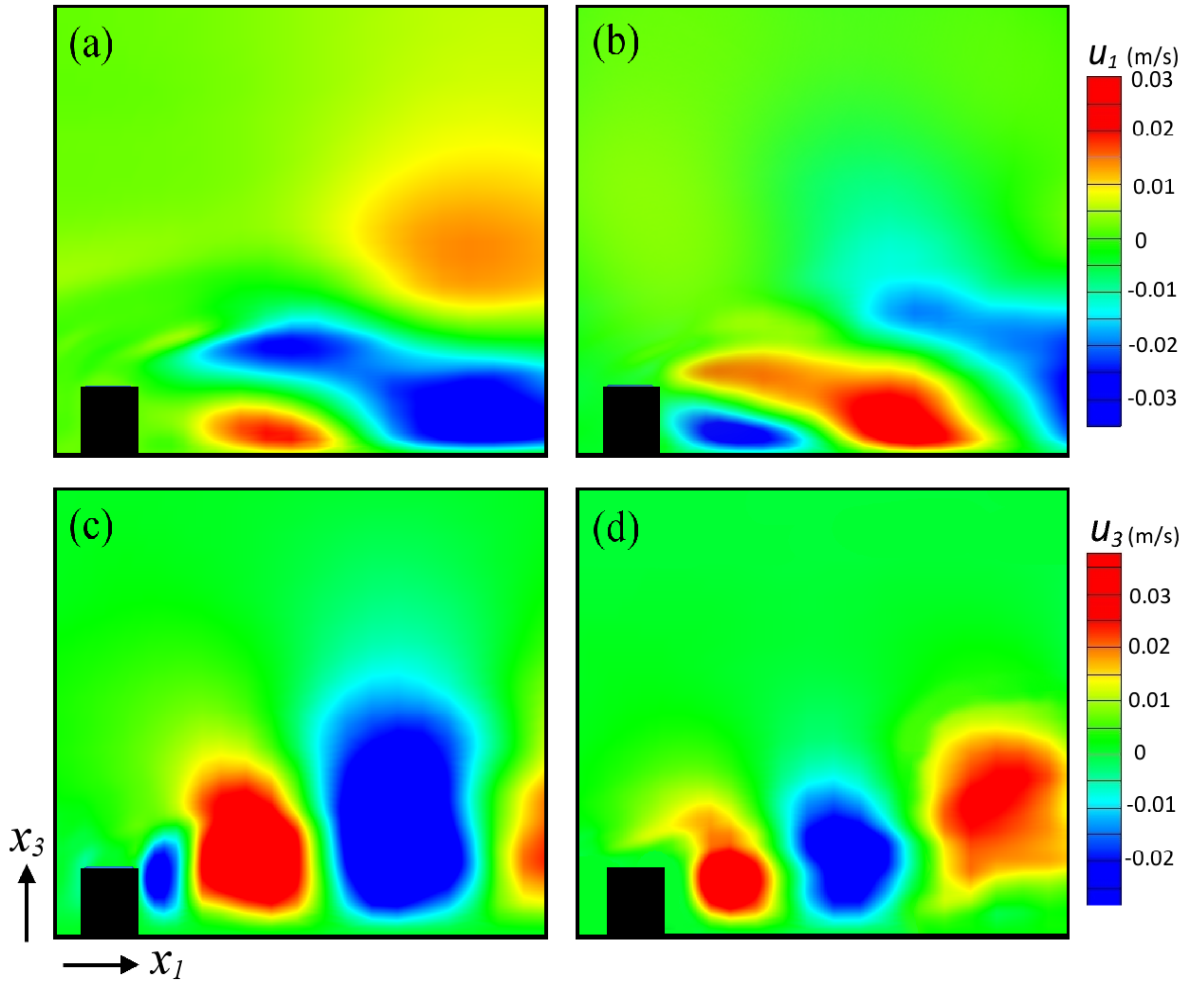

Figure 4.14: POD modes of a single rib on a ground plane: (a) ϕ_{u_1} mode 1, (b) ϕ_{u_1} mode 2, (c) ϕ_{u_3} mode 1 and (d) ϕ_{u_3} mode 2

4.3.2.2 Streamwise sampling plane

As mentioned previously, two-dimensional velocity fields were sampled using the POD on planes with different orientations, i.e. perpendicular to the ribs and to the flow direction. This section will consider the energetic structures in the streamwise (x_2-x_3) plane or cross-section of the flow. To begin, the ensemble averaged or mode 0 field is considered. A remarkable characteristic of turbulent Couette flow as noted by some previous authors (e.g. [15, 32]) is a swirling motion with its axis aligned in the streamwise direction. This secondary flow pattern in the ensemble averaged field is successfully captured in this simulation as displayed in Figure 4.15. The secondary flow consists of two counter-rotating vortical structures which move the fluid towards the smooth wall in the center of the channel and then towards the rough wall near the side planes.

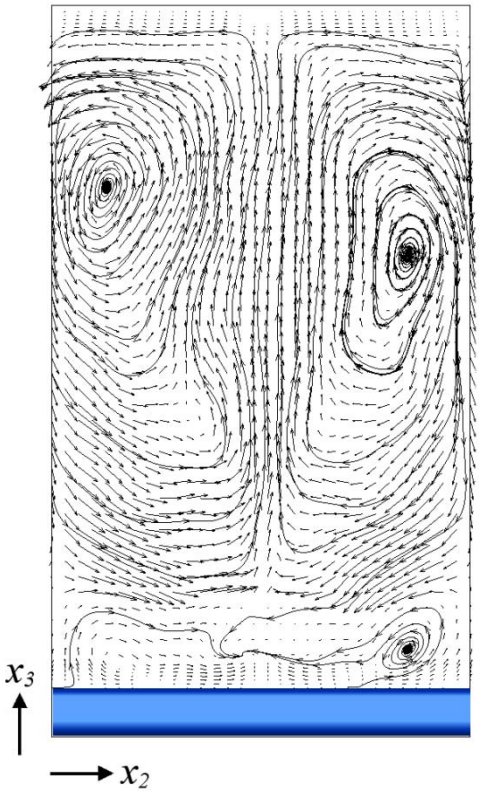

Figure 4.15: Ensemble averaged motions in a streamwise plane

The energy spectrum obtained from the POD analysis of the two-dimensional velocity field on the cross-stream plane or (x_2-x_3) plane is plotted in Figure 4.16. The energy curve obtained from the spanwise plane or (x_1-x_3) plane is also shown for comparison. Note that the lower order modes for the (x_2-x_3) plane contain more energy than those for the (x_1-x_3) plane; however, for higher order modes, this phenomenon is reversed.

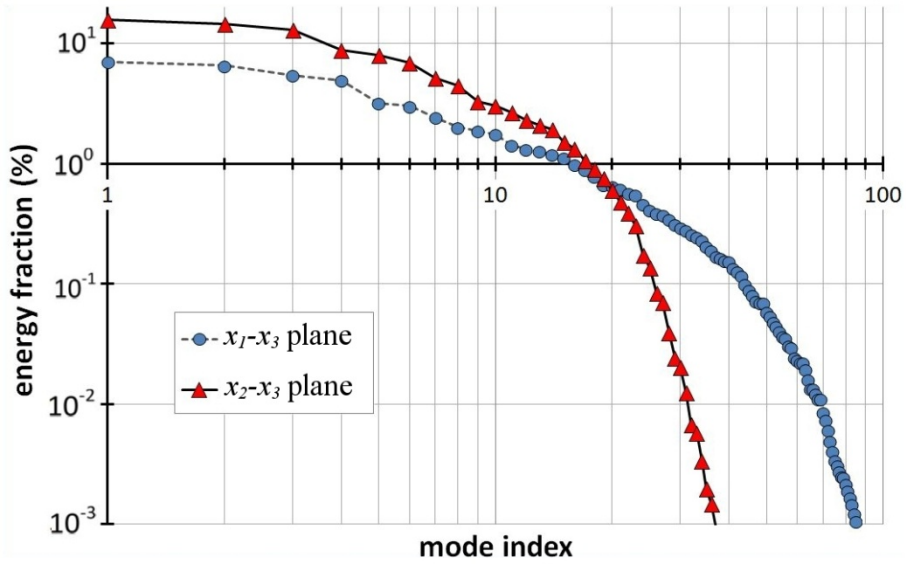

Figure 4.16 Energy spectrums from POD in two planes

Figure 4.17 shows the velocity vector plots for the first four POD modes collected on a streamwise (x_2-x_3) plane located between two ribs. The first mode is similar to the secondary flow pattern, i.e. it represents a swirling motion which is aligned in streamwise direction. For the second mode, similar swirling roll cells can be detected, however, compared with the first mode, the rolls are displaced to align with the center and sides of the domain. The dimensions of these roll cells are a function of the width of the channel for the boundary condition imposed, i.e. periodic in the spanwise direction. Compared with previous studies of plane Couette flow with two smooth walls, e.g. [15] and [17], these streamwise cells are displaced towards the smooth wall as a result of the rib-roughness. For the third mode, two counter-rotating cells are evident in the lower region of the channel above the rough wall. The primary cells swirl

in the same direction as those contained by the first mode. When the tertiary motions are added to the other two modes, they will change the recirculation patterns in the lower half of the channel. In addition

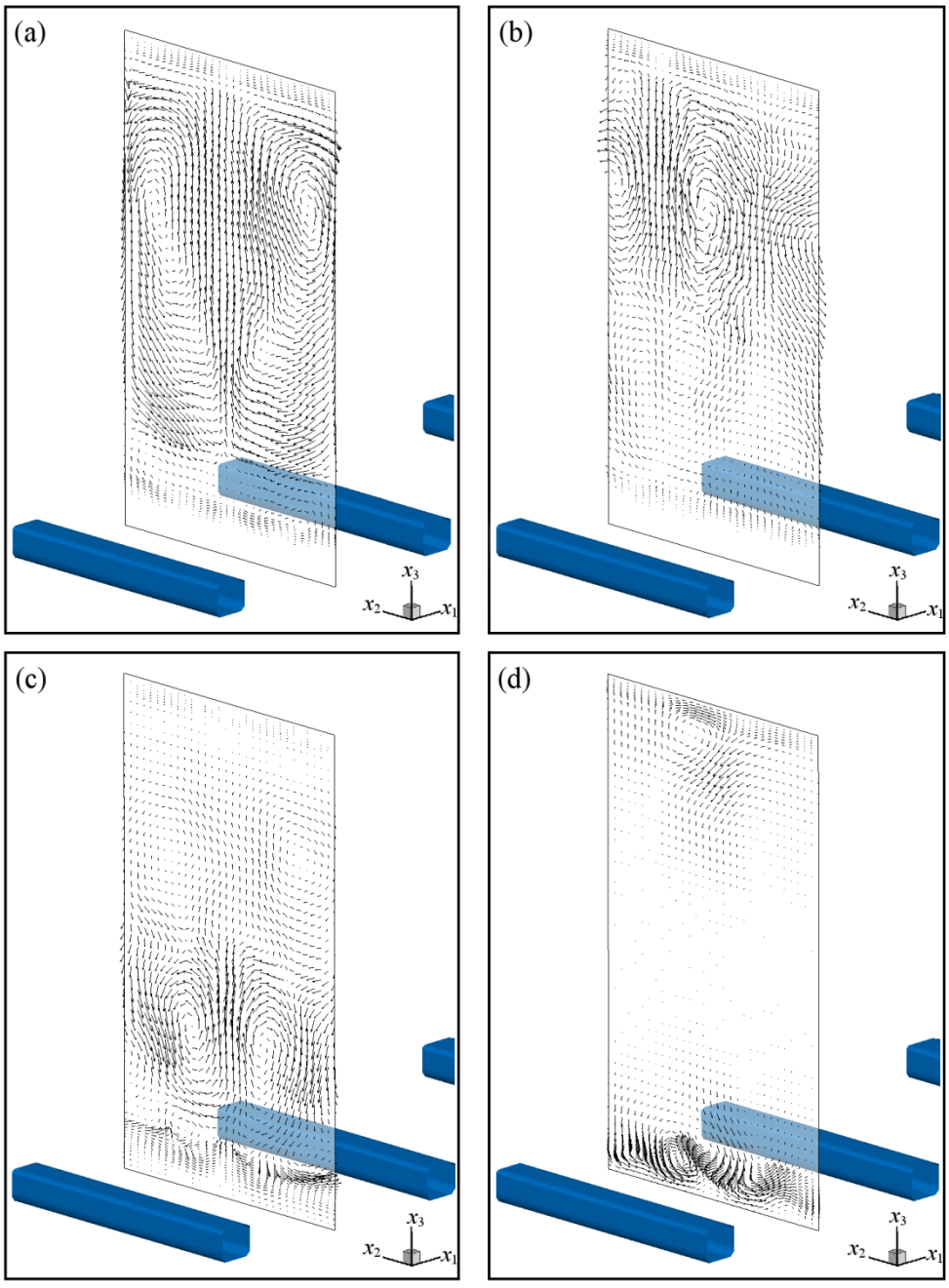

Figure 4.17: Velocity vectors for the first four eigenmodes in the x_2-x_3 plane

to the larger swirls observed for mode three, some smaller yet still energetic motions begin to appear near the crests of the ribs. This suggests that the first three energetic modes are dominated by the outer flow, with roughness only beginning to interact with the core flow in the third mode.

The topology of the fourth mode is visibly different than the first three, i.e. it is no longer dominated by swirling cells in the channel core. Instead, some vortical motions in the wake of the upstream rib can be seen. Further to the previous comment on the third mode, the fourth mode is more associated with the transverse flow patterns located in the gaps between the ribs, rather than with the Couette flow itself. As such, mode four is fundamentally different in nature than the first three. This conclusion is also supported by the energy plot given in Figure 4.16, which shows that the energy drops noticeably after the third mode. Another topology specific to this eigenmode is the emergence of vortical motions close to the smooth wall. One would expect the higher-order modes to introduce additional vortical motions close to the upper and lower walls.

It should be noted that visualizing the velocity vector fields was found to be helpful only for the (x_2-x_3) plane. This is simply because in the (x_2-x_3) plane, the u_2 and u_3 components of velocity were considered. For the (x_1-x_3) plane, where the u_1 and u_3 components were considered, the vectors become very small close to the bottom surface which then makes the plots less helpful for detecting the dominant structures.

The contour plots of the wall-normal velocity, spanwise velocity and streamwise vorticity (ω_1) for the first four modes in a (x_2-x_3) plane are displayed in Figures 4.18, 4.19 and 4.20, respectively. These contour plots help to identify the energetic flow structures in the core of the flow. Analysis of these figures supports the earlier observation that the first two modes are mainly dominated by the swirling motions in the centre region of the channel. The figures also illustrate how the swirling cells are displaced upwards by the roughened wall. Finally, they also reveal that for the higher-order modes the structures begin to accumulate near the walls, and likely relate to the turbulence generation.

4.3.2.3 Analysis of the life cycle of the eigenmodes

The eigenmodes presented thus far are basically two-dimensional spatial fields. However, one can use them to reproduce the reference turbulent flow, which is a time-dependent field. Therefore, it would be of

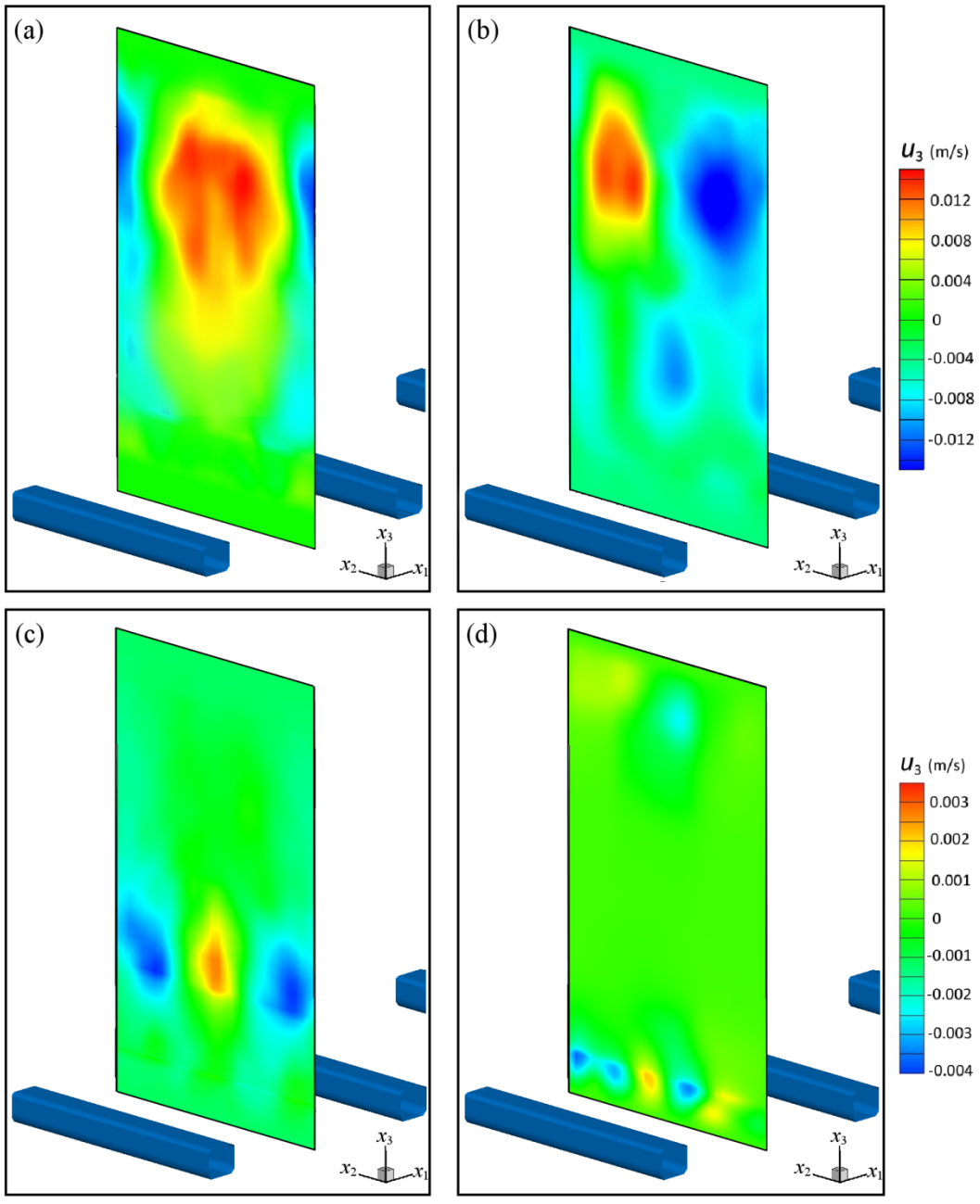

Figure 4.18: ϕ_{u_3} component of the first four modes

interest to investigate how the contributions of these spatial fields are modulated in time to generate a "realistic" flow field. This is where the temporal coefficients, $a_n(t)$, come into play. These coefficients are obtained from the eigenvalue problem and represent the amplitude of the eigenmodes in the linear decomposition of the instantaneous fluctuation field. The variation of the temporal coefficients of the first

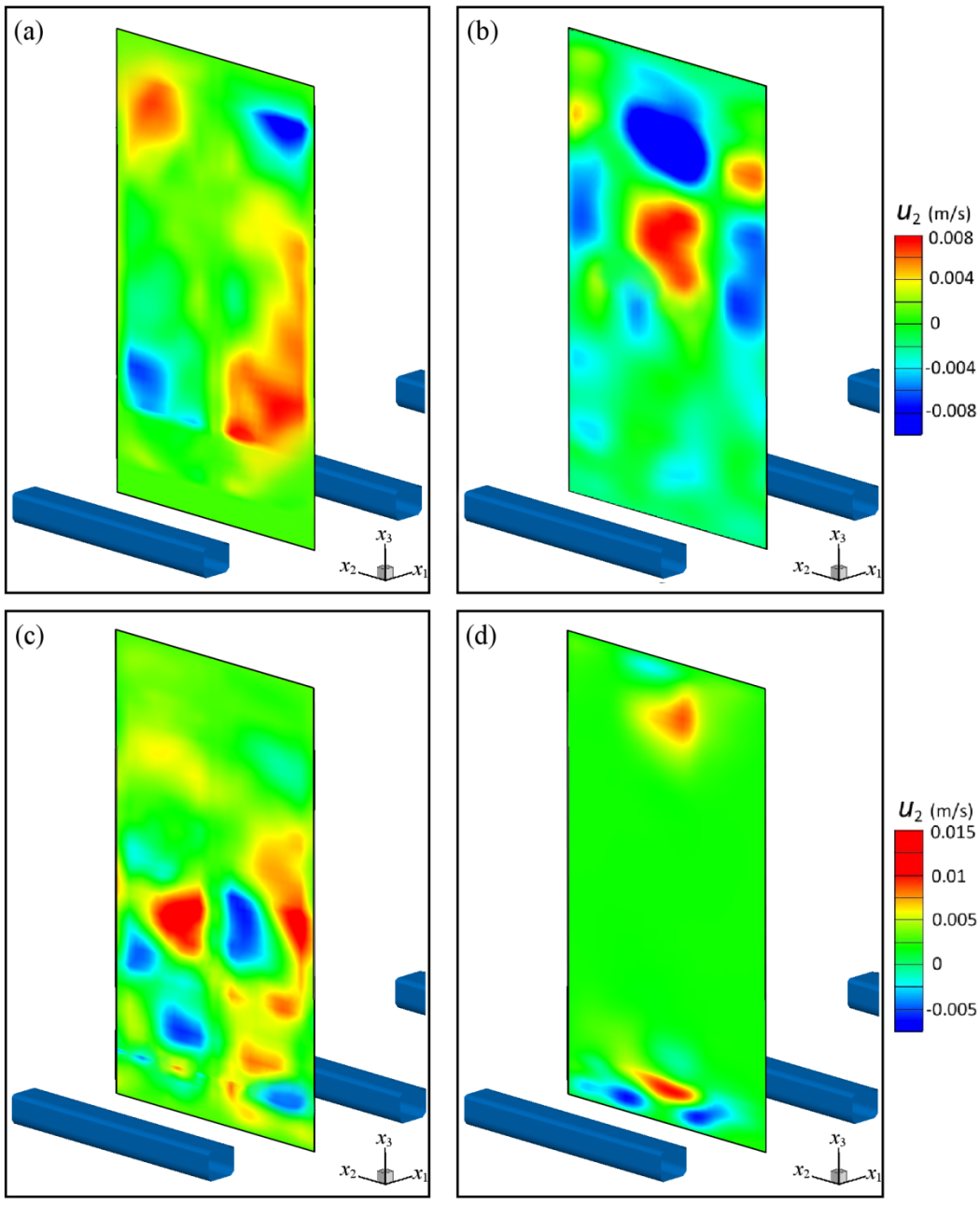

Figure 4.19: ϕ_{u_2} component of the first four modes

four eigenmodes over 24 non-dimensional time units is plotted in Figure 4.21. As noted previously, the velocity of the top wall and the spacing between the elements is used to non-dimesionalize the time ($T_w = w/U_w$). Given that the four ribs cover the streamwise extent of the solution domain, 24 dimensionless time units is equivalent traversing the channel six times. As expected, the magnitude of

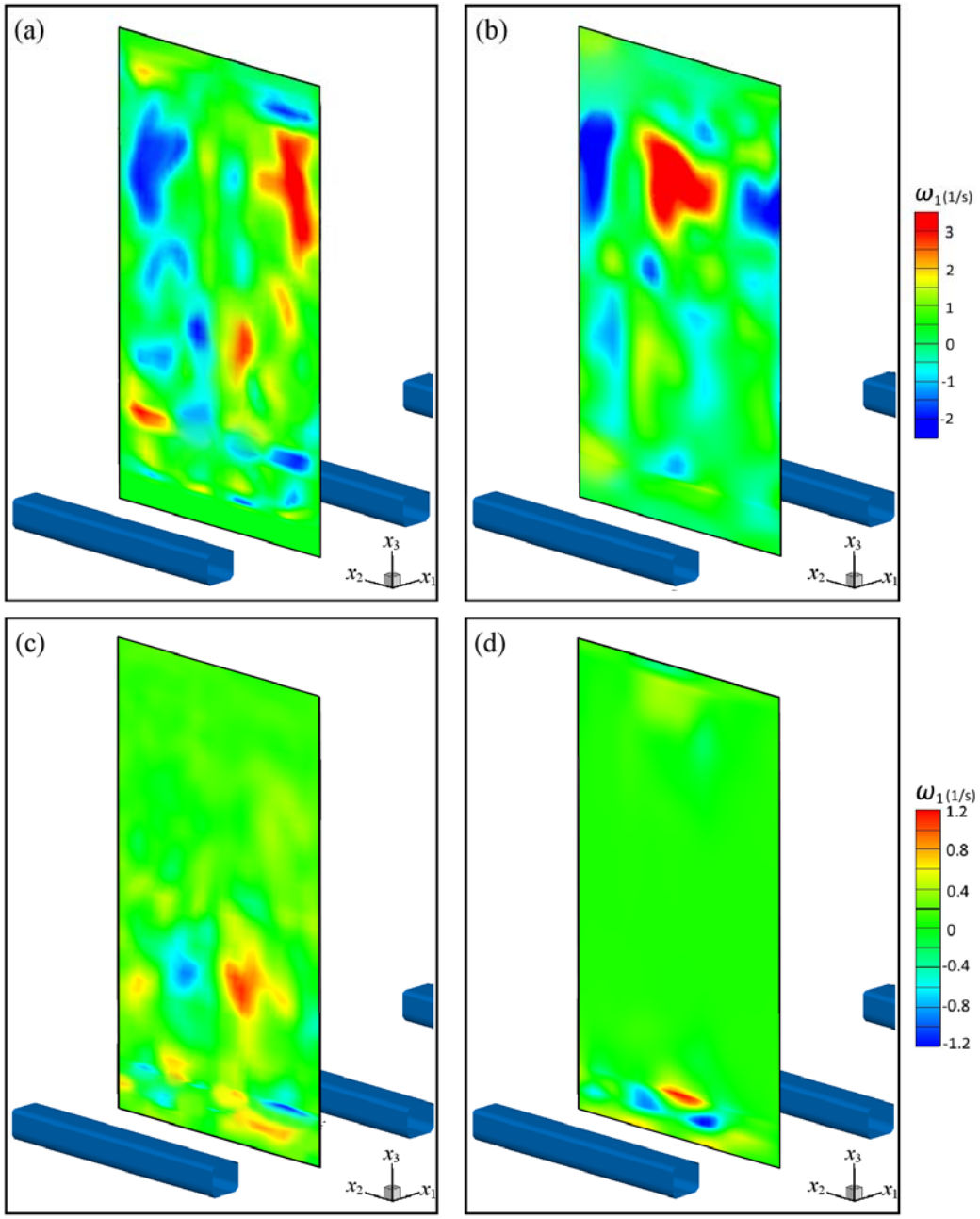

Figure 4.20: ϕ_{ω_1} component of the first four modes

a_1 is typically larger than the other modes, and the magnitude of each mode decreases as the order of the mode increases. Unlike the case of vortex shedding flow, a significant sinusoidal behavior is not evident in Figure 4.21. However, viewing the variation of $a_n(t)$ over a much longer time frame, a quasi-periodic behavior with a large time period can be detected, as shown in Figure 4.22. This approximately periodic dynamic has been visualized in previous studies, e.g. [17], [28] and [29]. These time traces indicate how energetic rolls are born, grow and decay as part of the life cycle of a realistic turbulent flow

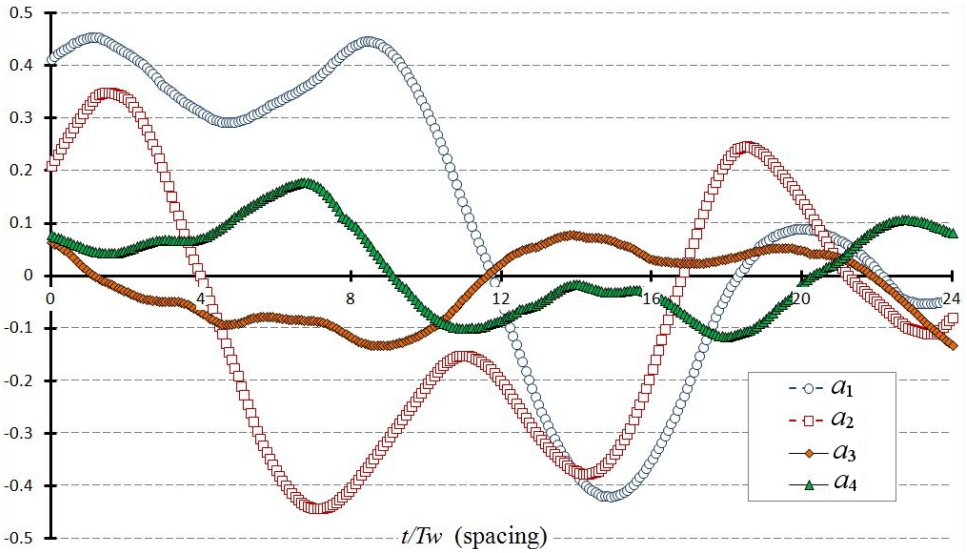

Figure 4.21: Time variation of the temporal coefficients for the first four modes

By individually analyzing each of the data series in Figure 4.22, a remarkable feature is observed for each curve: each curve can be decomposed into a primary trend curve and fluctuations about the trend. The trend curves exhibit a nearly periodic trajectory, and the time periods are all of the same order of magnitude but not exactly equal, as shown in Figure 4.23 (a) for the first two modes. The curves for the fluctuation component have much higher frequencies (or smaller periods), which increase with the of the mode index (see Figure 4.23 (b)). For comparison, both Figure 4.23 (a) and 4.23 (b) include the original time variation curves in the background.

The quasi-periodic behavior might be associated with the numerical boundary condition imposed on the streamwise boundaries of the computational domain, and as such not be observed in experimental

studies. Moreover, the trends outlined above can be used to specify the location of each energetic structure in the domain. The fluctuation curves on the other hand likely represent the turbulent motions. For higher modes, the frequency of these oscillations would systematically increase. Since the small-scale motions are more irregular and less energetic, the plots for higher modes would be expected to look like a noisy weak signal. Conversely, the frequency of the trend curves stays in the same approximate range, even for higher modes.

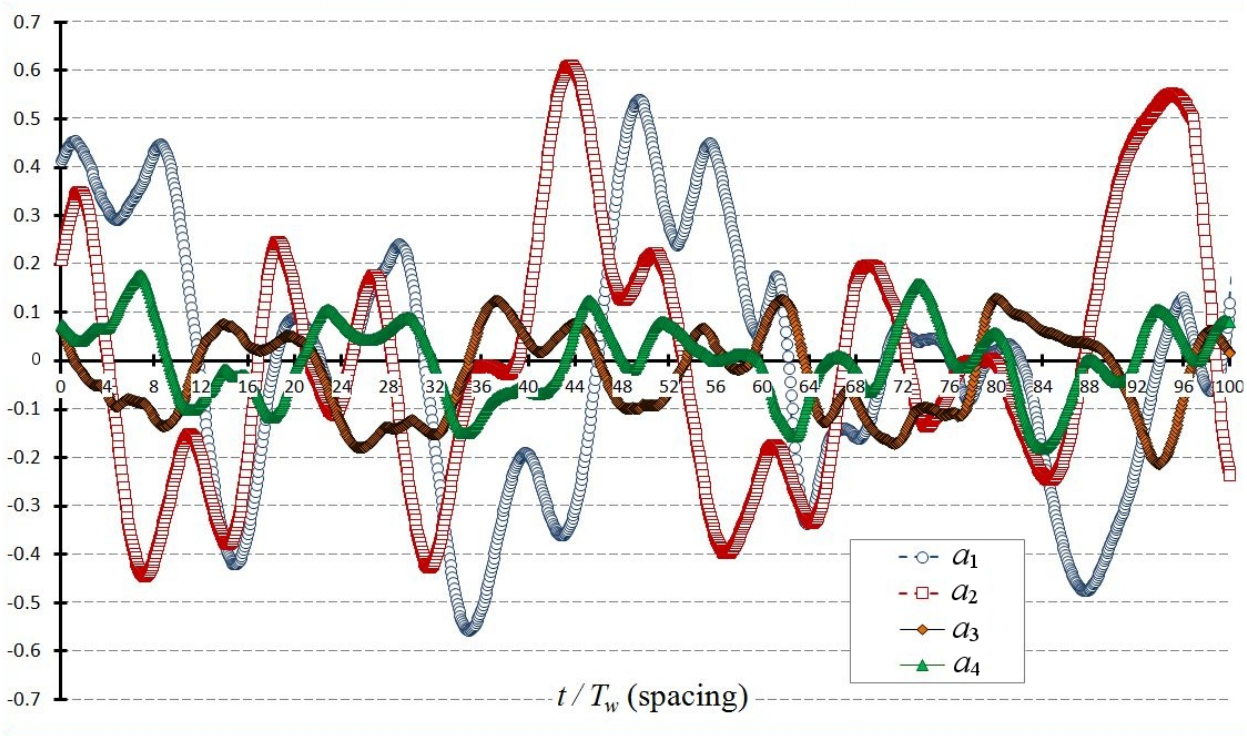

Figure 4.22: Time history of the first four modes over 100 non-dimensional time units

4.4 Conclusion

In this study, LES of turbulent Couette flow with rib-roughness elements on one wall was performed. Selected characteristics of the mean and fluctuating velocity fields were compared with previous measurements and simulations of plane Couette and rib-roughened Poiseuille flows to verify the results.

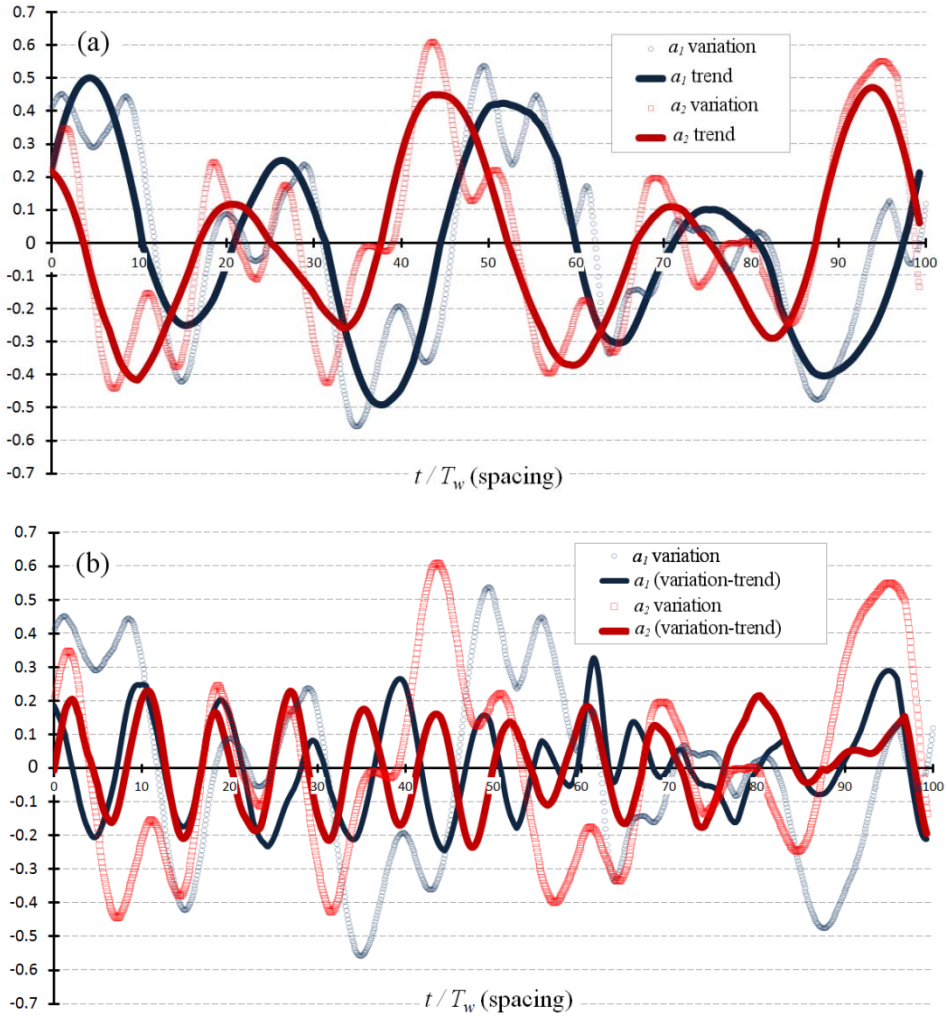

Figure 4.23: Decomposition of $a_n(t)$ plots: (a) trend curves, (b) oscillations

The LES results showed that roughness introduces an asymmetry in the velocity field. The dominant streamwise and spanwise structures of the flow were investigated using POD, and a physical interpretation of each structure was presented. Typically, the roughened surface displaces the streamwise swirling motions into the core region. Finally, the life cycle of the coherent structures was analyzed based on the temporal coefficients of the POD analysis. The results of the temporal analysis were shown to provide novel and significant insight into the flow structure. The two-dimensional roughness elements were shown to generate highly three-dimensional structures. This three-dimensionality suggests that the next step would be a thorough study of the three-dimensional flow structures using POD.

References

[1] K. Hanjalic and B. E. Launder,"Fully developed asymmetric flow in a plane channel." *Journal of Fluid Mechanics*, 51: 301–335, 1972.

[2] E. M. Aydin and H. J. Leutheusser, "Plane-Couette flow between smooth and rough walls." *Experiments in Fluids*, 11: 302-312, 1991.

[3] Y. Miyake, K. Tsujimoto and Y. Agata, "A DNS of a turbulent flow in a rough-wall channel using roughness elements model." *JSME International Journal*, B43(8): 233–242, 2000.

[4] T. Ikeda and P. A. Durbin, *Direct simulations of a rough-wall channel flow*. Report TF-81, Department of Mechanical Engineering, Stanford University, 2002.

[5] J. Cui, C. P. Virendra and L. Ching-Long, "Large-eddy simulation of turbulent flow in a channel with rib roughness." *International Journal of Heat and Fluid Flow*, 24: 372–388, 2003.

[6] S. Leonardi, P. Orlandi, R. J. Smalley, L. Djenidi, and R. A. Antonia, "Direct numerical simulation of turbulent channel flow with transverse square bars on one wall", *Journal of Fluid Mechanics*, 491: 229–238, 2003.

[7] S. Leonardi, P. Orlandi, L. Djenidi and R. A. Antonia, "Structure of turbulent channel flow with square bars on one wall." *International Journal of Heat and Fluid Flow*, 25: 384–392, 2004.

[8] Y. Nagano, H. Hattori and T. Houra, "DNS of velocity and thermal fields in turbulent channel flow with transverse-rib roughness." *International Journal of Heat and Fluid Flow*, 25: 393–403, 2004.

[9] J. Jimenez, "Turbulent flows over rough walls." *Annual Review of Fluid Mechanics*, 36: 173-196, 2004.

[10] P.-Å. Krogstad, H. I. Andersson, O. M. Bakken and A. Ashrafian, "An experimental and numerical study of channel flow with rough walls", *Journal of Fluid Mechanics*, 530: 327–352, 2005.

[11] O. M. Bakken, P.-Å. Krogstad, A. Ashrafian and H. I. Andersson, "Reynolds number effects in the outer layer of the turbulent flow in a channel with rough walls." *Physics of Fluids*, 17: 065101, 2005.

[12] A. Ashrafian and H. I. Andersson, "The structure of turbulence in a rod-roughened channel" *International Journal of Heat and Fluid Flow*, 27: 65–79, 2006.

[13] P. Orlandi, S. Leonardi and R. A. Antonia, "Turbulent channel flow with either transverse or longitudinal roughness elements on one wall" *Journal of Fluid Mechanics*, 561: 279–305, 2006.

[14] P. Burattini, S. Leonardi, P. Orlandi and A. Antonia, "Comparison between experiments and direct numerical simulations in a channel flow with roughness on one wall" *Journal of Fluid Mechanics*, 600: 403–426, 2008.

[15] D. V. Papavassiliou and T. J. Hanrattym, "Interpretation of large-scale structures observed in a turbulent plane Couette flow" *International Journal of Heat and Fluid Flow*, 18: 55-69, 1997.

[16] B-C. Wang and D. J. Bergstrom, "A dynamic nonlinear subgrid-scale stress model." *Physics of Fluids*, 17: 035109, 2005.

[17] J. Moehlis, T. R. Smith, P. Holmes and H. Faisst, "Models for turbulent plane Couette flow using the Proper Orthogonal Decomposition.", *Physics of Fluids*, 14: 2492-2507, 2002.

[18] T. R. Smith, J. Moehlis and P. Holmes, "Low-dimensional models for turbulent plane Couette flow in a minimal flow unit", *Journal of Fluid Mechanics*, 538: 71–110, 2005.

[19] T. Tsukahara, K. Iwamoto and H. Kawamura, *POD analysis of large-scale structures through DNS of turbulent plane Couette flow*. Advances in Turbulence XI, Proceedings of the 11th EUROMECH Turbulence Conference, Porto, Portugal, June 25-28, 2007.

[20] L. Sirovich, "Turbulence and the dynamics of coherent structures." Parts I, II and III. *Quarterly of Applied Mathematics*, 45: 561-571 and 573-590, 1987.

[21] M. Germano, U. Piomelli, P. Moin and W. H. Cabot, "A dynamic subgrid-scale eddy viscosity model." *Physics of Fluids*, A3: 1760-1765, 1991.

[22] D. K. Lilly, "A proposed modification of the Germano subgrid-scale closure method," *Physics of Fluids A*, 4: 633–635, 1992.

[23] Th. Von Karman, "The analogy between fluid friction and heat transfer", *Transactions of the American Society of Mechanical Engineers,* 61: 705–710, 1939.

[24] K. Bech, N. Tillmark, P. H. Alfredsson and H. I. Andersson, "An investigation of turbulent plane Couette flow at low Reynolds numbers." *Journal of Fluid Mechanics*, 286: 291-325, 1995.

[25] P.-Å. Krogstad and R. A. Antonia, "Surface roughness effects in turbulent boundary layers." *Experiments in Fluids*, 27: 450-460, 1999.

[26] N. Brunetière and B. Tournerie, "Study of Hydrostatic Mechanical Face Seals Operating in a Turbulent Rough Flow Regime." *Journal of Tribology*, 131: 032202, 2009.

[27] C. K. Liu, S. J. Kline and J. P. Johnston, *An experimental study of turbulent boundary layers on rough walls*. Report MD-15, Department of Mechanical Engineering, Stanford University, 1966.

[28] T. R. Smith, J. Moehlis and P. Holmes, "Low-dimensional models for turbulent plane Couette flow in a minimal flow unit." *Journal of Fluid Mechanics*, 538: 71–110, 2005.

[29] T. R. Smith, J. Moehlis and P. Holmes, "Low-Dimensional Modeling of Turbulence Using the Proper Orthogonal Decomposition: A Tutorial.", *Nonlinear Dynamics*, 41: 275–307, 2005.

[30] A. J. Grass, "Structural Features of Turbulent Flow over Smooth and Rough Boundaries", *Journal of Fluid Mechanics*, 50(2): 233-255, 1971.

[31] P. Orlandi and S. Leonardi, "DNS of turbulent channel flows with two- and three-dimensional roughness." *Journal of Turbulence*, 7(53): 1-22, 2006.

[32] M. J. Lee and J. Kim, *The structure of turbulence in a simulated plane Couette flow,* Proceeding of the 8th Symposium on Turbulent Shear Flows, Munich, Germany, September 9-11, 1991.

[33] M. F. Tachie, D. J. Bergstrom and R. Balachandar, "Rough wall turbulent boundary layers in shallow open channel flow." *Journal of Fluids Engineering*, 122: 533–541, 2000.

[34] E. M. Aydin and H. J. Leutheusser, *Experimental investigation of turbulent plane Couette flow*, ASME Forum on Turbulent Flows FED, Cincinnati, Ohio, June 14-17, 1987.

[35] H. I. Andersson, K. H. Bech and R. Kristoffersen, "On diffusion of turbulent kinetic energy in Plane Couette flow", *Proceedings of the Royal Society: Mathematical and Physical Sciences*, 438: 477-484, 1992.

Chapter 5

Concluding Remarks

5.1 Thesis Summary

The main target of this research was to study turbulent flows over rough walls and the objective was to identify the structures associated with the roughness. For the sake of validating the LES and POD algorithm, a simple geometry (an infinite square cylinder) was selected where a number of earlier experimental and numerical studies were available for comparison. Then, the effect of the wall was analysed by implementing a solid surface in proximity of the infinite cylinder. Finally by distributing those tested prismatic obstacles in the streamwise direction and changing the boundary conditions, a turbulent Couette flow with one roughened wall was modelled. For each study case, the main objective was to detect and characterize the dominant flow structures embedded in the global flow field.

For all the simulations, an existing in-house LES code was adopted and initial and boundary conditions along with grid resolution and time-steps were modified to apply it to multiple different geometries. The author also performed extensive post-processing, which included development of the POD code in MATLAB. In addition, three independent topics were linked and integrated into a comprehensive study of turbulent wake structures.

5.2 Conclusions and Contributions

For the first study case, an infinite square cylinder in a free stream, the Reynolds number based on the approach-flow velocity and cylinder edge-length ($U_\infty D/\nu$) was set to $Re = 500$, where a number of high resolution numerical and experimental results are available for comparison. A time series of the spanwise velocity and vorticity component from probes located in the wake behind the cylinder clearly exhibited irregularly changing amplitude with zero mean and indicated vortex shedding frequencies.

By performing a fast Fourier transform on these signals, the dominant shedding frequency was calculated and shown that is in a reasonable agreement with the results of other experimental and computational studies, despite using a relatively courser mesh and accordingly, lesser computational time and cost.

By looking into a close-up view of the time-averaged streamlines in the vicinity of the rear side of the cylinder, and distribution of some flow parameters (such as mean streamwise velocity and fluctuating energy components) along the centerline of the wake, it was shown that by proper local refinement of the grid, one can successfully resolve the turbulent wake flow with a reasonable accuracy, with a less computational cost.

After validation of the LES code, the POD algorithm was examined by first scanning the energy spectrum. A relatively steep inclination of the plot indicated that the total kinetic energy of the flow was found to be well captured by only a small number of eigenmodes. From the energy spectrum, it was concluded that each eigenmode represents a particular flow characteristic embedded in the turbulent wake and eigenmodes with analogous characteristics have analogous energies. Another contribution of this study case was to perform a qualitative analysis of the coherent structures generated by a prismatic bluff body and study their interaction, with large-scale structures in the developed outer flow. Dominant flow structures were classified as vortex shedding, bulk flow adjustment, higher harmonic fluctuations and instability rolls.

A contribution of this chapter was to examine the temporal behavior of the eigenmodes and from that, present a new manner to develop physical interpretations of the eigenmodes and even obtain some global flow parameters by analyzing life-cycles of each eigenmode. It was observed that the life-cycles of the paired modes are periodic, with nearly similar frequency, but a phase shift. In contrast, the stand-alone modes did not have a periodic variation or comparable pattern. At the end, the ability of POD in reconstructing the turbulent structure was examined. It was verified that the turbulent flow field can be approximated by a linear combination of the mean flow and a finite number of spatial modes. It was verified that, the cut-off of this linear series, and accordingly, the desired accuracy of this approximation can be defined by the number of dominant modes selected to reconstruct the turbulent flow.

In the second study case, for flow arrangement, the free stream velocity and the cylinder side length were used to define the Reynolds number ($Re = U_\infty D/\nu$). Similar to the first case, a Reynolds number of $Re = 500$ was adopted. The approach flow included a turbulent boundary layer with a thickness of $\delta/D = 0.2$. The simulation results of the second study case showed that a nearby wall has a minimal impact on the vortex shedding frequency, but significantly changes the periodic forces and consequently, the value of the mean drag and lift coefficients. As a result, the mean drag coefficient increases as the gap ratio is reduced, while the lift coefficient decreases. From the time-averaged velocity profiles in the gap between the lower face of cylinder and the wall, the region of reverse flow was observed, and it was concluded that the proportional size of this region is independent of the gap size. From the spanwise velocity profile for the same region, it was observed that the spanwise velocity is more dependent on the streamwise location: mainly downward close to the leading-edge of the cylinder, but turning upward close to the exit of the gap. It was concluded that the upward flow at the trailing-edge is due to the interaction between the wake vortices and the vortex attached to the wall.

A POD study of this flow reveals that the rate of decay of the eigenvalues decreases as the wall approaches the bluff body, which means the influence of the wall on generating the energetic structures is more significant for smaller gap spaces. In addition, at some point the pairwise decay disappears and the

physical interpretation of the dominant modes changes. An interpretation of the characteristic of each dominant mode versus the energy contained is developed, with the aim of detecting a meaningful linkage between the energy spectrum and the mode patterns.

From visualization of the coherent structures (in terms of streamwise velocity, wall-normal velocity and spanwise vorticity) for each gap height, it was concluded that for larger gaps, while the structures are leaning away from the wall, the travelling wave characteristic still exists. On the contrary for smaller gaps (and finally no gap case), the travelling wave and ultimately, the shedding fades away. Lastly, it was concluded that for the smaller gap spaces, energetic structures originated by the wall are rooted in lower index modes. In comparison to the existing literature on this topic, this study focused on the more spatial characteristics of the wake in proximity to the wall. More distinct structures are visualized and characterised and linked to the energy spectrum. Another improvement is to make a comparison with flow over a rib shaped obstacle which is the linkage to the study of flow over roughened surfaces.

The last study case tried to recap the contributions of the first two studies, in a single independent study and introduce a new perspective to analyse turbulent flow using POD. From the mean velocity distribution profile across the channel, it was concluded that the rib roughness on the bottom wall can have a significant influence on the velocity profile near the top wall. Another contribution of this simulation was to measure the characteristic roughness shift due to the enhanced wall shear stress created by the ribs from the velocity profiles in universal wall coordinates. The value of the roughness shift indicated that the flow is in the transitional roughness regime.

From the resolved-scale streamwise velocity fluctuation along the wall normal direction plots (for both walls) the peak value was obtained and it was shown that as a result of a roughened wall the peak value drops and the location of peak is shifted slightly away from the roughened wall, which is another outcome of this study work. It was also concluded that the resolved-scale streamwise velocity fluctuation on the smooth wall does not appear to be strongly affected by the roughness on the opposite side of the channel. Another valuable outcome of this simulation is the length of the recirculation cell and

reattachment length, which is shown to be slightly smaller than similar quantities in a pressure-driven channel.

From POD analysis of this flow, the energetic dynamics of the flow were obtained and characterized in two different two-dimensional planes. The energy spectrum in a log-log plot showed a significant drop in energy content after the fourth mode on the (x_1-x_3) plane and drop after the third mode on the (x_2-x_3) plane. It was also concluded that the lower order modes for the (x_2-x_3) plane contain more energy than those for the (x_1-x_3) plane. The influence of the roughened wall on formation of the energetic velocity (streamwise, spanwise and wall normal) and vortical structures was visualized on both planes. From coherent POD modes on a plane in the spanwise direction (x_1-x_3), it was learned that the energetic bulk flow structures have been pushed towards the smooth wall, especially for higher modes. It was also concluded that the first two modes are dominated by the bulk flow structures, whereas for modes 3 and 4, the structures associated with the rough wall are dominant.

By visualizing energetic structures in the streamwise (x_2-x_3) plane or cross-section of the flow, the secondary flow consists of two counter-rotating vortical structures which are a well-recognized characteristic of turbulent Couette flow. It was shown that counter-rotating cells start to appear (as tertiary swirling motions) above the ribs for the higher modes. In addition, some smaller yet still energetic motions were observed near the crests of the ribs. It was concluded that the first three energetic modes are dominated by the outer flow, with roughness only beginning to interact with the core flow in the third mode. In a different manner the fourth mode is more associated with the transverse flow patterns located in the gaps between the ribs, rather than with the Couette flow itself.

At the end, a comprehensive analysis of the time history of the eigenvectors for the first four modes was performed. By individually analyzing each of the traces, it was observed that each curve can be decomposed into a primary trend curve and fluctuations about the trend, which is an important contribution of this study. Physical explanations of the trend curves and oscillations were developed and

an interesting application of POD was introduced in terms of filtering out unrealistic behaviors caused by numerical boundary conditions.

To sum up, this research demonstrates advantages of POD to study turbulent flows in a more practical and efficient way: focusing on the stronger topologies and detecting their life-cycle, instead of looking at the flow as a whole. This approach can be very advantageous, for example, for flow control purposes. In addition some interesting applications of POD were introduced, from an angle never looked at before.

5.3 Recommendations for Future Extension

One important undertaking as an extension to this study is to examine more geometries and configurations. A finite square cylinder mounted on a ground plane would be an interesting subject to look into. Preparatory work was done as a side work in terms of literature review and some preliminary (yet interesting) POD results were obtained. That study can be continued on an appropriate time frame in the future.

Another configuration to look into is the cavity flow, which is worth considering from its practical point of view. Usually, when the spacing between two prismatic obstacles is relatively small, local cavity flows start to develop. The existing LES code was modified and tested for a three-dimensional lid-driven cavity flow (LDCF) case. POD analysis of unsteady and turbulent LDCF across different Reynolds numbers has been conducted and some preliminary results were obtained. The results are summarized in Appendix. This work can be carried on in future for fully turbulent cases ($Re \geq 10{,}000$) and with a three-dimensional POD analysis. Also, by replacing the lid with an outer flow (as in Figure A.1), possible interaction of the energetic topologies with those in the outer flow can be investigated.

Apart from studying different configurations, another effort that would constitute advancement to this research is to improve the POD algorithm based on its vast capabilities in turbulence research. One

potential which is currently under investigation is to perform a high temporal resolution (and/or spatial resolution) POD by using an incomplete, coarse or “gappy” snapshot set. That would be an extension to the existing method in the context of reconstruction of images, such as human faces, from partial data. The proposed method, i.e. performing spatio-temporal gap filling at the same time, seems to be feasible on paper. However, as mentioned, this is an ongoing work and the outcomes are likely being obtained after the defence of this thesis. Another remarkable capability of POD is to design a surface (or a bluff body) based on the desired outer flow energetic topology. That idea is also under review and will be continued after the graduation.

“The end of a melody is not its goal:

but nonetheless, had the melody not reached its end it would not have reached its goal either. A parable!”

Friedrich Nietzsche

Appendix:

Side Work 1: Analysis of Three-dimensional Lid-driven Cavity Flows using Proper Orthogonal Decomposition

Figure A.1 displays the development of local cavity flows in the spacing between two prismatic obstacles. As mentioned in Chapter 1, preliminary results of POD analysis of unsteady and turbulent LDCF was documented in a draft paper for the 7^{th} *International Symposium on Turbulence, Heat and Mass Transfer*, in Sicily, Italy (September 2012). To verify the validity of the simulation, the case of a steady cavity flow at $Re = 1000$ was first tested. The steady state velocity profiles along the centerlines was measured and verified with the existing literature (Figure A.2).

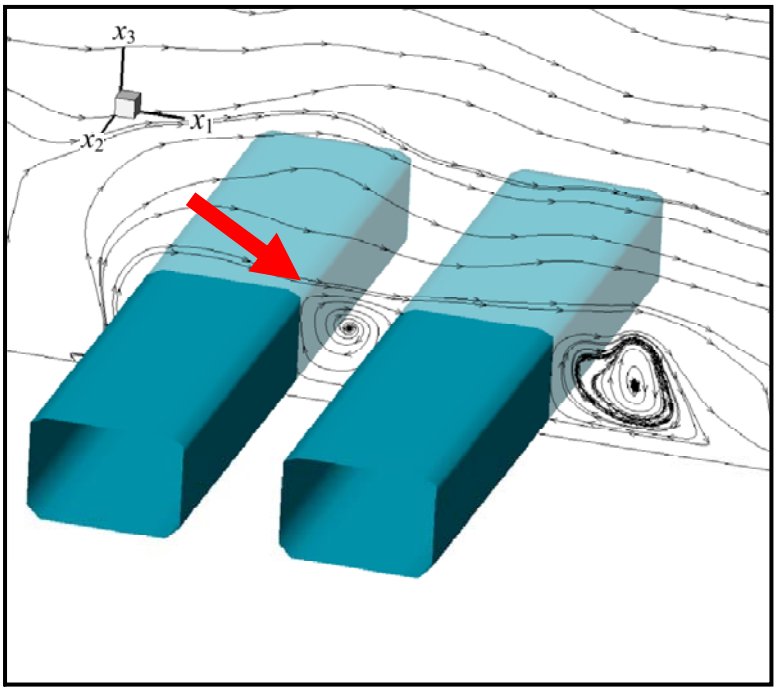

Figure A.1: formation of cavity flow between the elements

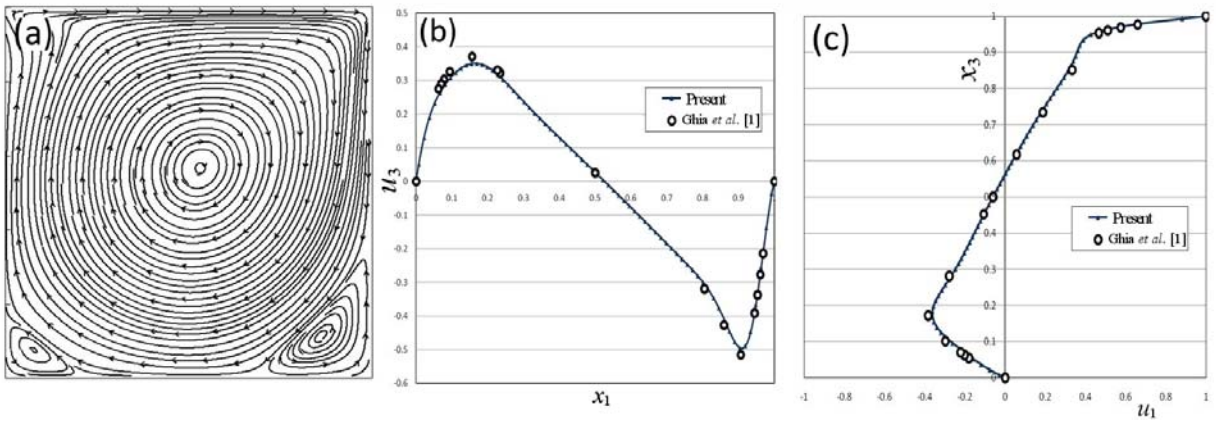

Figure A.2: Steady solution at $Re = 1000$: (a) streamlines, and velocity profiles along (b) horizontal and (c) vertical centerlines

In order to convert the laminar benchmark case to a time-dependent or transient flow field, a time dependent, periodic velocity was imposed on the moving lid. In this case, the POD technique was able to capture more than 99% of the total kinetic energy using only the first four modes. These four modes are displayed in Figure A.3. The first two can be identified as the dominant vortical structures of the flow. The first eigenmode represents the main vortex in the core region. The second mode denotes the change in the shape of the main vorticity due to the periodic motion of the upper wall. Modes 3 and 4 show the formation of the secondary and tertiary vortices.

Following the initial validation of the simulation and the POD algorithm, the simulation of higher *Re* LDCF was performed. The instantaneous streamline patterns in the vertical centre plane of two quasi-turbulent flows at $Re = 3000$ and 8000 is shown in Figure A.4. For both cases the flow is quasi-periodic in time, although instabilities begin to appear in the second flow.

Ultimately POD was performed on the higher *Re* quasi-turbulent flow cases, and energy spectrum was analyzed. It was concluded that the convergence of eigenmodes is significantly slower than the laminar case, but faster than a fully turbulent flow. The velocity vector plot of the first two dominant modes for the $Re = 8000$ case is plotted in Figure A.5. Although, for the POD analysis, the mean flow dynamic was subtracted, some large scale dynamics can still be seen near the core region. That was

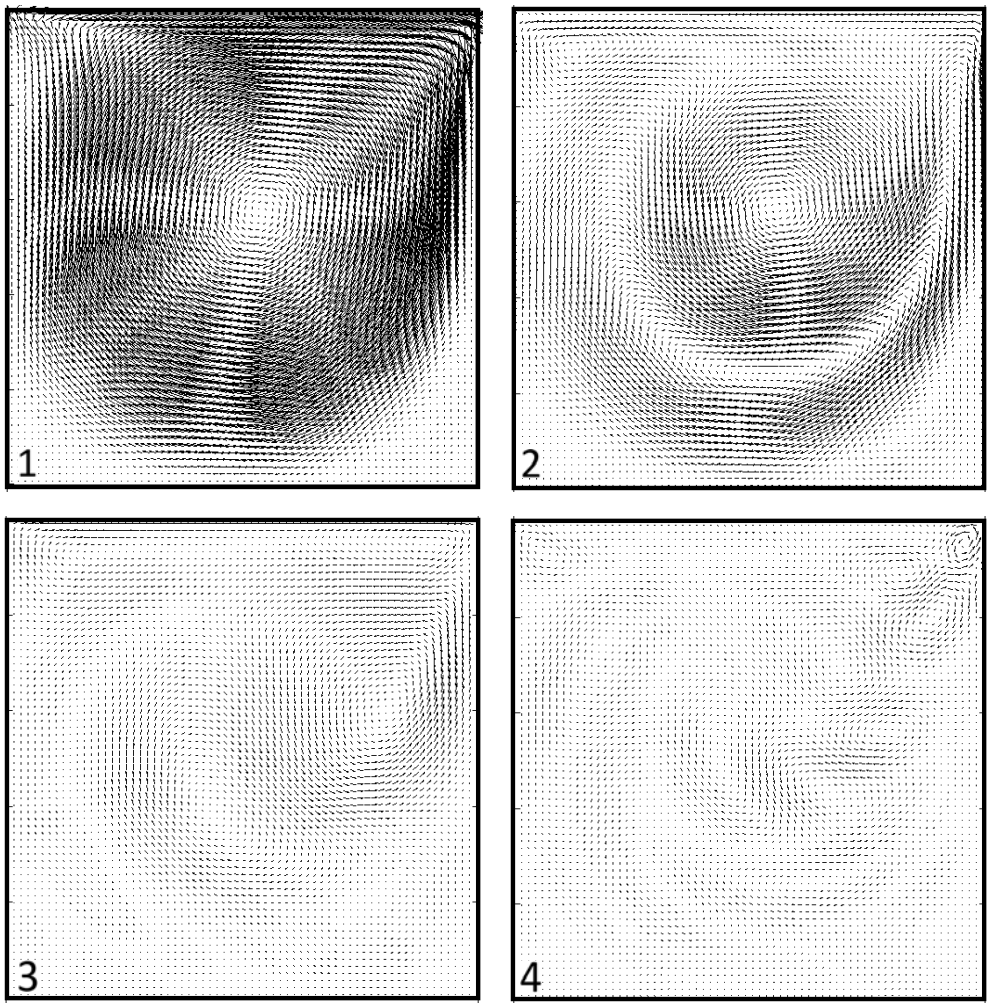

Figure A.3: Velocity vectors for the first 4 eigenmodes

shown to be due to the fact that the flow is not yet fully turbulent. The formation of eddies in the bottom corners of the cavity is displayed in Figure A.5. Since most of the energy is associated with the first eigenmode, which is most active in the lower right hand corner, it can be concluded that the largest velocity fluctuations also occur in this region of the cavity.

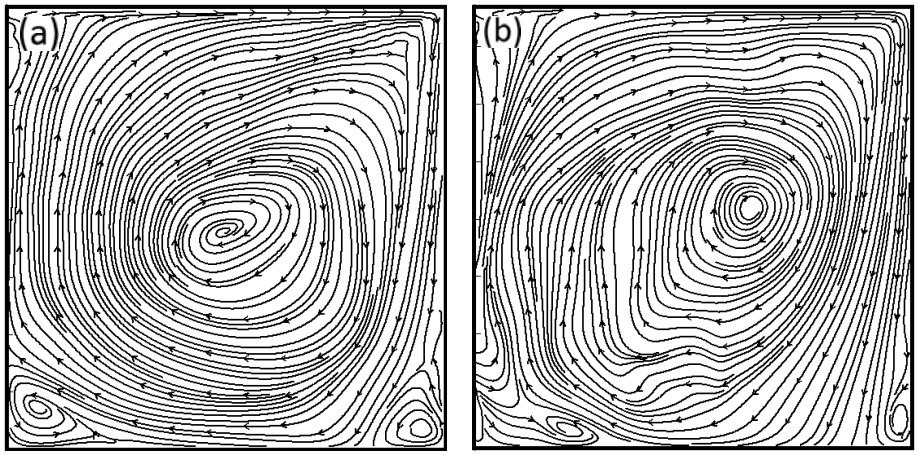

Figure A.4: Streamline patterns of (a) *Re* = 3000 and (b) *Re* = 8000

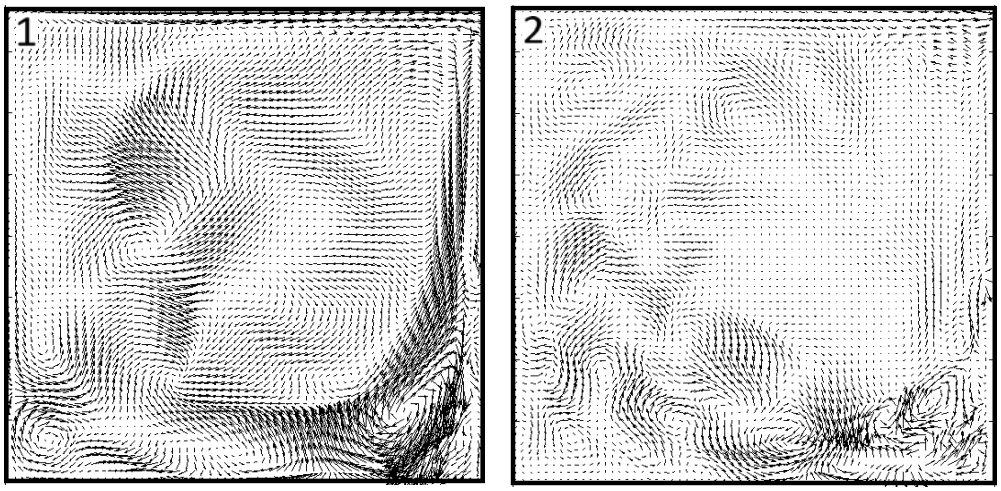

Figure A.5: Velocity vectors for the first 2 eigenmodes ($Re = 8000$)

References:

[1] U. Ghia, K. N. Ghia and C. T. Shin, “High-Re solutions for incompressible flow using the Navier-Stokes equations and a multigrid method”, *Journal of Computational Physics*, 48: 387-411, 1982.